Evaluation of four rugged long-term velocity measurement methods for assessment of hydrokinetic energy production

by

Seongtaek Oh

A Thesis Submitted to the Faculty of Graduate Studies of the University of Manitoba

in Partial Fulfilment of the Requirements of the Degree of

MASTER OF SCIENCE

Department of Mechanical Engineering

The University of Manitoba Winnipeg

Copyright © Seongtaek Oh, 2023. All rights reserved.

Abstract

Four sensors embedded in a tear-shaped buoy are investigated to measure non-instantaneous river velocity to eliminate seasonal elements that can damage velocity instruments when deployed over a long-term period for measurements at energetic sites. Velocity data is required to predict the 95% confidence interval of the power production from hydrokinetic turbines at potential river sites. This novel measurement buoy measures flow velocities inferred from the tilt angle of the buoy using an inertial measurement unit sensor, tension on the wire rope connecting the buoy to the riverbed anchor using a strain gauge sensor, vortex-induced vibration of the mooring line also using an inertial measurement unit sensor, and sound of the water flowing around the buoy using a microphone sensor. The four sensors are embedded in a prototype buoy and tested in a laboratory water tunnel at flow velocities from 0.1 to 1 m/s. The laboratory measurement data is analyzed to find the relationship of each sensor to water velocity based on a phenomenon-based approach. The data from the sensors displayed a nonlinear relationship with flow velocity. Calibration curves were developed for each sensor to measure the flow velocity. The most accurate measurement method is tilt angle method. The average percent error in accuracy for estimation of flow velocities from 0.5 to 1 m/s from tilt angle data is 0.5 %. Each of the sensors embedded in the buoy is critically assessed for its validity to estimate the long-term river velocity at energetic river sites to determine the power production from potential hydrokinetic turbine sites.

Acknowledgements

I first want to thank Dr. Eric Bibeau for providing me the opportunity to research for improving hydrokinetic resource assessment. With his advisory help, I was able to obtain unique experience to investigate on measurement methods. I also want to thank the technologist, Mr. Zeev Kapitanker who assisted me a lot to search for parts and materials necessary for the research and instructed me how to handle them. Mr. Erwin Sy, my colleague, helped and encouraged me to complete measurements. Another coordinator, Mr. Kirk Mason, helped me to go at the middle of different rivers for me to deploy a measurement device. Mr. Nik Reimer finished preparing for the device to be ready to be floatable on water. Finally, Mr. Nick Jackimec designed the prototype used for this research. I also want to appreciate Dynamic Systems Analysis Ltd. For providing me thorough support for ProteusDS simulations.

Contents

1. Introduction 1

1.1. Hydropower and hydrokinetic power 2

1.2. Hydrokinetic energy resource assessment for determining hydrokinetic turbine sites 5

1.3. Challenges on measurement of higher flow velocity for a long term 7

1.4. Four variables related to flow velocity 8

1.4.1. Tilt angle of tear-shape buoy and tension force of mooring rope 9

1.4.2. Vibration acting on mooring line of tear-shape buoy 12

1.4.3. Sound of water flowing over tear-shape buoy 13

1.5. Objectives 14

1.6. Methodology 14

1.7. Research contributions 15

1.8. Outline 16

2. Literature review 17

2.1. Velocity measurement techniques for open channel flow 17

2.1.1. Acoustic instruments 17

2.1.2. Measurement methods with water contact 19

2.1.3. Measurement methods without water contact 22

2.2. Vortex-induced vibration 24

2.3. Sound level 30

2.4. Instrumentation 31

2.4.1. Tilt measurement using accelerometer 31

2.4.2. Force measurement using strain gauge 34

2.4.3. Vibration measurement using piezoelectric sensor 35

3. Measurement data collection in water tunnel 38

3.1. Prototype buoy of rugged long-term velocity meter 38

3.2. Instrumentation 40

3.2.1. Accelerometer 41

3.2.2. Customized load cell 42

3.2.3. Piezo-film sensor 42

3.2.4. Electret condenser microphone 45

3.2.5. Arduino code 46

3.3. Data collection in water tunnel 47

3.3.1. Variable conditions in data collection 49

3.3.2. Data collection procedures in water tunnel 50

3.4. Simulation to find relationship between mooring line tension and flow velocity 51

3.5. Test matrix 54

4. Laboratory measurement results and discussions 57

4.1. Measurement data of four variables for identifying relationship with flow velocity 57

4.1.1. Tilt angle 62

4.1.2. Mooring line tension 64

4.1.3. Vibration amplitude 65

4.1.4. Sound 66

4.1.5. Other possible sources of error 67

4.1.6. Noise of variable frequency drive (VFD) of water tunnel 68
4.2. Calibration curves by curve-fitting 71
4.2.1. Residual plots to assess trendlines 73
4.2.2. Elimination of effects originated from other variables related to flow velocity 76
4.3. Estimation of flow velocity using trendline function from each variable 78
4.3.1. Tilt angle of the prototype buoy 78
4.3.2. Mooring tension on the prototype buoy 79
4.3.3. Vibration amplitude of the prototype buoy 81
4.3.4. Sound level around the prototype buoy 82
4.4. Different characteristics between water tunnel and river 84
4.4.1. Flow condition 84
4.4.2. Underwater portion of prototype buoy 85
4.4.3. ProteusDS simulations to find different characteristics between water tunnel and river 85
4.5. Evaluation of the four measurement methods 88
5. Conclusion and recommendations 91
5.1. Conclusion 91
5.2. Recommendations 93
6. Bibliography 95

List of Figures

Figure 1.1: Global monthly mean CO_2 since 1980 [1] 1

Figure 1.2: Global surface temperature deviation when the average temperature of 1951-1980 is the reference point [4] 2

Figure 1.3: Satellite data of global sea level change since 1993 [2] 2

Figure 1.4: Estimated share of renewable energy in global electricity generation in 2019 [3] 3

Figure 1.5: Simplified free body diagram of mooring buoy 10

Figure 1.6: Flow chart of the methodology for testing in the water tunnel 15

Figure 2.1 Propellor meter [24] 20

Figure 2.2 Hot-wire anemometer [25] 20

Figure 2.3: Tilt current meter [27] 21

Figure 2.4: Overall behavior of vortex-induced synchronization including both in-line and transverse oscillations [38] where the legend is "- -": in-line oscillation; "—": transverse oscillation 26

Figure 2.5: Vortex-induced in-line oscillations of a flexible cantilevered circular cylinder in water when U*< 4 [40]. ∘, Re=6×105; ×, Re=6×104 26

Figure 2.6: Oscillation characteristics for a freely vibrating circular cylinder in air, where the legend is ◯: vortex shedding frequency; +: cylinder frequency; □: phase angle; ×: oscillation amplitude; ϕ°: phase angle between fluid force and cylinder's displacement; f_w: vortex shedding frequency; f_c: oscillating frequency of cylinder; A*: amplitude ratio (A*=A/D) [43]. 28

Figure 2.7: Comparison of transverse vibration amplitude between Khalak's study and Feng's [44] where the legend is ●: Khalak's study; ◇: Feng's study. 29

Figure 2.8: Frequency response f* for m*=2.4 [46] 30

Figure 2.9: Frequency response f* for m*=10.3 and m*=20.6 [46]. 30

Figure 2.10: Pitch and roll angle of object [49] 32
Figure 2.11: Basic structure of an accelerometer [50] 33
Figure 2.12: Block diagram of three-axis accelerometer including built-in A/D converter [51] 33
Figure 2.13: Measurement system for strains with a strain gauge [52] 35
Figure 2.14: Charge amplifier for piezoelectric sensor [53] 37
Figure 3.1: Prototype buoy of rugged long-term velocity meter before and after including load cell 39
Figure 3.2: Arduino board including a prototyping shield, a strain gauge ampifier and a charge amplifier circuit board 40
Figure 3.3: Inside of cylinder canister viewed from top of the prototype buoy 40
Figure 3.4: 10-degree of freedom IMU breakout assembled on a prototyping shield 41
Figure 3.5: Customized load button load cell 42
Figure 3.6: General-purpose piezo-film 43
Figure 3.7: Sensitivity of piezo-film sensor in different rotation (orientation) angles [58] 43
Figure 3.8: Indication of the reference angle, 0°, on buoy axial pipe and canister 44
Figure 3.9: Three piezo-film sensors installed on inner wall of buoy axial pipe: one piezo-film with flat washers attached both sides and aligned with the indicated reference angle is used. 44
Figure 3.10: Charge amplifier for two piezo-film sensors 44
Figure 3.11: Electret condenser microphone MAX4466 [59] 45
Figure 3.12: Top view of old cylinder canister lid 46
Figure 3.13: Bottom view of old cylinder canister lid 46
Figure 3.14: Top view of new cylinder canister lid 46
Figure 3.15: Bottom view of new cylinder canister lid 46

Figure 3.16: Water tunnel in the Renewable Energy Lab 48
Figure 3.17: Remote control of water tunnel 48
Figure 3.18: Calibration plot to obtain flow velocity from pump frequency 48
Figure 3.19: Side view of the prototype buoy anchored with steel bars in water tunnel before load cell assembled 51
Figure 3.20: Side view of the prototype buoy in water tunnel after load cell assembled 51
Figure 3.21: Top side view of the prototype buoy 51
Figure 3.22: Prototype buoy simulation in water tunnel setting in ProteusDS 52
Figure 3.23: ProteusDS simulation of the velocity meter in river 52
Figure 4.1: Forty-eight trials of tilt angle measurements vs. flow velocity before load cell is installed 59
Figure 4.2: Selected trials of tilt angle measurements vs. flow velocity after load cell is installed 59
Figure 4.3: Fifty-three trials of mooring line tension measurements vs. flow velocity after load cell is installed 60
Figure 4.4: Forty-eight trials of piezo-film voltage measurements vs. flow velocity before load cell is installed 60
Figure 4.5: Selected trials of piezo-film voltage measurements vs. flow velocity after load cell is installed 61
Figure 4.6: Forty-eight trials of microphone voltage measurements vs. flow velocity before load cell is installed 61
Figure 4.7: Selected trials of microphone voltage measurements vs. flow velocity after load cell is installed 62
Figure 4.8: Flow velocity at 0 m/s when initial tilt angle is 60° 64
Figure 4.9: Flow velocity at 1 m/s when initial tilt angle is 60° 64

Figure 4.10: Flow velocity at 0 m/s when load cell is assembled....65
Figure 4.11: Flow velocity at 1 m/s when load cell is assembled....65
Figure 4.12: Ten trials of sound measurements to compare between dry tarp and wet tarp condition....67
Figure 4.13: Average of two trials of VFD sound voltage vs. flow velocity....69
Figure 4.14: Eight sound measurements with and without VFD noise in dry tarp condition....70
Figure 4.15: Average % ratio of VFD voltage to microphone voltage from eight sound measurements....70
Figure 4.16: Trendline function of 43 tilt angle measurement data vs. flow velocity .71
Figure 4.17: Trendline function of 50 tension measurement data vs. flow velocity....71
Figure 4.18: Trendline function of 43 vibration amplitude measurement data vs. flow velocity....72
Figure 4.19: Trendline function of 43 sound measurement data vs. flow velocity....72
Figure 4.20: Trendline function of 50 mooring line tension measurement data vs. flow velocity excluding low flow velocities from 0 to 0.2 m/s....72
Figure 4.21: Residual plot of trendline of tilt angle of the prototype buoy against flow velocity....74
Figure 4.22: Residual plot of trendline of tension of the prototype buoy against flow velocity....74
Figure 4.23: Residual plot of trendline of vibration amplitude of the prototype buoy against flow velocity....74
Figure 4.24: Residual plot of trendline of sound about the prototype buoy against flow velocity....74
Figure 4.25: Residual plot of trendline of mooring line tension of the prototype buoy against flow velocity excluding 0 to 0.2 m/s....75

Figure 4.26: lnVpiezo vs. flow velocity with trendline 76
Figure 4.27: Residual plot of Figure 4.26 76
Figure 4.28: lnVmic vs. flow velocity with trendline 76
Figure 4.29: Residual plot of Figure 4.28 76
Figure 4.30: lnVmic vs. flow velocity with trendline in dry tarp condition of 19 measurements 77
Figure 4.31: Residual plot of Figure 4.30 77
Figure 4.32: lnVmic vs. flow velocity with trendline in wet tarp condition of 20 measurements 77
Figure 4.33: Residual plot of Figure 4.32 77
Figure 4.34: Plot of estimated flow velocity using tilt angle measurements 79
Figure 4.35: Plot of estimated flow velocity using mooring line tension measurements 80
Figure 4.36: Plot of estimated flow velocity using vibration measurements 82
Figure 4.37: Plot of estimated flow velocity using sound measurements 83
Figure 4.38: ProteusDS result of mooring tension force of wire rope vs. flow velocity from 0.1 to 1 m/s in water tunnel setting 87
Figure 4.39: ProteusDS result of mooring tension force of wire rope vs. flow velocity from 0.5 to 4 m/s in river setting 87
Figure 4.40: Combined plot of Figure 4.38 and Figure 4.39 87
Figure 4.41: ProteusDS result of tilt angle of prototype buoy vs. flow velocity from 0.1 to 1 m/s in water tunnel setting 88
Figure 4.42: ProteusDS result of tilt angle of prototype buoy vs. flow velocity from 1 to 2.5 m/s in river setting 88

List of Tables

Table 1: List of flow features at hydrokinetic turbine location [11] 6

Table 2: Differences between water tunnel and river in ProteusDS 53

Table 3: Test matrix. **A**: Measurement before load cell is installed; **B**: Measurement after load cell is installed; W: wet tarp; O: data collected. 55

Table 4: Tilt angle measurements from 0.5 to 1 m/s flow velocity with corrected values 79

Table 5: Mooring line tension measurements and estimated velocity from 0.5 to 1 m/s 80

Table 6: Vibration measurements and estimated velocity from 0.5 to 1 m/s 81

Table 7: Sound level measurements and estimated velocity from 0.5 to 1 m/s 83

Table 8 Evaluation of the four rugged long-term velocity meter methods. (ln): taking natural logarithm on voltage signals 90

Nomenclature

Latin letters

A	Vortex induced vibration amplitude
A^*	Amplitude ratio
A_t	Rotor area of hydrokinetic turbine
A_x	Acceleration of object in x-component
A_y	Acceleration of object in y-component
A_z	Acceleration of object in z-component
C_D	Drag coefficient of frontal shape of object against flow
C_f	Feedback capacitance in charge amplifier
C_L	Lift coefficient of frontal shape of object against flow
Cp	Power coefficient of hydrokinetic turbine
c	Speed of sound
D	Characteristic diameter
D_c	Diameter of oscillating cylinder
d_{3n}	Piezoelectric coefficient for the mechanical axis, n
E	Elastic modulus of material
F_B	Buoyant force
F_D	Drag force of flowing water to object
F_G	Gravitational force; weight
F_L	Lift force
F_T	Tension force
f^*	Frequency ratio
f_c	Oscillating frequency of cylinder
f_N	Natural frequency

f_w	Vortex shedding frequency
g	Gravitational acceleration
k	Spring constant
L_c	Length of oscillating cylinder
l_0	Initial length of material
m^*	Dimensionless mass
m_A	Added mass
n	Mechanical axis of applied stress or strain
Q	Electric charge
Q_R	Resistivity
Q_{R_0}	Initial resistivity
R	Electrical resistance
R_0	Initial electrical resistance
Re	Reynolds number
r	Turbine rotor radius
St	Strouhal number
U	Mean velocity of flowing water
U^*	Dimensionless velocity of flowing water

Greek letters

Δl	Change in length of material
δ	Logarithm microphone decrement
ϵ	Strain of material
ζ	Damping ratio
λ	Tip speed ratio

ν	Poisson's ratio
ρ_f	Density of fluid
ρ_w	Density of water
σ	Stress of material
σ_n	Applied stress in the mechanical axis, n
ϕ	Roll of object
ω	Angular velocity of turbine rotor

Word subscripts

A_{piezo}	Conductive electrode area of piezoelectric sensor
$A_{wetted_{buoy}}$	Wetted area of buoy
C_{piezo}	Capacitance of piezoelectric sensor
f_{cutoff}	Cut-off frequency
$f_{doppler}$	Frequency of wave after doppler effect is applied
f_{source}	Frequency of source wave frequency emitted from ADV
$P_{technical}$	Technically available hydrokinetic power
V_{mic}	Output voltage of microphone
$V_{mic(d)}$	Output voltage of microphone with dry tarp condition
$V_{mic(d+w)}$	Output voltage of microphone with dry and wet tarp condition
V_{out}	Output voltage of sensor after amplification
V_{piezo}	Output voltage of piezoelectric sensor
V_{supply}	Supply voltage for each sensor
$V_{wetted_{buoy}}$	The wetted volume of buoy
v_{actual}	Actual flow velocity

$v_{estimated}$	Estimated flow velocity = v_{flow}
$V_{mic(d)}$	Output voltage of microphone with dry tarp condition
$V_{mic(d+w)}$	Output voltage of microphone with dry and wet tarp condition
θ_{tilt}	Tilt angle of object
$\theta_{tilt\_corrected}$	Corrected tilt angle
$\theta_{tilt\_estimated_0}$	Estimated tilt angle when estimated flow velocity is zero
θ_{tilt_raw}	Raw data of tilt angle
$\theta_{tilt\_raw_0}$	Raw data of tilt angle at zero flow velocity

Acronyms

ADCP	Acoustic doppler current profiler
ADV	Acoustic doppler velocimeter
CHTTC	Canadian Hydrokinetic Turbine Testing Centre
GPS	Global Positioning System
IMU	Inertial Measurement Unit
IP	Ingress Protection rating
LDV	Laser Doppler Velocimetry
LSPIV	Large Scale Particle Image Velocimetry
MEMS	Micro-Electromechanical Systems
PIV	Particle Image Velocimetry
PTV	Particle Tracking Velocimetry
STIV	Space Time Image Velocimetry
VFD	Variable Frequency Drive

1. Introduction

The global average concentration of atmospheric carbon dioxide, CO_2, increases every year from excessive fossil fuel consumption worldwide—a train that goes around the earth 84 times is required to carry all the coal, liquefied natural gas and oil consumed in 2022. According to National Oceanic and Atmospheric Administration Earth System Research Laboratory, Figure 1.1 shows that the global annual mean CO_2 concentration surpassed 400 ppm in 2016 [1] and is now 420 ppm. Increase in CO_2 concentration causes increase in the global average temperature, as shown in Figure 1.2, because of the greenhouse gas effect. Because of the increase in the global temperature, Figure 1.3 shows that sea levels have been slowly increasing because of melting glaciers of both subarctic and arctic regions and water expansion [2].

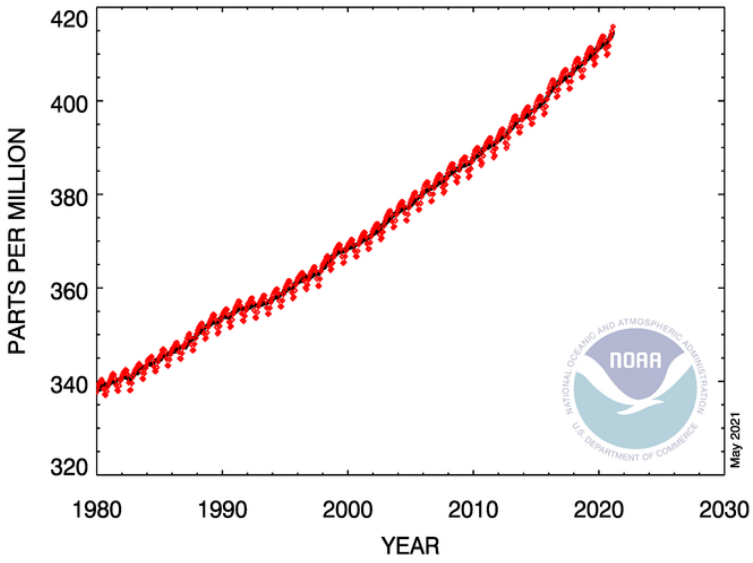

Figure 1.1: Global monthly mean CO_2 since 1980 [1]

Renewable energy is required to reduce usage of fossil fuels that emit CO_2 and other greenhouse gases such as methane. In 2019, 27.3% of global electricity was produced

by renewable energy resources [3], as shown in Figure 1.4. Among the renewable energy resources, hydropower contributed the most with 15.9% of global electricity generation.

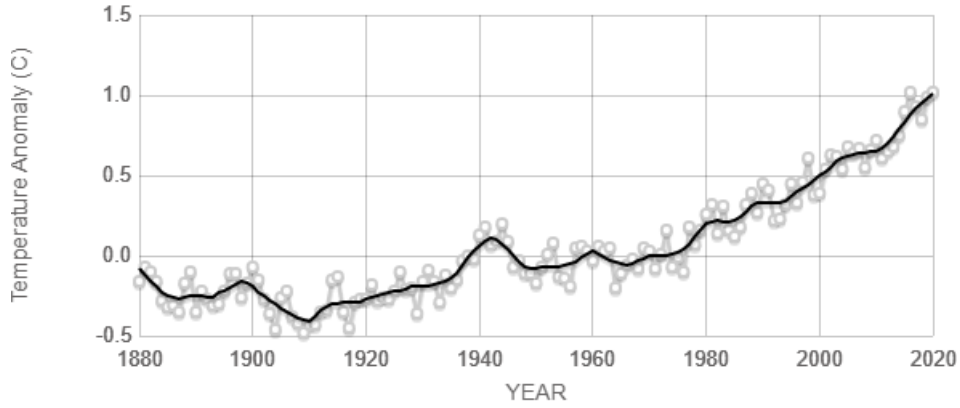

Figure 1.2: Global surface temperature deviation when the average temperature of 1951-1980 is the reference point [4]

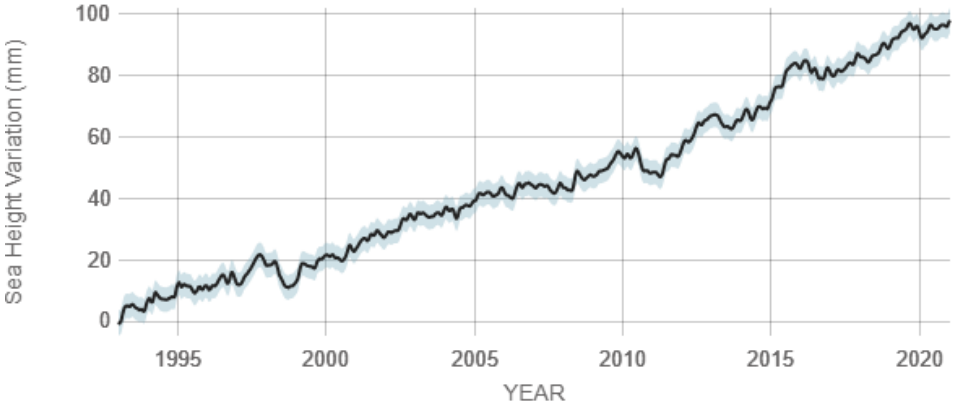

Figure 1.3: Satellite data of global sea level change since 1993 [2]

1.1. Hydropower and hydrokinetic power

Hydropower produces utility scale electricity from the energy that water contains. Conventional hydropower refers to the extracted power from the potential energy of

water. Hydrokinetic power uses the kinetic energy of currents and can be utilized to microgrids.

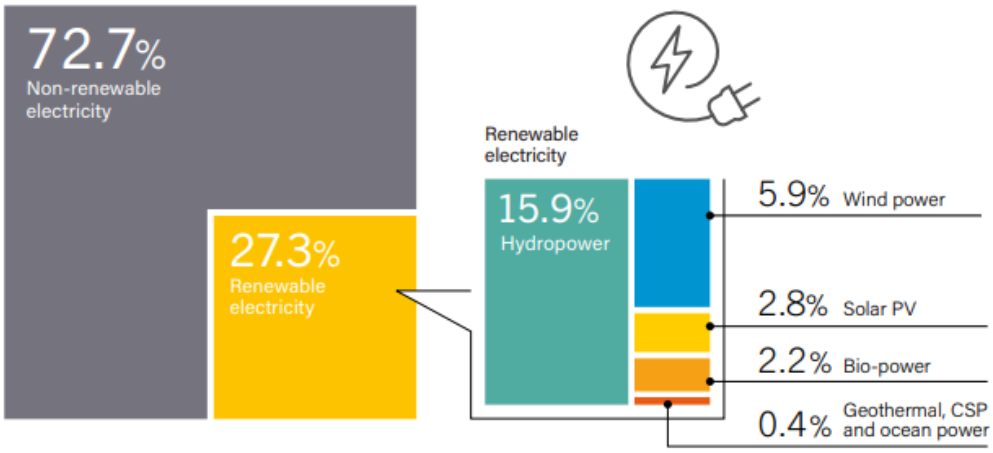

Figure 1.4: Estimated share of renewable energy in global electricity generation in 2019 [3]

Hydrokinetic turbines extract energy from flowing water to generate electric power, $P_{technical}$, using:

$$P_{technical} = \frac{1}{2} C_P \rho_w A_t U^3 \qquad \text{Equation 1.1}$$

where ρ_w is the density of water at the site, A_t is the rotor area of the turbine, U is the mean velocity of water at the site, and C_P is the power coefficient of the turbine. $P_{technical}$ is technically available hydrokinetic power that depends on the power coefficient because the power coefficient has a theoretical limit called Betz limit with a value of 0.59 [5]. The coefficient is affected by the tip speed of the turbine rotor blades. When the tip speed of the rotor blades is low and the water flows fast, most of the water passes through the gap among the blades without energy conversion. Conversely, if the tip speed of the blades is fast while the water flows slow, water flows backward relatively which means energy is lost. Thus, when the ratio, λ,

between the rotor tip and water flow velocity, is the optimum, the power coefficient is also the maximum:

$$\lambda = \frac{r\omega}{U} \qquad \text{Equation 1.2}$$

where r is the radius of rotor, and ω is the angular velocity of rotor.

Hydrokinetic energy has benefits over other renewable energy resources. First, the energy density per unit area is higher than wind turbines [6]. Therefore, smaller location area is needed for the same electricity supply. Second, hydrokinetic energy can address consistent baseload and thus contribute to microgrids.

Despite the benefits of hydrokinetic power, estimation techniques of power at energetic rivers sites is not well developed. Estimation of power potential, including seasonal variations in flow velocities, remains difficult to obtain. Communities do consider utilizing hydrokinetic turbines but can hesitate because they have difficulties with obtaining financing which requires power estimates based on long term velocity measurements. As hydrokinetic turbines are being commercialized, financial institutions will require long-term flow velocity measurement data over at least a year to predict the power produced at a 95% confidence interval.

In contrast, wind measurement data is first collected across Canada using meteorological towers by Environment Canada [7]. For proposed wind turbine farms, guy wire towers equipment with multiple turbine velocity meters are installed for a year at potential wind farm sites to obtain 95% confidence of the power produced and secure bank financing. Once wind data is obtained, a Weibull probability density function can be determined. However, for hydrokinetic turbines, such data is difficult to obtain using conventional instruments in energetic river sites due to harsh elements.

1.2. Hydrokinetic energy resource assessment for determining hydrokinetic turbine sites

Determining the power production of hydrokinetic turbines from a proposed site is an essential process before turbines are installed—the power produced, like wind turbines, depends on the velocity cubed. Hydrokinetic turbines will extract the maximum electric power possible when maximum power point tracking is enabled, delivering renewable electricity to address community baseloads. Therefore, resource assessment to estimate the available hydrokinetic energy at a site of interest is necessary before installation of hydrokinetic turbines.

The potential hydrokinetic energy available from rivers in Canada is 300 to 700 GW [8]. However, the actual technical estimation of hydrokinetic energy needs to consider parameters in Equation 1.1 for hydrokinetic turbines, leading to a much lower value. Furthermore, additional features need to be considered to estimate the available hydrokinetic energy. Table 1 summarizes the features that characterize the flow at energetic river locations. To these features, we also need to include turbulence measurements which is a factor in selecting a suitable hydrokinetic turbine site. Moreover, hydrokinetic turbines need to withstand turbulent fluctuations and consider the effect of vibration and cyclic loading caused by the turbulent flow.

River velocity profiles in the vertical direction from the free surface to the riverbed is another key flow feature in resource assessment. Since the river velocity is higher near the free surface than at the bottom [9], hydrokinetic turbines are more effectively located near the free surface. In terms of installation cost, near-surface turbines are also more cost-effective [10].

Table 1: List of flow features at hydrokinetic turbine location [11]

Feature	Contribution
Mean velocity	▪ Power ▪ Mooring
Temporal flow variation	▪ Yearly power prediction
Turbulence intensity	▪ Wear ▪ Vibration ▪ Mooring ▪ Safety
Time scale	▪ Wear ▪ Cyclic loading ▪ Vibration ▪ Turbine design
Length scale	▪ Wear ▪ Cyclic loading ▪ Vibration ▪ Turbine design
Dissipation rate	▪ Wear ▪ Cyclic loading ▪ Vibration ▪ Turbine design
Velocity profile	▪ Turbine position ▪ Turbine design ▪ Max power
Boundary layer	▪ Turbine design ▪ Max power
Water depth	▪ Turbine design ▪ Safety ▪ Mooring
Bathymetry	▪ Turbine design ▪ Safety
Sediment	▪ Wear ▪ Instrument use
Wildlife	▪ Safety ▪ Environment
Ice cover	▪ Safety ▪ Placement ▪ Year-round use

The profile of the riverbed impacts the velocity resources. Hydrodynamic microphone features and velocity profiles are impacted by the bathymetry of the riverbed. Moreover, flow mixing of riverbed sediments can impact turbine operations and wear. Therefore, sedimentation can also be a factor in the resource assessment.

Among the features that determine hydrokinetic turbine sites, the mean flow velocity is the key factor because the estimated potential electric power based on the flow velocity data helps find the most beneficial location. The mean flow velocity can be measured directly by a portable velocity meter. However, to know the temporal variation of the flow to predict the yearly power generation, the velocity meter must be able to measure at the same point for at least a year to characterize the flow velocity. Because water depth and discharge from the source can vary due to precipitation throughout year, the flow velocity changes seasonally year-round.

1.3. Challenges on measurement of higher flow velocity for a long term

Instruments for flow velocity measurement are developed and available in the market. Acoustic doppler velocimeter (ADV) and acoustic doppler current profiler (ADCP) are commonly used instruments to measure velocity of river and ocean tide flow. Even though these are useful, applying these instruments for a long-term measurement for hydrokinetic energy resource assessment is challenging because the instruments need to withstand the elements, like the drag force, F_D, of the flowing water:

$$F_D = \frac{1}{2} C_D \rho_w A U^2, \qquad \text{Equation 1.3}$$

where C_D is the drag coefficient determined by the shape of the object to the flow, and A is the frontal area of the object to the flow. According to the equation, as the flow velocity doubles, the drag force increases by a factor of four. Because the water

velocity increases if there are heavy rains or snow, a secure mooring for the velocity measuring device is essential to withstand against the energetic flow over a full year. The instruments for flow velocity measurements are often damaged at energetic sites and need to be powered. Even the mooring design itself required for velocity measurements is challenging. Any heavy and rigid objects flowing along the river can also damage the instruments especially when flood occurs. Different methods of flow velocity measurement are reviewed in Chapter 2.

1.4. Four variables related to flow velocity

The Canadian Hydrokinetic Turbine Testing Center (CHTTC) located on the Winnipeg River tests hydroelectric turbines to advance the technology readiness level of new turbine designs. The CHTTC has tried to measure flow velocities over year long campaigns but have found this to be too difficult using commercial instruments. Instruments fail and are often lost to the elements. However, during testing, CHTTC researchers have developed the ability to infer the flow velocity from peal-shaped buoys using four methods—tilt, tension, vibration, and sound—and three senses—eyesight, hearing, and touching senses. The four methods to infer flow velocity used by CHTTC researchers could eliminate the need to expose sensors to the elements and enable to estimate the power within a 95% confidence interval over at least 1 year at a proposed energetic site. Therefore, these four methods could be of interest commercially to measure flow velocity for year-long resource assessments and are presented below. As for the shape of buoy, only tear-shaped type buoys are used as they survive winter as ice will not stick to these buoys, with some of these surviving more than 15 years.

1.4.1. Tilt angle of tear-shape buoy and tension force of mooring rope

Mooring buoys are fixed at the riverbed and are often used in the marine industry. When the flow velocity increases, hydrodynamic drag and lift force acting on the buoy and the mooring line also increase. Because of the tension, the buoy gets pulled downwards, which causes the buoyant force to increase as more water must be displaced. In this situation, the tilt angle of the buoy and tension on the mooring line are increased. Theoretically, the relationship of tilt angle of the buoy and tension in the mooring line can be analyzed by the force balance shown in Figure 1.5, where l is vertical length from the free surface to point anchor A; θ_{tilt} is the tilt angle of the buoy; F_T is the wire rope tension; F_B is the buoyant force; F_L is the lift force and F_g is the weight. Assumptions to simplify the shape of mooring buoy and flow condition for the force balance are:

- Two-dimensional analysis is considered.
- Rotational motion of the buoy is assumed to be negligible.
- Relative motion between the buoy and the cable is negligible.
- The wire rope is one rigid body element having uniform cross-sectional area.
- Centre of mass, G, is located at the half-way point of the wire rope. Buoyant, drag, and gravitational force of the wire rope is acted at the centre of mass.
- The buoyant force of the wire rope is negligible.
- The buoy is a sphere.
- Steady flow condition is considered.

Using the free body diagram and the assumptions, the relationship of tilt angle and tension with flow velocity can be derived as follows:

$$\overset{+}{\rightarrow} \Sigma F_x = F_{D,buoy} + F_{D,wire\ rope} - A_x = 0 \qquad \text{Equation 1.4}$$

$$\uparrow^{+} \Sigma F_z = F_{B,buoy} + F_{L,buoy} + F_{L,wire\ rope} - F_{G,buoy} - F_{G,wire\ rope} - A_z = 0 \qquad \text{Equation 1.5}$$

$$ccw^{+}\Sigma M_A = +F_{L,buoy} \sin\theta_{tilt} * d_{AB} + F_{B,buoy} \sin\theta_{tilt} * d_{AB} - F_{D,buoy} \cos\theta_{tilt} * d_{AB} - F_{G,buoy} \sin\theta_{tilt} * d_{AB} - F_{D,wire\ rope} \cos\theta_{tilt} * \frac{l}{2} + F_{L,wire\ rope} \sin\theta_{tilt} * \frac{l}{2} - F_{G,wire\ rope} \sin\theta_{tilt} * \frac{l}{2} = 0 \qquad \text{Equation 1.6}$$

$$\Sigma F_{A,x} = F_T \sin\theta_{tilt} - A_x = 0 => A_x = F_T \sin\theta_{tilt} \qquad \text{Equation 1.7}$$

$$\Sigma F_{A,z} = F_T \cos\theta_{tilt} - A_z = 0 => A_z = F_T \cos\theta_{tilt} \qquad \text{Equation 1.8}$$

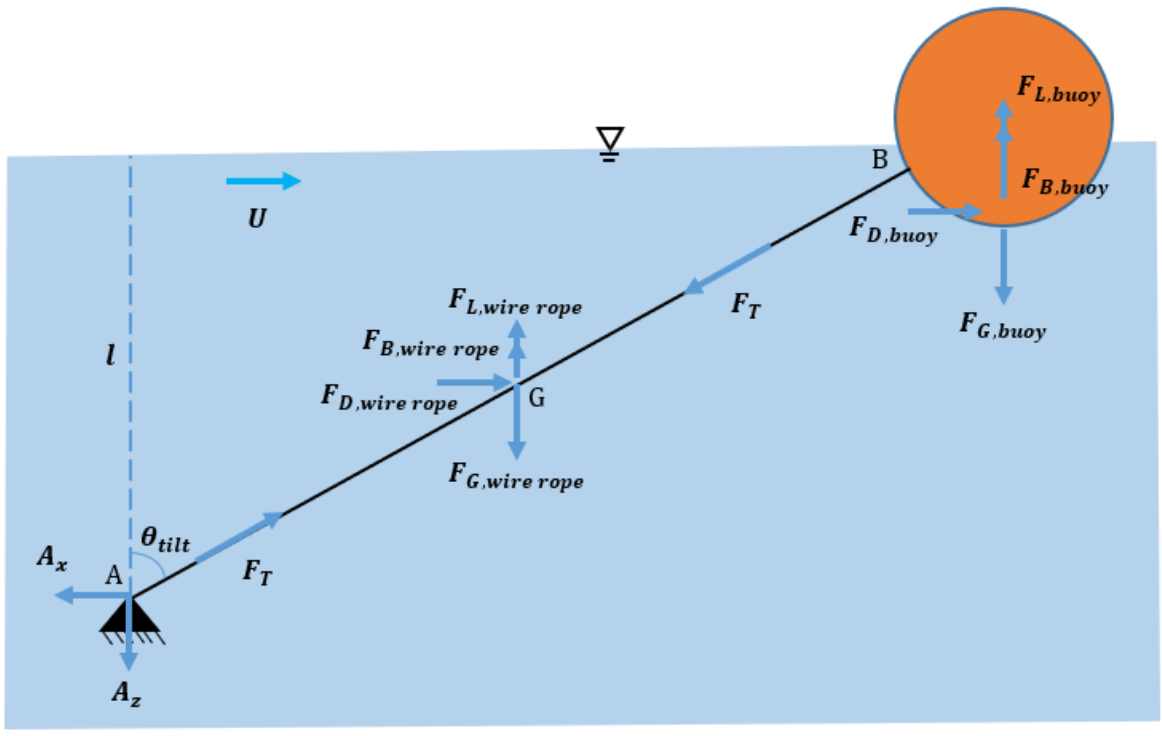

Figure 1.5: Simplified free body diagram of mooring buoy

By substituting Equation 1.7 into Equation 1.4, and Equation 1.8 into Equation 1.5,

$$=> \Sigma F_x = F_{D,buoy} + F_{D,wire\ rope} - F_T \sin\theta_{tilt} = 0 \quad \text{Equation 1.9}$$

$$=> \Sigma F_z = F_{B,buoy} + F_{L,buoy} + F_{L,wire\ rope} - F_{G,buoy} - F_{G,wire\ rope} - F_T \cos\theta_{tilt} = 0 \quad \text{Equation 1.10}$$

By rearranging Equation 1.9 for tension force, F_T,

$$F_T = \frac{F_{D,buoy} + F_{D,wire\ rope}}{\sin\theta_{tilt}}$$

$$= \frac{\frac{1}{2} C_{D,buoy} \rho_w A_{wetted_{buoy}} U^2 + \frac{1}{2} C_{D,wire\ rope} \rho_w A_{wire\ rope} U^2}{\sin\theta_{tilt}} \quad \text{Equation 1.11}$$

$$= \frac{\rho_w (C_{D,buoy} A_{wetted_{buoy}} + C_{D,wire\ rope} A_{wire\ rope}) U^2}{2 \sin\theta_{tilt}}$$

$$U = \sqrt{\frac{2 * \sin\theta_{tilt}}{\rho_w [(C_D A)_{wetted_{buoy}} + (C_D A)_{wire\ rope}]}} * F_T \quad \text{Equation 1.12}$$

shows that when the flow velocity doubles, the tension of wire rope increases four times if the other variables' change with respect to flow velocity is negligible. By rearranging Equation 1.10 for tension force, F_T,

$$F_T = \frac{(F_{B,buoy} + F_{L,buoy} + F_{L,wire\ rope}) - (F_{G,buoy} + F_{G,wire\ rope})}{\cos\theta_{tilt}} \quad \text{Equation 1.13}$$

Combining and Equation 1.13,

$$\tan\theta_{tilt} = \frac{F_{D,buoy} + F_{D,wire\ rope}}{(F_{B,buoy} + F_{L,buoy} + F_{L,wire\ rope}) - (F_{G,buoy} + F_{G,wire\ rope})} \quad \text{Equation 1.14}$$

$$= \frac{C_{D,buoy} \rho_w A_{wetted_{buoy}} U^2 + C_{D,wire\ rope} \rho_w A_{wire\ rope} U^2}{2g \times \left(\rho_w V_{wetted_{buoy}} - m_{buoy} - m_{wire\ rope}\right) + \rho_w \left(C_{L,buoy} A_{wetted_{buoy}} + C_{D,wire\ rope} A_{wire\ rope}\right) U^2}$$

$$\theta_{tilt} = \tan^{-1}\left[\frac{\left(C_{D,buoy} \rho_w A_{wetted_{buoy}} + C_{D,wire\ rope} \rho_w A_{wire\ rope}\right) U^2}{2g \times \left(\rho_w V_{wetted_{buoy}} - m_{buoy} - m_{wire\ rope}\right) + \rho_w \left(C_{L,buoy} A_{wetted_{buoy}} + C_{D,wire\ rope} A_{wire\ rope}\right) U^2}\right] \quad \text{Equation 1.15}$$

According to Equation 1.15, the tilt angle of the buoy has a nonlinear relationship with the flow velocity. However, researchers at the CHTTC routinely observe the tilt of tear

shaped buoys and are within 10% to 20% error of the measured flow surface velocity: the brain can somehow over time establish a correlation. It remains difficult for the human brain, however, to process the tension felt in the mooring line and equate that to velocity. Researchers are not accurate and just report the mooring line is too much to hold with hands and arms.

The actual relationships between the tilt angle and the flow velocity and between the tension force and the flow velocity are more complicated. Thus, the assumptions made for the force balance of mooring buoy are oversimplified for actual applications. First, the wire rope, or the cable of mooring buoy underwater forms a curved shape because cables are easy to bend and the drag force variation due to various frontal area of each infinitesimal section along the bended shape. Second, large rotational motion of the buoy may occur if the buoy is not axisymmetric. Third, the connection point between the buoy and the cable may allow motion by moment when the connection is not clamped. Lastly, in real cases, the flow shows waves and oscillations at free surface. The waves and oscillations in flow introduce the added mass effect and Froude-Krylov force onto a floating object, like mooring buoy, because of acceleration in flow [12]. In addition, and Equation 1.12 contain the tilt angle term. This means that the tension force of wire rope is a dependant variable to the tilt angle of the buoy. Therefore, to implement tension force measurement data to estimate flow velocity, combining tilt angle measurement data together will provide a more completed picture.

1.4.2. Vibration acting on mooring line of tear-shape buoy

When fluid flows across an immersed cylindrical body, vortices are shed periodically from the surface of the body. This behaviour varies pressure on the structure periodically which causes vibration. The cylinder body can vibrate in both transverse

and parallel to the flow. In the transverse direction, the dominating frequency is called the vortex shedding frequency. In the direction parallel to the flow, the dominating frequency is called the in-line vibration frequency and is twice the vortex shedding frequency. The vortex shedding frequency is often represented by a dimensionless form called the Strouhal number, St, where f_w is the vortex shedding frequency, and D is the characteristic diameter:

$$St = \frac{f_w D}{U} \qquad \text{Equation 1.16}$$

In the range of Reynolds number between 10^2 and 10^5, Strouhal number is 0.2 on average for a slender cylindrical body [13]. With the known Strouhal number and the characteristic diameter of the vibrating body, the vortex shedding frequency has linear relationship with the flow velocity.

The amplitude of the vortex-induced vibration increases when the flow velocity increases. This is because when the flow comes onto the cylinder body, the pressure difference between the front of the body and the back occurs. The wire rope of mooring buoys is a slender cylinder body. Therefore, the vortex shedding frequency generated by the flow passing the cable linearly increases when the flow increases. The amplitude of the vibrating cable also increases when the flow increases. CHTTC researchers feel the frequency on the mooring lines with their hands, but the brain cannot correlate the vibration they feel to the flow velocity.

1.4.3. Sound of water flowing over tear-shape buoy

As water flows over a floating buoy, the free surface breaks, and there is sound of water. As higher kinetic energy of water collides onto the buoy, the sound of impact becomes louder. At the same time, at the back of the object, water flow generates sound to fill the gap around the back of the object. This sound from the back also increases when the flow is faster. Experienced researchers at the CHTTC can infer

flow velocity from sound on tear-shape buoys as their brain developed a correlation over time.

1.5. Objectives

The objective of this research is to evaluate the potential of using a tear-shape buoy to commercially develop a rugged flow velocity meter using up to four methods: tilt, tension, vibration, and sound to correlate river surface velocity. Specific objectives are:

1. Obtain a calibration curve for each method by curve-fitting the data of each variable against flow velocity using repeated measurements,
2. Estimate flow velocity from the calibration curves to evaluate accuracy of each method, and
3. Evaluate the four methods to determine if they could practically be used to obtain a P95 estimation of non-instantaneous flow velocity for hydrokinetic energy resource assessment.

1.6. Methodology

Tear-shape prototype instrumented buoys were designed and assembled. Four sensors are used to measure tilt of the buoy, mooring line tension, mooring line vibration amplitude, and sound around the buoy. Prototypes were tested in the water tunnel located at the University of Manitoba. The measurement for collecting data was repeated to find the reliability of each method. With the measurement data for each variable, a scatter plot for each variable in terms of the water flow velocity was created. Figure 1.6 summarizes the methodology of this research.

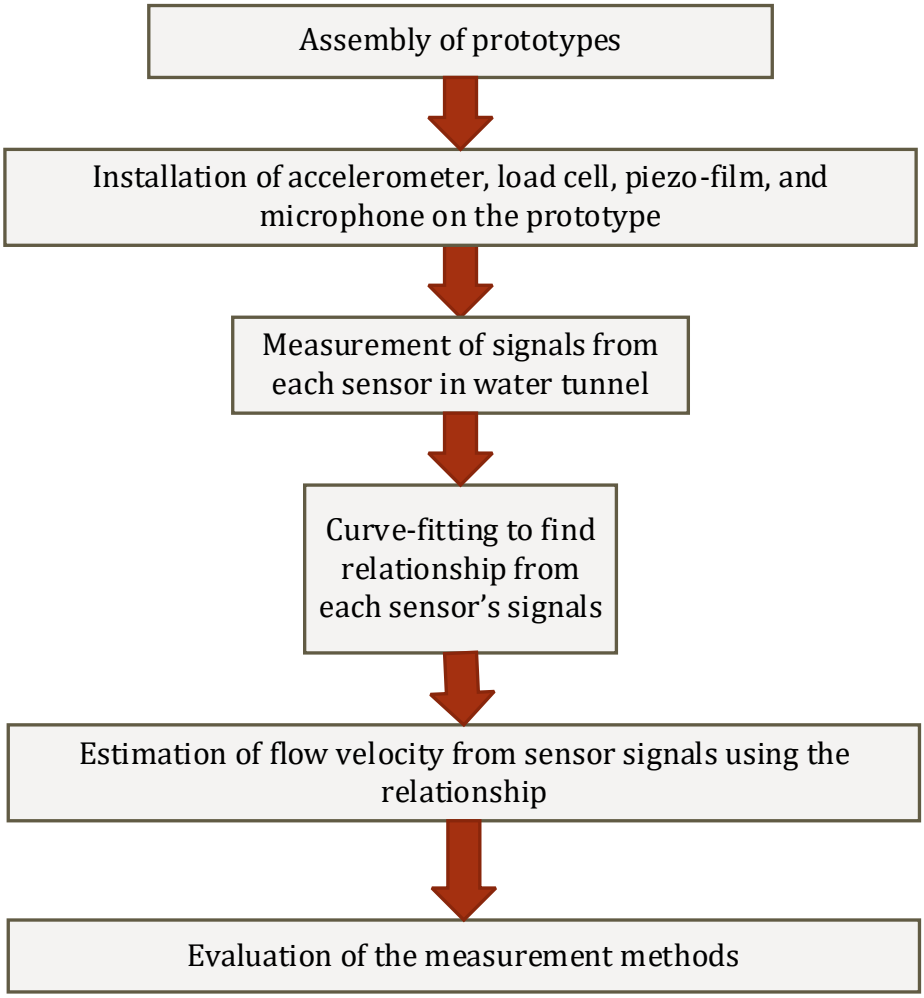

Figure 1.6: Flow chart of the methodology for testing in the water tunnel

1.7. Research contributions

This research provides novel concepts for non-instantaneous flow velocity measurement techniques to enable measurements of long-term energetic river velocities that are rugged, as none of the sensors are exposed to the elements. Instead of using typical acoustic and turbine flow meters, the proposed low-cost methods of flow velocity measurement use a moored buoy. Sensors are installed inside the tear-shape buoy. Development of these methods could contribute to better site assessment for river hydrokinetic resources at lower costs and design requirements,

as the instrument is a typical moored buoy which is easy to deploy. When the long-term data of flow velocity is finally available, the probability density function can be obtained. Using this statistical function, flow velocity and hydrokinetic power could then be estimated within a 95% confidence interval. This would assist communities to implement hydrokinetic turbines and obtain financing.

Note that another method of measuring flow using sight by looking at eddies on the surface of the water can be used to determined flow velocity at the CHTTC by people. Work is ongoing to apply the Space Time Image Velocimetry (STIV) method to quantify the flow velocity. This approach is out of the scope of this thesis as it cannot be integrated into a buoy.

1.8. Outline

Chapter 2 reviews literature on flow velocity measurement techniques. Chapter 3 describes the prototype buoy, sensors with specification and installation, measurement procedures in water tunnel. Chapter 4 shows results of the measurements, analysis, and discussions of the results. Chapter 5 concludes the research and provides recommendations. The Appendix contains the coding script used for the Arduino microprocessor and demonstrate how sensor readings are stored within the instrumented prototype buoys.

2. Literature review

In this section, studies are reviewed that investigate flow velocity measurement techniques that can be used for rivers, studies that investigate the relationship of tilt, tension, vibration, and sound with velocity measurements, and methods that focus on long-term flow velocity measurements.

2.1. Velocity measurement techniques for open channel flow

Flow velocity has been measured using various methods that are contact and contactless with the water. These methods measure flow velocity accurately but remain difficult for collecting data for a long duration in energetic river sites.

2.1.1. Acoustic instruments

Acoustic instruments such as Acoustic Doppler Velocimeter (ADV) and Acoustic Doppler Current Profiler (ADCP) have been commonly used to measure flow velocity in open-channel flow. These instruments use the Doppler effect, which is the principle of the frequency change in waves propagating from the wave source to the observer as the relative distance between the source and the observer changes. These instruments have no contact with the flow at the point of measurement. However, the instruments are exposed to the river elements as they are immersed into the flow.

ADV emits acoustic waves to water particles reflecting the wave back to the ADV measurement control volume. Using the difference between the wave frequency going to the particles and emitted back to the ADV, the flow velocity is obtained by:

$$U = \frac{f_{doppler}\frac{c}{2}}{f_{source}}, \qquad \text{Equation 2.1}$$

where $f_{doppler}$ is the frequency of the wave after doppler effect is applied, f_{source} is the original wave frequency emitted from ADV, and c is the speed of sound in water.

The Nortek Vector-300 is a typical ADV product which samples water particles in a volume of 900-3500 mm^3 at a rate of up to 64 Hz with an accuracy of ±0.5% [14]. To compensate the motion of ADV because of water drag force, an inertial motion unit including an accelerometer and a magnetometer is also contained in the ADV device.

ADVs have been used in laboratories, estuaries, riverbeds, and shallow rivers. Chanson et al. [15] measured flow velocity of an estuarine zone of a creek using ADV. To eliminate effects of disturbances which cause the flow to become unsteady, a post-processing method of error detection and removal was used. Chanson et al. [16] used ADV to measure the turbulent velocity of tidal bore in a laboratory setting. Sulaiman et al. [17] measured velocity at the near bottom of sand-gravel bed rivers containing bulging clast.

Gunawan et al. [18] performed a resource assessment to evaluate the temporal variation of the flow velocities, flow directions, turbulence intensities, and power densities for installing a hydrokinetic turbine for tidal energy generation. They used ADV to collect data covering two months at the design hub height of a hydrokinetic turbine. From the data, an average horizontal flow velocity of 1.4 m/s is obtained. One remarkable finding is that the power densities calculated from the two months data is one order of magnitude larger than the data reported in the US government.

ADCP sends acoustic waves to a much larger volume of the flow compared to the ADV. ADCPs are often used for measuring flow discharges by integrating flow velocity over a cross section of a river [19]. The discharge can either be obtained by traversing an

ADCP from one riverbank to the other riverbank or fixing ADCPs at the side of a riverbank. As compared to ADVs in terms of the accuracy in velocity and discharge measurement, ADCPs show agreement within 5% [20]. ADCPs can measure turbulence intensity, large scale turbulence, and vertical velocity profile from the free surface to the riverbed of the flow [21]. The Nortek – Signature55 is a typical ADCP that profiles current up to 1000 m long at a maximum sampling frequency of 55 kHz [22].

Acoustic devices have been implemented to measure velocity of energetic flows to estimate hydrokinetic energy potential. However, the devices are difficult to deploy and secure at a site for a long term, and processing and evaluating the measurement data is more complex [23]. D'Auteuil [11] measured flow velocity using ADV and ADCP securing these to a measurement platform which were fixed and mobile. He described the challenges in the motion of mobile platform and ADV because of surface wave due to energetic flow. Moreover, he described the drag force and the vibration acting on components of the measurement designs are challenging to withstand. For the mobile platform, a pole to secure acoustic devices needs to be firm to withstand the large forces. In addition, vibration can cause fatigue and crack propagation into the structure holding the device. To reduce vibration, the stiffness of the holding arm should be increased, and a streamline design implemented.

2.1.2. Measurement methods with water contact

Flow velocity measurement has been performed by devices which are intrusive to the flow. These types of velocity measurement devices are anemometer, Pitot tube, and tilt current meter.

Anemometers or propeller meters are relatively simple devices that obtain flow velocity by measuring the rate of rotation of an impeller. These devices contain a

magnetic proximity sensor which detects the movement of rotating components, such as a propeller mounted on a freely rolling shaft on the end of support strut, as shown in Figure 2.1. They are inexpensive, easy to use, and rugged, but the resolution is temporal and relatively poor in spatial aspect. Hot-wire anemometers, shown in Figure 2.2, are a specialized type of anemometer. These devices utilize a relationship where the heat transfer from a heated element is approximately proportional to its temperature difference. Therefore, when a heated fine wire is placed in a flow, as the flow velocity increases, the temperature of the heated wire decreases, and the wire's electrical resistance also decreases. Hot-wire anemometers measure the electrical conductivity of the wire, which has an inverse relationship with the electrical resistance, to obtain flow velocity.



Figure 2.1 Propellor meter [24]

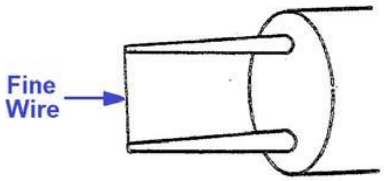

Figure 2.2 Hot-wire anemometer [25]

The Pitot tube measures pressure and relates this to flow velocity. Almeida et al. [26] developed an adapted Pitot tube and evaluated its performance in a laboratory water tunnel at flow velocities from 0.2 to 2.0 m/s. The results showed that measurements over 1.2 m/s are valid to be used because of the uncertainties in the static and total head. Comparison of the results to ADV showed that up to 15% differences in the mean velocities between the two measurement methods are obtained.

A measurement device, called a tilt current meter, shown in Figure 2.3, was developed by Lowell Instruments [27]. The shape of the device is a cylindrical rod which is placed under water and anchored to the bottom of water with a short tether. The data

logger is mounted in the core of the device containing 3-axis accelerometer and 3-axis magnetometer to measure tilt and bearing. This device measures flow velocity using the relationship between flow velocity and the tilt angle of an anchored object caused by drag of the flow. Using calibration coefficients obtained from the relationship, the orientation data is converted into flow velocity.



Figure 2.3: Tilt current meter [27]

Anemometer and Pitot tube types of flow velocity measurement devices can obtain flow velocity instantly. However, they are difficult to use to collect long-term data for analysis of seasonal variation in flow velocity. The tilt current meter can collect long-term measurement data because it can stay longer at the same location. Nevertheless, a tilt current meter cannot measure near-surface flow velocity because the device is mounted on the riverbed. Since streamwise velocity is slower closer to the bottom because of boundary layer effect, the device may underestimate flow velocity. Also, even though tilt current meter design claims to be rugged, the sensors in the data logger may be affected by the mixed sediments in turbulent flow when collecting measurement data over a long term.

2.1.3. Measurement methods without water contact

Flow velocity measurement methods without water contact are interesting techniques that researchers focus on as they may be more appropriate for long-term measurements in difficult conditions. The methods are optical techniques to estimate flow velocity of water. They can be classified by optical medium for analysis: laser velocimetry, velocimetry using unmanned aerial systems such as drones, and satellite velocimetry.

Laser velocimetry analyzes the streamwise movement of water particles in terms of time between laser beams or displacement for a certain time interval by tracing. Particle Image Velocimetry (PIV) [28] and Laser Doppler Velocimetry (LDV) [29] are commercially available methods. PIV measures the displacements of groups of particles of two- or three-dimensional flow between a short time interval determined by laser pulses or camera shutter. A two-dimensional flow velocity map generated by PIV for instantaneous time shows the structure of the flow field of velocity vectors. As for LDV, a defined space is divided into equally small defined spaces. The number of small spaces, n, times small time interval, dt, is measured by the apparatus because the particles move over n spaces dx periodically. LDV uses the Doppler effect to use the frequency shifts between the source of the particles and the observer, which are related to the velocity vector of moving particles.

Laser velocimetry is impractical for river flow velocity measurements because the side planes of river flow, except for the free surface, are unreachable. PIV needs to be accessible on two side planes out of the four side planes of flow stream: top, bottom, left, and right. PIV needs to project a laser beam to illuminate particles from one side, and the camera captures the particles' image on the perpendicular side plane of the laser beam. LDV can project two laser beams from one side and receive at the same

side. However, the LDV needs to have a firm fixture to withstand wind and precipitation for long term measurements. This is difficult to construct.

Instead of using laser to illuminate seeded particles to obtain images to estimate flow velocity, free surface floating particles or deformations due to ripples or waves are captured by a camera located at riverbank. Unmanned aerial vehicles such as drones with cameras are also deployed in the air to capture images by facing the cameras to the free surface. Large Scale Particle Image Velocimetry (LSPIV) [30], Space Time Image Velocimetry (STIV) [31], and Particle Tracking Velocimetry (PTV) are typical flow velocity measurement methods tracking particles on the river water surface.

Compared to PIV, LSPIV noninvasively measures the flow velocity field in two dimensions without seeding particles to river. LSPIV uses large areas of images recorded by a camera mounted at riverbank from oblique angles to the free surface of the flow. To analyze the images to estimate flow velocity, the removing process of distortions or displacements of those images is processed [32]. An assessment of the accuracy of LSPIV is made by comparison with ADV. Muste et al. [33] obtained error up to 10% in measured flow velocity in field conditions using LSPIV when compared with ADV at the same site of measurement. STIV, an advanced method of LSPIV, uses tracking free surface particles in one dimension instead of two dimensions [34]. This makes STIV performs faster than LSPIV. In terms of accuracy in velocity measurements, PTV needs to capture only a few particle-like tracers in the field of view [35]. This means PTV can measure flow velocity easier and more accurately than LSPIV.

Satellite image data has also been used instead of images captured by a camera. Legleiter et al. [36] used PIV to estimate surface flow velocities from satellite video of

a broad and sediment-rich river in Alaska. Instead of seeding artificial particles on the water surface, definite water surface features generated by naturally driven sediment boil vortices were trackable from frame to frame as they flow. The data went through refining procedures including stabilization, geo-referencing, image preprocessing, PIV analysis with a correlation algorithm, and postprocessing of PIV result.

One research addressed developing smartphone applications to find flow velocity. Lüthi et al. [37] developed a smartphone app to calculate amount of drained water for water management in irrigated agriculture. They used measured water level, surface flow velocity, and the channel geometry to calculate the drained water amount. For the surface flow velocity measurement, images are captured by a standard camera at intervals of two seconds. Those images are logged as data every ten minutes. The smartphone app separated moving image content from stationary image content. This app feature did not use any artificial flow tracers to alleviate the effects of background properties such as sunlight movement, waves, or ground features.

Even though the above noncontact measurement methods to obtain flow velocity data have been developed in the last decades, implementation to measure data for over a year to develop a probability distribution function within 95% confidence interval is still difficult to achieve.

2.2. Vortex-induced vibration

The behaviour of vortex-induced vibration acting on a bluff body against the velocity of fluid flow has been analyzed by researchers who are interested in estimating the vibration impact on structures. They separate the analysis into the amplitude and the frequency. As a result of the experiments at different velocities, they found regimes

in the behaviour of amplitude and frequency in terms of flow velocity divided by the natural frequency, f_N, of the vibrating body and the characteristic diameter, D, of the body. This velocity is a dimensionless velocity, U^*, is given by:

$$U^* = \frac{U}{f_N D}, \qquad \text{Equation 2.2}$$

$$f_N = \frac{1}{2\pi}\sqrt{\frac{k}{m + m_A}} \qquad \text{Equation 2.3}$$

where k is the spring constant, and m_A is the added mass.

Based on the stages of amplitude and frequency of vortex-induced vibration, Nakamura et al. [38] classified vortex-induced vibration into several categories and levels. First, vibration induced by crossflow is divided into two geometric groups. The first group is bending vibration of circular cylinder objects, and the second group is ovalling vibration of cylindrical shells. The bending vibration is also divided into whether the vibration occurs by steady flow or oscillating flow. The overall behaviour of vortex induced vibration is shown in Figure 2.4. The vibration induced by steady flow can also be further classified into four categories in terms of dimensionless velocity:

1) Forced vibration by Karman vortex shedding
2) Synchronization accompanied by Karman/symmetric vortex sheet
3) Turbulence-induced vibration
4) Vibration induced by tip vortex in high flow velocity regime

In the first category of the induced vibration by steady flow, vibrations can occur in transverse or parallel to the flow. The vibration parallel to the flow, called in-line oscillation, occurs when the dimensionless velocity is below four, as shown in Figure 2.5, where the higher Reynolds number of the flow initializes the amplitude earlier.

When the Reynolds number of the flow is below 1.2×10^3, in-line vibrations are not induced in water [39].

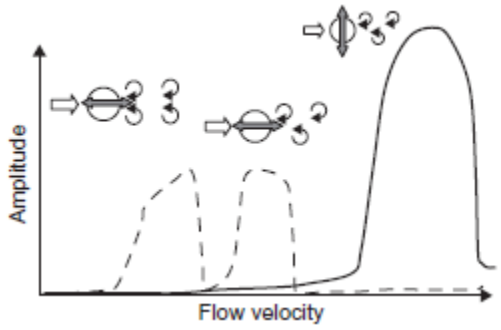

Figure 2.4: Overall behavior of vortex-induced synchronization including both in-line and transverse oscillations [38] where the legend is "- -": in-line oscillation; "—": transverse oscillation

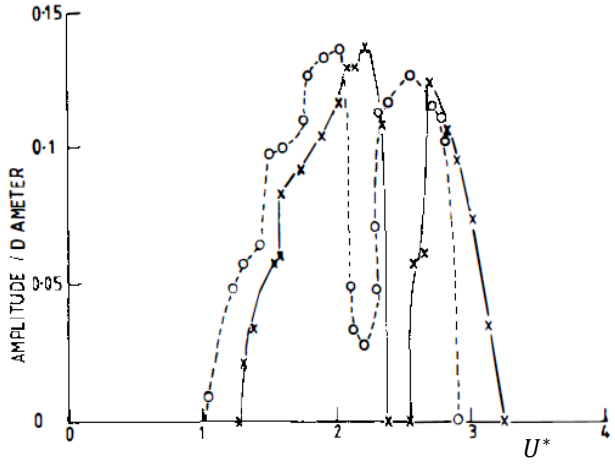

Figure 2.5: Vortex-induced in-line oscillations of a flexible cantilevered circular cylinder in water when $U^* < 4$ [40]. ∘, $Re=6\times10^5$; ×, $Re=6\times10^4$

The in-line vibration introduces symmetric vortex shedding, of which frequency is twice as the Karman vortex shedding frequency. In air flow, the amplitude is not often observed [41]. However, in water flow, if the mass ratio of displaced water to the mass of the floating body is substantially higher, high amplitude of in-line vibration can occur [42].

When the dimensionless velocity is greater than four, the amplitude of the vibration transverse to the flow starts to increase. As the flow increases, the Karman vortex shedding frequency also increases. At the same time, the natural frequency of the body is close to the vortex shedding frequency. Then, the vortex shedding frequency synchronizes with the natural frequency. This is called lock-in. Synchronization also occurs for the in-line vibration accompanied by symmetric vortex shedding when the amplitude of the in-line vibration increases.

Outside the synchronization region of both symmetric and Karman vortex shedding, the cylinder body gets affected by components over a wide band of frequency. If the natural frequency of the cylinder body is completely separated from the shedding frequency of both symmetric and Karman, the cylinder body will vibrate by the wide band components closer to the natural frequency.

At high dimensionless flow velocities beyond the lock-in regime for both symmetric and Karman vortex shedding, much larger amplitude of vibration occurs because of the vortices generated at the tip of the cylinder body. These vortices' shedding frequency is one-third of the Karman vortex shedding frequency.

Feng [43] conducted a study on vibration amplitude and its frequency in the transverse direction on a perpendicular cylinder in wind tunnel. The purpose of the study was to know how vortex-induced vibration of the structures in wind, such as bridges and chimneys, occurs at different wind speeds. In the study, he not only demonstrated that an increase in the dimensionless flow velocity on the cylinder body synchronizes the Karman vortex shedding frequency with the cylinder frequency, but he also found out the hysteresis in the amplitude measurement. The amplitude was higher when the flow velocity increased from a lower flow velocity

and lower when the flow velocity decreased from a higher flow velocity, as shown in Figure 2.6.

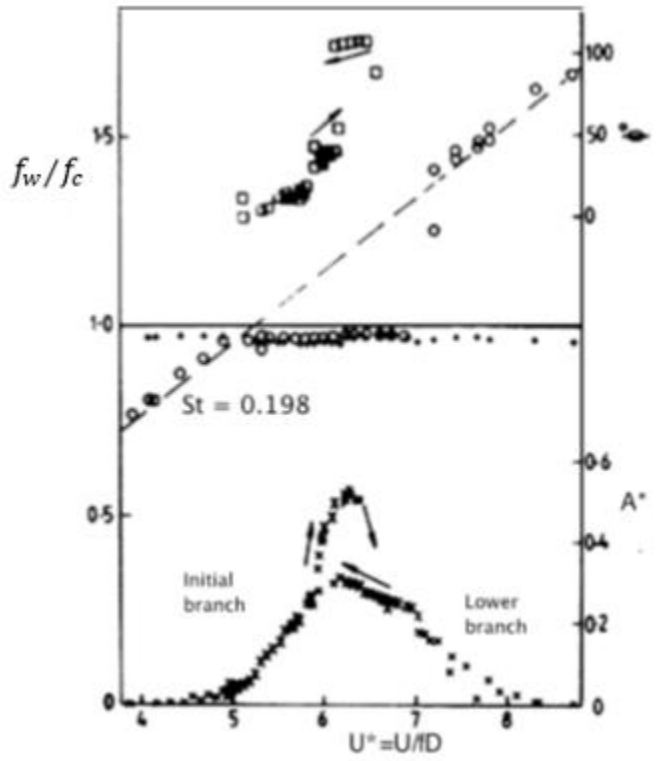

Figure 2.6: Oscillation characteristics for a freely vibrating circular cylinder in air, where the legend is ◯: vortex shedding frequency; +: cylinder frequency; □: phase angle; ×: oscillation amplitude; ϕ°: phase angle between fluid force and cylinder's displacement; f_w: vortex shedding frequency; f_c: oscillating frequency of cylinder; A*: amplitude ratio (A*=A/D) [43].

Several studies on low mass-damping system for offshore structures were conducted. These studies introduced the mass-damping term, $m^*\zeta$. This term is a nondimensionalized value derived by multiplication of two terms: 1) the mass ratio, m^*, of the cylinder mass, m_c, to the displaced fluid mass, $\frac{1}{4}\pi\rho_f D_c^2 L_c$, of the cylinder and 2) damping ratio, ζ, as shown below, where δ is the logarithm microphone decrement:

$$m^*\zeta = \frac{m_c \times \zeta}{\frac{1}{4}\pi\rho_f D_c^2 L_c};\ \zeta = \frac{\delta}{\sqrt{(2\pi)^2 + \delta^2}}, \qquad \text{Equation 2.4}$$

Where ρ_f is the density of the displace fluid, D_c is the diameter of the cylinder, and L_c is the length of the cylinder.

Khalak et al. [44] studied vortex-induced vibration on a flexibly mounted cylinder body with low mass-damping system and found that the initialization of synchronization, or the point of increasing the vibration amplitude, occurred at least one order of dimensionless velocity less than Feng [43] when the low mass-damping system was 1/30 to Feng's system. Khalak et al. [45] also concluded that the lock-in range increased in lower mass-damping system, and that the amplitude of the branch where the peak amplitude is also increased, as shown in Figure 2.7.

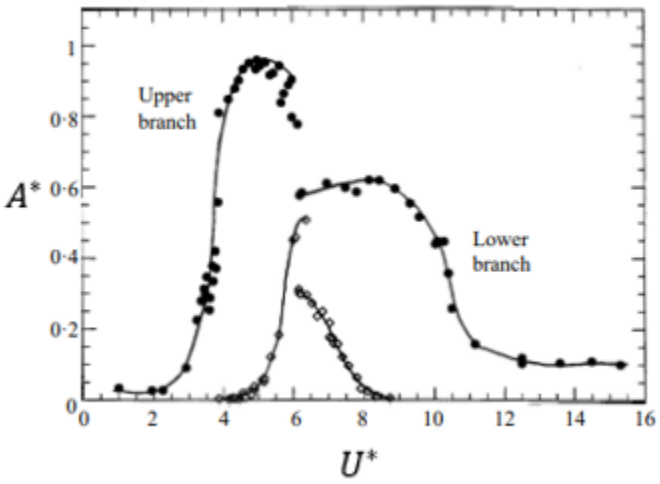

Figure 2.7: Comparison of transverse vibration amplitude between Khalak's study and Feng's [44] where the legend is ●: Khalak's study; ◇: Feng's study.

As for the frequency, the effect of mass ratio is an important factor to change the behavior of frequency response. Khalak et al. [46] measured frequency response for mass-damping, $m^*\zeta$, of 0.013, of which mass ratio, m^*, is 2.4. The response, as shown in Figure 2.8 and Figure 2.9, showed that when the mass ratio is smaller, the lock-in

region, where the cylinder oscillation frequency synchronizes with the Karman vortex shedding frequency, is wider than when the mass ratio is higher. Figure 2.8 and Figure 2.9 includes the frequency ratio, $f^* = \frac{f_W}{f_N}$, of the vortex shedding frequency to the natural frequency. Also, the synchronized nondimensional frequency also reached 1.5 when the mass ratio is smaller. The added mass effect causes the difference in frequency response as the mass ratios changes. As the dimensionless velocity increases, the added mass effect decreases. This increases the natural frequency of the cylinder body.

There is no reference that could be found that used the Karman vortex shedding frequency to measure flow velocity.

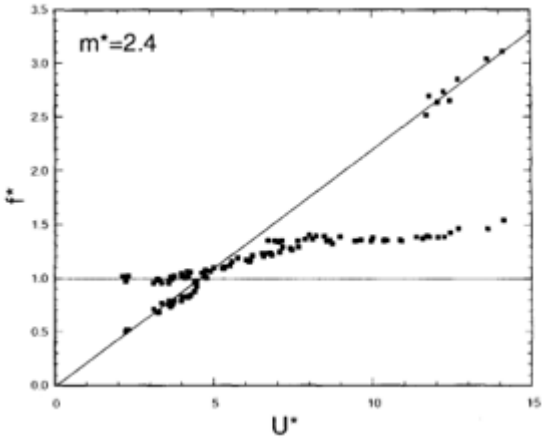

Figure 2.8: Frequency response f^* for m^*=2.4 [46].

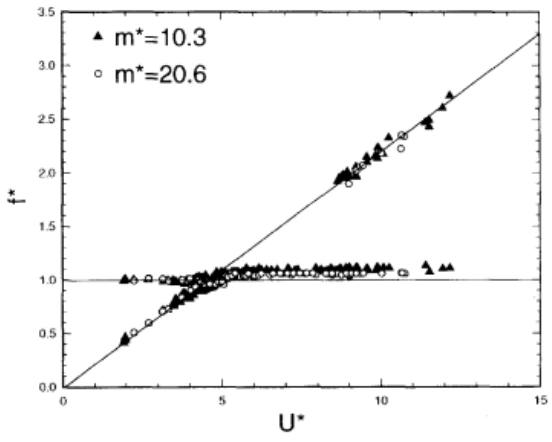

Figure 2.9: Frequency response f^* for m^*=10.3 and m^*=20.6 [46].

2.3. Sound level

One study documented that there is a positive correlation between sound and flow rate of water. H.E. Jacobs et al. [47] measured the sound of tap water and the corresponding flow rate to find a mathematical relationship between them. Using Fourier transforms of data in the frequency domain, the flow rate of water is

estimated from the obtained function of measured sound signals. After verification of the result against five independently recorded data sets, the average error was 15%. This result is relatively less accurate than currently available flowmeters.

2.4. Instrumentation

Instrumentation is the collective term of designing measurement systems. The values of physical parameters such as temperature, pressure, and force are obtained by instruments. Instrumentation can be divided into three components: 1) sensors, 2) signal conditioners, and 3) displays [48]. Sensors or transducers are the devices that transform physical parameters in equipment or environment into numerically quantified signals. It is necessary to amplify or filter these raw signals because of small magnitudes and unwanted noises. Signal conditioners amplify the magnitudes of raw signals and filter noises to help visualize the signals of physical parameters. The signals after the signal conditioners are displayed, recorded, or analyzed further to obtain the information of interest.

2.4.1. Tilt measurement using accelerometer

As explained in Reference [49], tilt is the angle of orientation of an object in x, y, and z axis. Tilt is measured by accelerometers that measure the acceleration of gravity in x, y, and z axis. Pitch and roll angles define the angles of accelerometers. Pitch, θ_{tilt}, is the angle between the x-axis of the accelerometer and the ground. Roll, ϕ, is the angle between the y-axis of the accelerometer and the ground. The diagram of pitch and roll is shown in Figure 2.10.

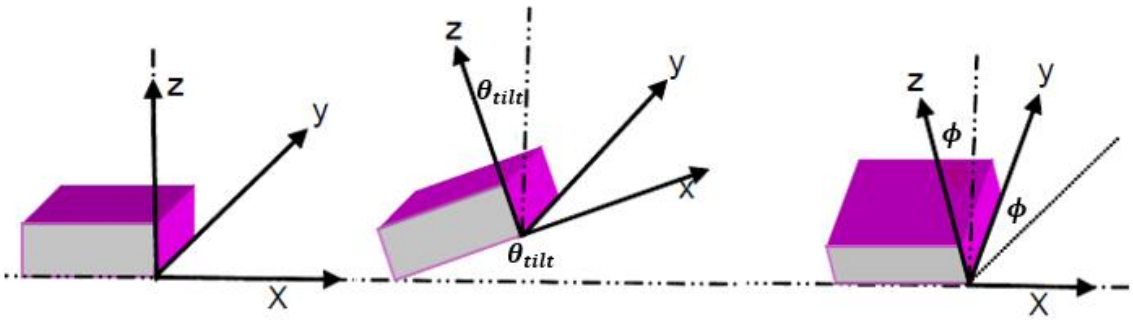

Figure 2.10: Pitch and roll angle of object [49]

$$\theta_{tilt} = \arctan\left(\frac{A_x}{\sqrt{A_y^2 + A_z^2}}\right), \quad \text{Equation 2.5}$$

$$\phi = \arctan\left(\frac{A_y}{\sqrt{A_x^2 + A_z^2}}\right), \quad \text{Equation 2.6}$$

where $A_x, A_y,$ and A_z are acceleration in x, y, z-components. The resultant acceleration of the three components is equal to 1 g (9.81 m/s^2).

$$\sqrt{A_x^2 + A_y^2 + A_z^2} = 1\ g \quad \text{Equation 2.7}$$

As shown in Figure 2.11, accelerometers consist of five basic elements inside [50]:

- Mass
- Spring suspension
- Damping
- Displacement sensor
- Frame

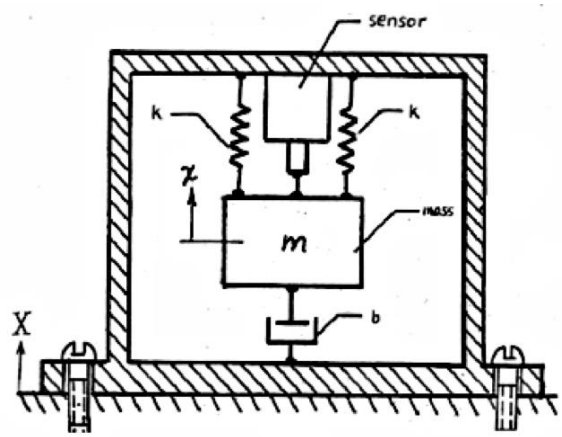

Figure 2.11: Basic structure of an accelerometer [50]

As explained in Reference [51], the principle on how accelerometers operate is that when the frame of the accelerometer moves, the inertia force of the proof mass causes deflection in the proof mass. The displacement sensor for each axis measures the displacement between the proof mass and the frame. The displacement is converted to acceleration in x, y, and z-axis. The three acceleration components are taken by the multiplexer to convert the current signals into voltages. After amplifying the voltage signals, the analog voltage signals are converted into digital output signals to be displayed. The overall diagram of the operation of accelerometers is shown in Figure 2.12.

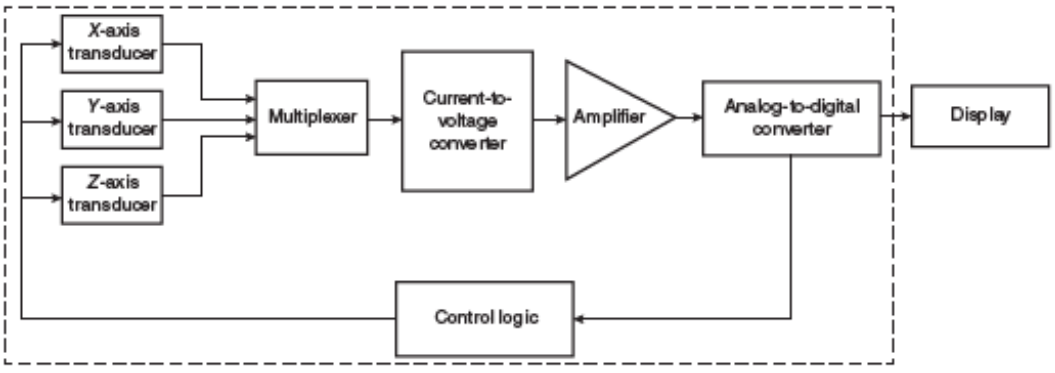

Figure 2.12: Block diagram of three-axis accelerometer including built-in A/D converter [51]

2.4.2. Force measurement using strain gauge

Force is defined as a vector of the amount of compression or tension applied to an object. The force, F, per unit area perpendicular to the force direction, A, is called stress, σ. Below a certain level of stress, the material changes its length proportional to the applied force, as shown in the equation below. When the applied force is removed, the material returns to its original length. The force sensors, or load cells, measure the strain, the ratio of change in the length of the object material to its original length because of the applied force.

$$\sigma = \frac{F}{A} = E\epsilon = E\frac{\Delta l}{l_0}, \qquad \text{Equation 2.8}$$

where σ is the stress, E is the elastic modulus of the material, and ϵ is the strain, l_0 is initial length of the object, and Δl is the change in length of the object. The measurement system for strains is visualized in Figure 2.13.

Strain is measured by strain gauges. Among various kinds of strain gauges, the commonly used metal strain gauges are electrically resistive. The strain detected by strain gauges from the object of interest causes a change in its electrical resistance. As the object deforms, it not only geometrically changes, but it also microstructurally changes.

$$\frac{dR}{R_0} = \epsilon(1 + 2\nu) + \frac{dQ_R}{Q_{R_0}} \qquad \text{Equation 2.9}$$

where R is electrical resistance, ν is Poisson's ratio, and Q_R is resistivity.

The change in resistance is detected by measuring voltage output from the Wheatstone bridge circuit. The resistance change generated by the strain of strain gauges is too small to measure directly from the voltage output of the circuit. Therefore, the voltage signals from strain gauges need amplification to make the outputs convenient to analyze. The amplified voltage signals are proportional to the change in resistance and proportional to the strain. Finally, the voltage signals are displayed in analog or digital form or recorded in storage.

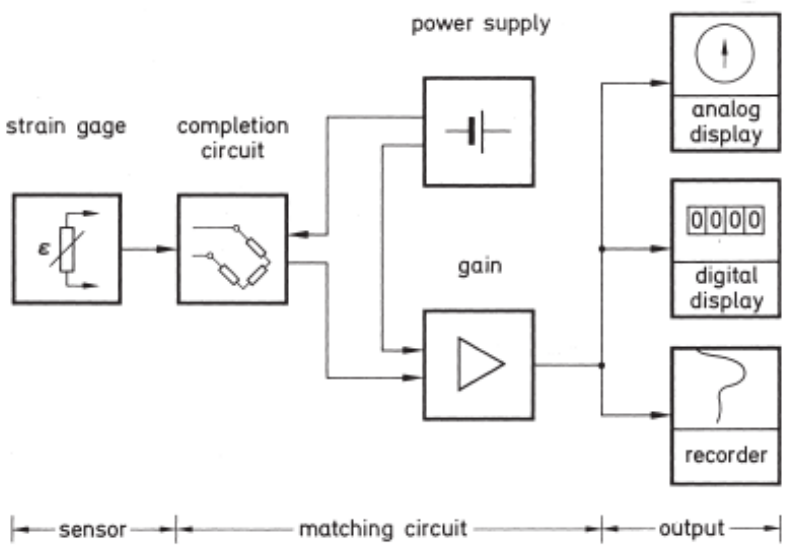

Figure 2.13: Measurement system for strains with a strain gauge [52]

2.4.3. Vibration measurement using piezoelectric sensor

As explained in Reference [48], piezoelectric sensors use the mechanism of piezoelectricity, which is the generation of electric charge, Q, when a material mechanically deforms due to an external force. The relationship between the electric charge and the external force load is proportional.

$$Q = d_{3n} * F \; where \; F = \sigma_n * A_{piezo} \; (n = 1, 2, or \; 3), \qquad \text{Equation 2.10}$$

where d_{3n} is the piezoelectric coefficient for the axis of applied stress, n is the mechanical axis of the applied stress, σ_n is the stress applied in n^{th} axis, and A_{piezo} is the conductive electrode area of the piezoelectric sensor. When $n = 1$, it is the longitudinal direction, $n = 2$ means the width (or transverse) direction, and $n = 3$ means the thickness direction [53].

The output voltage, V_{piezo}, of the piezoelectric sensor is proportional to the generated electric charge:

$$V_{piezo} = \frac{Q}{C_{piezo}}, \qquad \text{Equation 2.11}$$

where C_{piezo} is the capacitance of the piezoelectric sensor. The output voltage signals are used for detecting periodic external force, like vibration.

An interface circuit is required to optimize the piezoelectric sensor signals [53]. To design the circuit, first, the frequency range and signal amplitude over the dynamic range of interest is to be considered. Second, an appropriate load input resistance is to be selected to make sure the low-end operating frequency and to minimize signal loss because of the loading effect. Lastly, an operational amplifier is required to amplify sensor signals.

As explained in Reference [53], operational amplifiers can be used in either two modes: charge mode or voltage mode. When a long cable is required between the piezoelectric sensor and electronics, a charge-mode amplifier, shown in Figure 2.14, is beneficial because the output voltage of the amplifier does not include the effect of the cable capacitance. The magnitude of the output voltage of charge amplifier is:

$$V_{out} = \frac{Q}{C_f}, \qquad \text{Equation 2.12}$$

where C_f is the feedback capacitance of charge amplifier. The cut-off frequency is:

$$f_{cutoff} = \frac{1}{2\pi R C_f} \qquad \text{Equation 2.13}$$

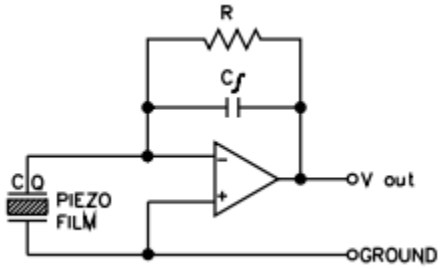

Figure 2.14: Charge amplifier for piezoelectric sensor [53]

3. Measurement data collection in water tunnel

To develop the velocity meter using tilt, mooring line tension, vibration amplitude, and sound, a prototype buoy is assembled. One sensor for each variable is selected and installed in the prototype buoy. Then the prototype buoy is deployed on different flow velocities in the water tunnel. Using the buoy, measurement data for each variable at different flow velocities is collected. The relationship of each variable with the flow velocity is first analyzed. After finding the relationships, a calibration curve for estimation of the flow velocity from each variable can be obtained from measurements. For the two variables of tilt and mooring line tension, a simplified force balance analysis is performed for estimation of the relationship of the flow velocity with tilt and mooring line tension using software ProteusDS. This software is used to simulate the velocity meter to determine the relationship of the flow velocity with tilt and mooring line tension numerically.

3.1. Prototype buoy of rugged long-term velocity meter

The prototype buoy of the velocity meter consists of three major parts: canister, tear-shaped buoy, and wire rope as shown in Figure 3.1. The canister includes an Arduino microcontroller board, as shown in Figure 3.2, which is assembled inside as shown in Figure 3.3. The tear-shaped buoy is assembled along the axial pipe. At the end of the axial pipe, the wire rope is connected by a clamp. Since the prototype buoy is to be durable to prevent damages due to collisions with rigid materials that flow in the water, parts except for the rubber buoy are made of 304 and 316 stainless steel, galvanized steel, and zinc-plated steel. Also, all the metal parts are welded together.

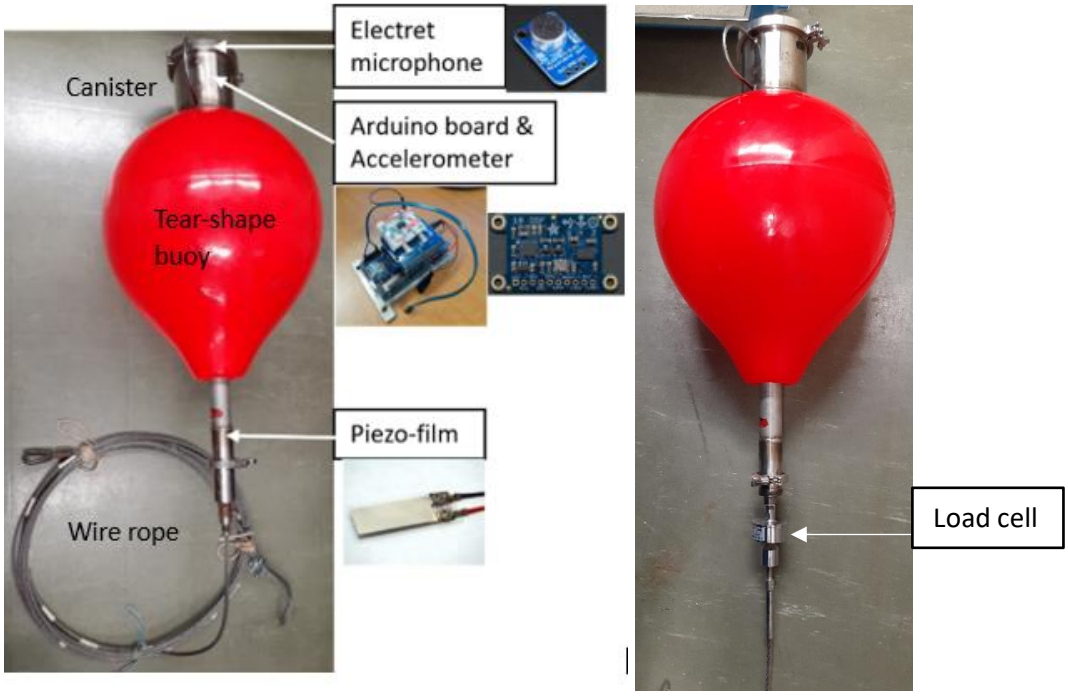

Figure 3.1: Prototype buoy of rugged long-term velocity meter before and after including load cell

The prototype buoy is a rugged, long-term flow velocity meter and may contain one or more sensors internally. No sensor is exposed to water as to avoid damage by solid materials flowing in the river. The strain gauges to measure tension of the wire rope was planned to be installed at the inner side of the axial pipe. However, the strain of the axial pipe portion did not exceed a few millionth [mm/mm] when the maximum possible mooring line tension load (~50 kg) was applied. Therefore, a load cell that has an inner portion which elongates enough to measure strain and stress in higher resolution is used instead. Load cells in the market usually have the signal transmission cable come out from the side of the load cell. To avoid water contact to the load cell signals, the outlet location of the signal cable is a customized deign with the cable located at the top plane of the centre axis of the load cell. Thus, the cable can directly go all the way to the canister to connect to the Arduino board without contacting water in a watertight arrangement with no seal requirements.

3.2. Instrumentation

To measure tilt, mooring line tension, vibration amplitude, and sound, four sensors are used: an accelerometer, a load cell, a piezo film sensor, and an electret condenser microphone, respectively. The Arduino microcontroller board takes each sensor signal and stores them onto a storage card, shown in Figure 3.2. Arduino is a low-cost, open-source electronics platform accompanying user-friendly hardware and software [54]. The Arduino board can read signals from sensors and write on a storage card. The process and organization of data acquisition is available through the Arduino coding script.

The accelerometer generates digital signals, and the other sensors generate analog signals. The analog signals become digital signals when passing through analog-to-digital converter embedded in the Arduino board. Because the Arduino board (Arduino mega) is a 10-bit microprocessor, digitized signals are represented in a range from 0 to 1023. An Arduino code is uploaded in the Arduino board to control each sensor, sampling frequency, analog-to-digital conversion, and measurement data storage. The Arduino code is shown in Appendix A.

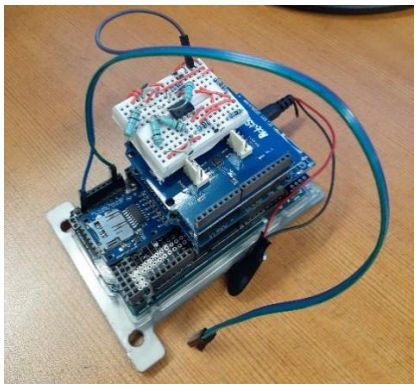

Figure 3.2: Arduino board including a prototyping shield, a strain gauge ampifier and a charge amplifier circuit board



Figure 3.3: Inside of cylinder canister viewed from top of the prototype buoy

3.2.1. Accelerometer

A 3-axis Micro-Electromechanical Systems (MEMS) accelerometer LSM303DLHC of Adafruit 10-degree of freedom Inertial Measurement Unit (IMU) breakout [55] [56] is used. It is assembled on a prototyping shield, (a layer for assembling parts,) of the Arduino board as shown in Figure 3.4.

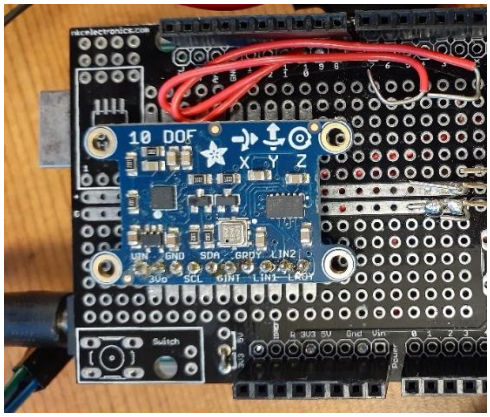

Figure 3.4: 10-degree of freedom IMU breakout assembled on a prototyping shield

This accelerometer has 16-bit data output resolution, and the full scale is selected to be $\pm 4g$. At the selected full scale, the linear acceleration sensitivity is 2 mg/ least significant bit. The analog supply voltage is available from 2.16 V to 3.6 V. Since the Arduino board supplies voltages at either 3.3 V or 5 V, 3.3 V of supply voltage is supplied to the accelerometer. The accelerometer is factory-calibrated, and a level tool is used to test if the accelerometer is calibrated.

For this research, we measure tilt (pitch) and roll angle by the 3-axis acceleration components. The tilt angle is obtained by the equation written in the Arduino code. The roll angle is needed for vibration measurements by piezo-film sensor. The accelerometer is aligned with the axis of the mooring buoy. Thus, it measures the tilt angle of the axial pipe of the velocity meter. Its sampling rate is selected to be 0.66 Hz.

3.2.2. Customized load cell

A customized Anyload load button 247BST1 is used, as shown in Figure 3.5. Its output sensitivity is 2.02 mV/V, and the full scale of the load cell is 200 kg. The Ingress Protection rating (IP) is 69. This means the load cell is waterproof. Since the recommended supply voltage is between 5 V and 12 V, 5 V from the Arduino board is supplied to the load cell.

The shape of the right end portion of the load cell is male thread for connection to the axial pipe portion of the prototype buoy. Since the load cell is fully submerged during the measurements, the thread gap between the load cell and the female thread part to the axial pipe is taped with thread seal tape. As the load cell is no different than the steel mooring cable, we assume this to have minimal impact on instrument survivability.



Figure 3.5: Customized load button load cell

A Strain gauge Wheatstone bridge amplifier is assembled on the Arduino board. Gain is set to be 495. Since the unit of the tension force is preset in pounds force, [lb], to be calibrated, mooring line tension force is represented in pound force.

3.2.3. Piezo-film sensor

To measure vibration, a piezo-film, a cantilever-beam-shaped piezoelectric sensor LDT1-028K/L [57], shown in Figure 3.6, is used. The capacitance of the sensor is 1.38

nF, the film thickness is 28 μm, and the conductive electrode area is 12 mm × 30 mm = 360 mm^2.

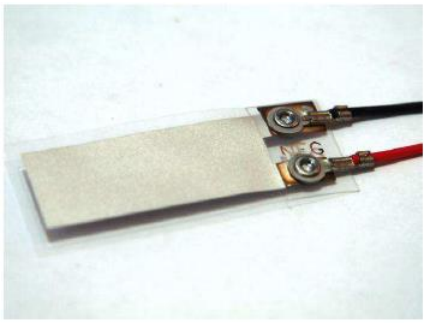

Figure 3.6: General-purpose piezo-film

The sensitivity of piezo-film sensors depends on the orientation of the sensor with respect to the axial and vertical direction as shown in Figure 3.7. The reference angle (0°) is aligned with the centre normal line of the Arduino board plane. It is also indicated outside the canister and the axial pipe as shown in Figure 3.8. Because the piezo-film sensor is attached on the inner surface of the axial pipe of the device as shown in Figure 3.9, the magnitude of vibration is affected by cosine of the angle between the reference angle and the orientation of the axial pipe. The angle of orientation of the axial pipe is recorded with the accelerometer as a roll angle. The magnitude corrections are achieved by using the roll angle data.

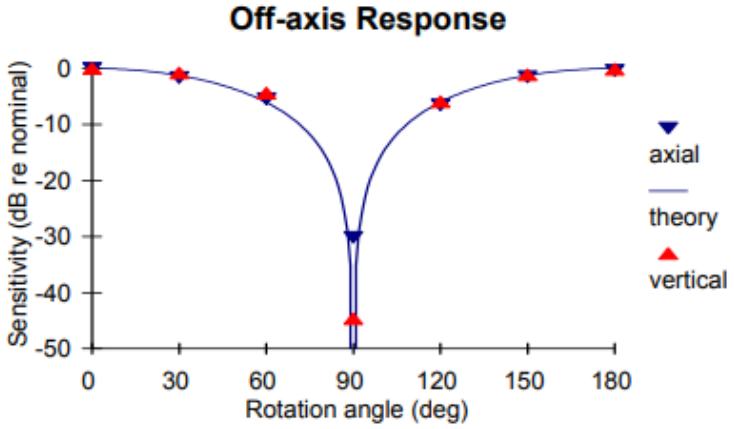

Figure 3.7: Sensitivity of piezo-film sensor in different rotation (orientation) angles [58]



Figure 3.8: Indication of the reference angle, 0°, on buoy axial pipe and canister



Figure 3.9: Three piezo-film sensors installed on inner wall of buoy axial pipe: one piezo-film with flat washers attached both sides and aligned with the indicated reference angle is used.

Flat washers are used to increase the sensitivity of low-frequency signals. Also, the raw output voltage signal of the piezo-film sensor is amplified by the charge amplifier shown in Figure 3.10.

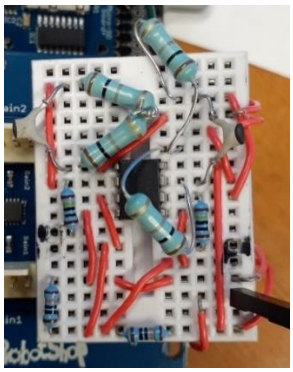

Figure 3.10: Charge amplifier for two piezo-film sensors

3.2.4. Electret condenser microphone

To measure background sound around the velocity meter, electret condenser microphone MAX4466 [59] [60] [61], shown in Figure 3.11, is used. This microphone can be operated in supply voltage of either 3.3 V or 5 V from the Arduino board, but since the noise in the sound voltage signal is lower for 3.3 V of supply voltage, 3.3 V is chosen.



Figure 3.11: Electret condenser microphone MAX4466 [59]

The gain is available from 25 times to 125 times. To minimize extra filtering of sensor data due to unnecessary noise, the gain is set to be 25 times. In general, microphones capture sound better when the source of sound is closer. To capture background sound of the velocity meter, the microphone should be located outside of the canister. However, the microphone cannot work with water contact. Figure 3.12 and Figure 3.13 show the previous stainless-steel lid which could not transmit sound to the microphone located inside the cylinder. Therefore, a lid is designed for the microphone so that the microphone can capture sound outside as shown in Figure 3.14 and Figure 3.15.



Figure 3.12: Top view of old cylinder canister lid

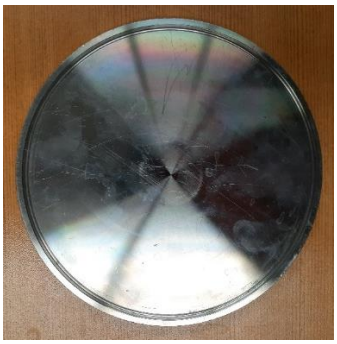

Figure 3.13: Bottom view of old cylinder canister lid



Figure 3.14: Top view of new cylinder canister lid



Figure 3.15: Bottom view of new cylinder canister lid

A tarp of waterproof but accepting air flow in and out is used so that the microphone does not contact water but captures the sound outside the canister.

3.2.5. Arduino code

The Arduino code is used for determining how frequently and when sensor's signals are to be recorded in the storage card. The code is originally adapted from a code of Global Positioning System (GPS) sensor board. In this research, the GPS feature is excluded. The code script is classified into two major parts: setup and main loop.

When the code runs, in the setup part, sensors are initialized to be ready for reading signals. The pin number for each analog sensor is assigned. Also, the storage card is activated to record sensor readings. The accelerometer's signals are digital while all

the other sensor's signals are analog. Since digital and analog sensors cannot read signals at the same time, the digital accelerometer reads signals first and then all the other analog sensors read signals.

Sampling frequency and time are assigned in the code before running the setup part. For digital sampling, sampling frequency of each reading and number of samples per one cycle of running the main loop are selected. For analog sampling, instead of the number of samples per cycle, sampling period per one cycle is selected.

The accelerometer is connected to a software first to initialize the functioning. Then, range of acceleration was selected. Also, there are options to choose the mode in terms of resolution. "High" resolution is selected. Based on the settings, the accelerometer measures acceleration in x, y, and z components. These measurements are used in the equations of pitch and roll, as shown in Equation 2.5 and Equation 2.6. The acceleration, pitch, and roll angles are recorded in the storage card.

As for the load cell, it is first calibrated at zero load and then with a reference load. Using the corresponding readings, the actual load is estimated by linear interpolation. Piezo-film sensor and electret condenser (electrostatic capacitor-based) microphone signals are recorded in the storage card without applying any formulas. Before starting measurements, the code is uploaded on the Arduino board so that the sensors connected to the Arduino board may read sensor signals according to the instructions in the uploaded code. The code is available in Appendix A which shows the important functions.

3.3. Data collection in water tunnel

Tests to collect data of signals from four sensors are conducted in a water tunnel, shown in Figure 3.16. The water tunnel in the Renewable Energy Lab in the University

of Manitoba can generate water flow velocity from 0.1 to 1 m/s by adjusting the water pump frequency using the remote control shown in Figure 3.17. The calibration plot to adjust flow velocity using pump frequency is provided by the laboratory coordinator as shown in Figure 3.18. The water tunnel is 2 m long, 0.62 m wide, and 0.6 m high.



Figure 3.16: Water tunnel in the Renewable Energy Lab



Figure 3.17: Remote control of water tunnel

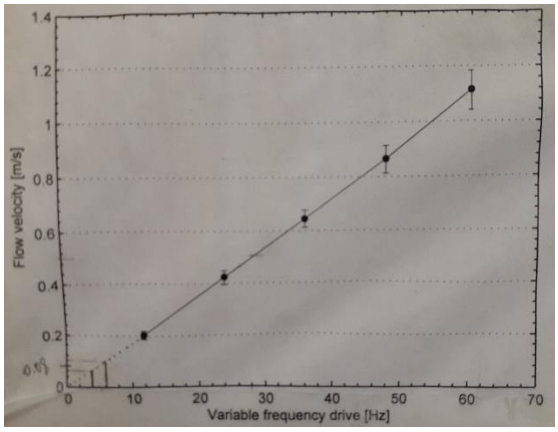

Figure 3.18: Calibration plot to obtain flow velocity from pump frequency

Before assembling the customized load cell, forty-eight measurements are performed using the prototype buoy without the load cell. These measurements contain five to seven trials used for preparation for measurement system setting. For each trial, the

flow is increased from zero to 1 m/s by 0.1 m/s increments, and measurement data for each velocity is collected for 40 seconds. For each measurement, four 20-lb steel bars at the bottom of the water tunnel are used for anchoring the prototype buoy, as shown in Figure 3.19. The steel bars can only be slanted because the wounded wire rope is placed under the steel bars. This increases the frontal surface area of the stacked steel bars against the flow. This means more drag force acts on the steel bars. Because of this drag force, more weights than normal are required. At 1 m/s, the slanted steel bars started drifting. Therefore, the measurements were redone after making sure that the steel bars are secure.

After assembling the customized load cell, fifty-three measurements are performed as shown in Figure 3.20. The measurements are for obtaining mooring line tension data from the load cell. The setup for measurements in the water tunnel was all the same as before assembling the load cell. The only difference is that three steel bars are enough to secure the steel bars not to drift. Also, the steel bars are less slanted than before the load cell is assembled.

3.3.1. Variable conditions in data collection

Several variable conditions in the prototype buoy tested in the water tunnel contribute to increase errors in the measurement data. First, the angular orientation with respect to the central axis, or the roll angle, of the prototype buoy is not controllable at a fixed angle when the flow velocity is zero. Also, some angular orientations are unstable when stationary because of non-uniform mass distribution inside the stainless-steel canister where the Arduino board and batteries are located. Since the piezo-film vibrates like a cantilever beam on one angular portion of the inner surface of the axial pipe, vibration acting on the piezo-film is not uniform in all orientations. Second, the tarp condition can vary in terms of moisture. When splashes

occur and water drops come to the tarp covering the microphone, the sound transmission through the tarp to the microphone diminishes. Therefore, according to the moisture of the tarp, sound measurements are divided into two cases: dry and wet. Dry means the tarp has no contact with water at all, and wet means a water drop is applied on the tarp.

3.3.2. Data collection procedures in water tunnel

The procedures of collecting measurement data for each measurement trial are described as follows:

1) The storage card is taken in the card socket assembled in the Arduino board. Also, six 1.5-V AA batteries (or a 9-V battery) assembled in a socket are connected to the Arduino board to power on.
2) After closing and locking the canister lid as well as connecting the microphone signal wires to the Arduino board, the time count using an app in a smartphone starts. The time count is used for comparing the time counted in the Arduino board, so that the measurement at certain flow velocity can be identified.
3) The prototype buoy is deployed on the water tunnel by anchoring the wire rope portion with the steel bars.
4) After turning on the water tunnel pump switch, measurement data is collected as increasing the flow velocity by 0.1 m/s by adjusting the pump frequency by the remote control. Figure 3.19-Figure 3.21 show the prototype buoy deployed in the water tunnel when the flow velocity is zero.

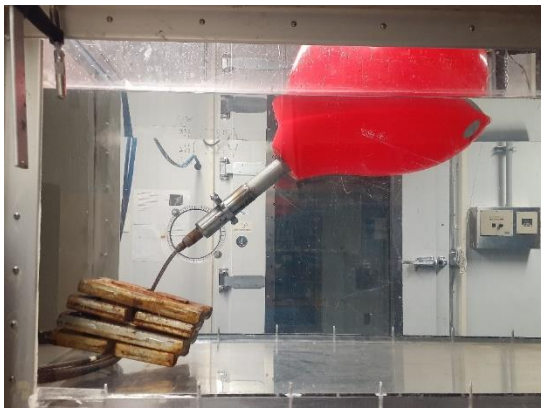

Figure 3.19: Side view of the prototype buoy anchored with steel bars in water tunnel before load cell assembled

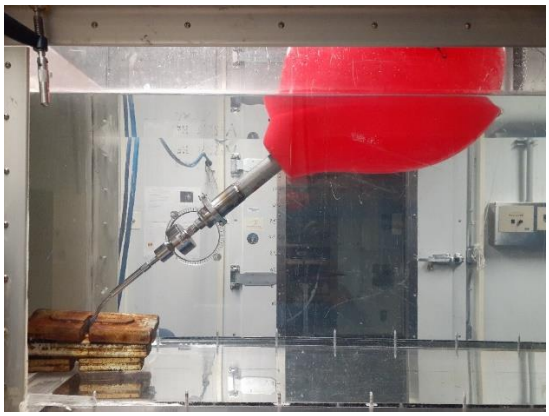

Figure 3.20: Side view of the prototype buoy in water tunnel after load cell assembled

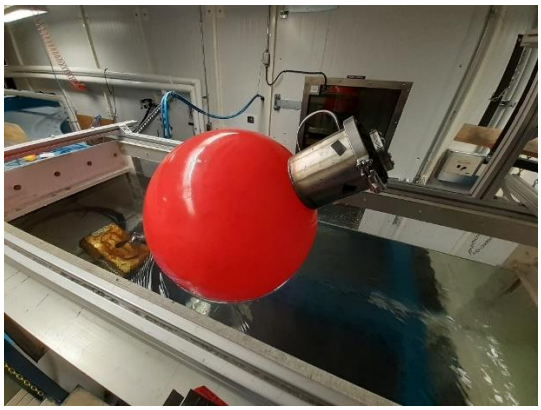

Figure 3.21: Top side view of the prototype buoy

3.4. Simulation to find relationship between mooring line tension and flow velocity

ProteusDS [62] is used to simulate the water flow around the prototype buoy to estimate tension on the wire rope. The obtained simulations are used to determine the relationship between flow velocity and tension on the wire rope of the prototype buoy at different flow velocities in the water tunnel and in the river. Figure 3.22 and Figure 3.23 show the examples of the prototype buoy simulations that ProteusDS provides.

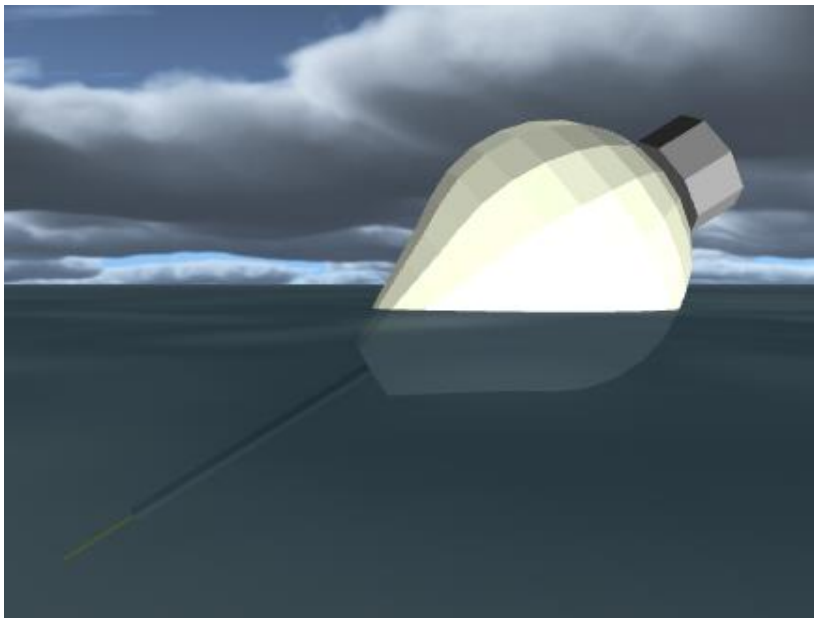

Figure 3.22: Prototype buoy simulation in water tunnel setting in ProteusDS

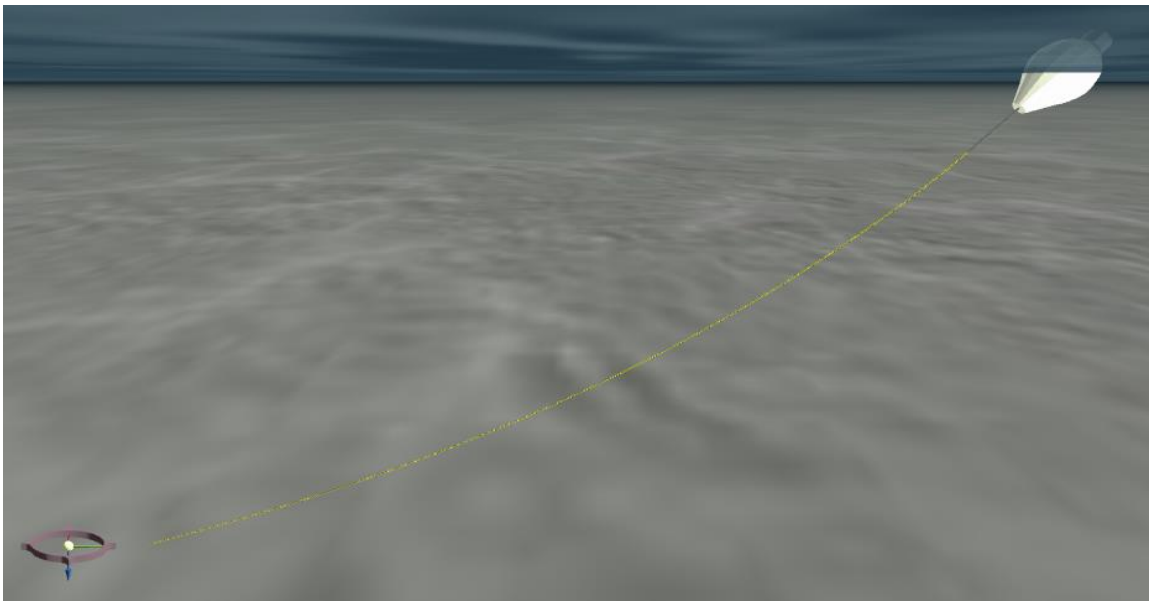

Figure 3.23: ProteusDS simulation of the velocity meter in river

Table 2 summarizes the differences between the water tunnel and river settings. The differences between the water tunnel and river settings are not only flow velocity and water depth. When the same prototype buoy is used, the length of the wire rope underwater is the major geometrical difference between the two settings.

Table 2: Differences between water tunnel and river in ProteusDS

	Water tunnel	River
Velocity range	0.1 – 1 m/s	0.5 – 4 m/s
Depth	0.45 m	10 m
Percentage of wire rope from the prototype buoy underwater	< 20 %	> 200 %
Wire rope orientation underwater	Straight	Curved

Features of the prototype buoy need to be defined. For surface buoy application, the simulation is divided into the rigid buoy and the wire-rope cable. For the rigid body, mass moment of inertia, center of gravity, and mass are defined. For the features of the rigid body, added mass coefficients, dimensions, drag coefficients, and number of mesh segments are defined in library section which is called for the rigid body. For cable or wire rope, boundary constraints, like which end to fix, fluid loading mode (either constant volume or surface integral mode), and cable segment defining mode are defined. The features of the wire rope include axial rigidity (the product of elastic modulus and cross-sectional area), drag coefficients, bending and torsional stiffnesses, diameter, density, buoyancy diameter, and compressive elasticity.

After defining the features of the objects, the initial position of the rigid body, which is the buoy and axial pipe portion, and the wire rope, is defined. The mesh count is defined. For river application, twenty meshes are selected. Another setting that ProteusDS simulation needs is connection setting between the objects. In general, the wire rope follows the floating rigid body. By assigning the location of the connection point in terms of the rigid body frame and setting the principal normal vectors for the clamped connection, the connection setting is complete. After assigning the simulation end time, ProteusDS simulation is ready to start.

After ProteusDS simulation finishes, the simulation video and numerical results are saved. The relationship between flow velocity and mooring line tension of the prototype buoy is analyzed. The results are discussed in Chapter 4.4.

3.5. Test matrix

Table 3 shows all the measurement trials with dates of measurement, recorded variables, and condition of the tarp on the canister lid. Since the total measurement trials are divided into two by the absence or presence of the load cell, as shown in Figure 3.19 and Figure 3.20, the first letter in each trial # is either A or B. Also, the condition of the tarp on the canister lid is divided into dry condition and wet condition.

Table 3: Test matrix. **A**: Measurement before load cell is installed; **B**: Measurement after load cell is installed; W: wet tarp; O: data collected.

Trial #	Date	Tilt	Tension	Vibration	Sound	Dry tarp	Wet tarp	**Trial #**	Date	Tilt	Tension	Vibration	Sound	Dry tarp	Wet tarp
A1-1	2021-09-15	O		O	O	V		**A7-4**	2021-12-17	O		O	O	V	
A1-2	2021-09-15	O		O	O	V		**A7-5**	2021-12-17	O		O	O	V	
A2-1	2021-09-22	O		O	O	V		**A7-W1**	2021-12-17	O		O	O		V
A2-2	2021-09-22	O		O	O	V		**A7-W2**	2021-12-17	O		O	O		V
A2-3	2021-09-22	O		O	O	V		**A7-W3**	2021-12-17	O		O	O		V
A3-1	2021-09-23	O		O	O	V		**A7-W4**	2021-12-17	O		O	O		V
A3-2	2021-09-23	O		O	O	V		**A7-W5**	2021-12-17	O		O	O		V
A3-W1	2021-09-23	O		O	O		V	**A8-1**	2021-12-20	O		O	O	V	
A3-W2	2021-09-23	O		O	O		V	**A8-2**	2021-12-20	O		O	O	V	
A3-W3	2021-09-23	O		O	O		V	**A8-3**	2021-12-20	O		O	O	V	
A3-W4	2021-09-23	O		O	O		V	**A8-4**	2021-12-20	O		O	O	V	
A3-W5	2021-09-23	O		O	O		V	**A8-5**	2021-12-20	O		O	O	V	
A4-1	2021-10-05	O		O	O	V		**A8-W1**	2021-12-20	O		O	O		V
A4-W1	2021-10-05	O		O	O		V	**A8-W2**	2021-12-20	O		O	O		V
A4-W2	2021-10-05	O		O	O		V	**A8-W3**	2021-12-20	O		O	O		V
A4-W3	2021-10-05	O		O	O		V	**A8-W4**	2021-12-20	O		O	O		V
A4-W4	2021-10-05	O		O	O		V	**A8-W5**	2021-12-20	O		O	O		V
A4-W5	2021-10-05	O		O	O		V	**B1-1**	2022-04-20	O	O	O	O	V	
A5-1	2021-11-02	O		O	O	V		**B1-2**	2022-04-20	O	O	O	O	V	
A5-2	2021-11-02	O		O	O	V		**B1-3**	2022-04-20	O	O	O	O	V	
A5-3	2021-11-02	O		O	O	V		**B1-4**	2022-04-20	O	O	O	O	V	
A5-4	2021-11-02	O		O	O	V		**B1-5**	2022-04-20	O	O	O	O	V	
A5-5	2021-11-02	O		O	O	V		**B2-1**	2022-04-25	O	O	O		V	
A6-1	2021-11-19	O		O	O	V		**B2-2**	2022-04-25	O	O	O		V	
A6-2	2021-11-19	O		O	O	V		**B2-3**	2022-04-25	O	O	O		V	
A6-3	2021-11-19	O		O	O	V		**B2-4**	2022-04-25	O	O	O		V	
A6-4	2021-11-19	O		O	O	V		**B2-5**	2022-04-25	O	O	O		V	
A6-5	2021-11-19	O		O	O	V		**B3-1**	2022-04-27	O	O	O		V	
A7-1	2021-12-17	O		O	O	V		**B3-2**	2022-04-27	O	O	O		V	
A7-2	2021-12-17	O		O	O	V		**B3-3**	2022-04-27	O	O	O		V	
A7-3	2021-12-17	O		O	O	V		**B3-4**	2022-04-27	O	O	O		V	

Table 3 continued

Trial #	Date	Tilt	Tension	Vibration	Sound	Dry tarp	Wet tarp	Trial #	Date	Tilt	Tension	Vibration	Sound	Dry tarp	Wet tarp
B3-5	2022-04-27	O	O	O		V		**B7-5**	2022-05-06	O	O	O		V	
B4-1	2022-04-29	O	O	O	O	V		**B7-6**	2022-05-06	O	O	O		V	
B4-2	2022-04-29	O	O	O	O	V		**B7-7**	2022-05-06	O	O	O		V	
B4-3	2022-04-29	O	O	O	O	V		**B7-8**	2022-05-06	O	O	O		V	
B4-4	2022-04-29	O	O	O	O	V		**B8-1**	2022-05-11	O	O	O	O	V	
B4-5	2022-04-29	O	O	O	O	V		**B8-2**	2022-05-11	O	O	O	O	V	
B5-1	2022-05-02	O	O	O	O	V		**B8-3**	2022-05-11	O	O	O	O	V	
B5-2	2022-05-02	O	O	O	O	V		**B8-4**	2022-05-11	O	O	O	O	V	
B5-3	2022-05-02	O	O	O	O	V		**B8-5**	2022-05-11	O	O	O	O	V	
B5-4	2022-05-02	O	O	O	O	V		**B8-6**	2022-05-11	O	O	O	O	V	
B5-5	2022-05-02	O	O	O	O	V		**B8-7**	2022-05-11	O	O	O	O	V	
B6-1	2022-05-04	O	O	O	O	V		**B9-1**	2022-05-12	O	O	O	O	V	
B6-2	2022-05-04	O	O	O	O	V		**B9-2**	2022-05-12	O	O	O	O	V	
B6-3	2022-05-04	O	O	O	O	V		**B9-3**	2022-05-12	O	O	O	O	V	
B6-4	2022-05-04	O	O	O	O	V		**B9-4**	2022-05-12	O	O	O	O	V	
B6-5	2022-05-04	O	O	O	O	V		**B9-5**	2022-05-12	O	O	O	O	V	
B7-1	2022-05-06	O	O	O		V		**B10**	2022-06-28	O	O	O	O	V	
B7-2	2022-05-06	O	O	O		V		**B11-1**	2022-07-08	O	O	O	O	V	
B7-3	2022-05-06	O	O	O		V		**B11-2**	2022-07-08	O	O	O	O	V	
B7-4	2022-05-06	O	O	O		V									

4. Laboratory measurement results and discussions

In this chapter, measurement data of tilt, mooring line tension, vibration, and sound signals collected in the water tunnel are presented. From each dataset for one variable, the relationship between the variable and flow velocity is analyzed. By curve-fitting each dataset, a calibration curve for each variable using the trendline feature in Excel is obtained. The obtained calibration curve is used for estimating flow velocity when a set of measurement data is given. Before using the calibration curve for each variable, the calculated residual is used to check if the calibration curve needs further transformation. Finally, each method is compared each other in terms of experimental errors, sensor quality, geometric complexity, and applicability to river environment.

4.1. Measurement data of four variables for identifying relationship with flow velocity

As explained in Chapter 3, each trial of measurement started from zero flow velocity and increased by 0.1 m/s every 40 seconds. After 40 seconds at 1 m/s, flow velocity is reduced back to zero. This is the end of each test. Before the customized load cell is assembled at the connection between the bottom end of the axial pipe and the wire rope as shown in Figure 3.20, the three variables, except for mooring line tension, are repeatedly measured forty-eight times which consists of seven times of measurement setup. After the load cell is assembled, tension signals are measured fifty-three times with nine times of each measurement setup. Plots containing all the measurements of each variable show how the variables are related to flow velocity.

Raw data stored in the storage card by the Arduino board is imported into Excel and the last 15 seconds of each 40 second interval data is used for the analysis. From the 15 seconds of data for each trial at each increment of flow velocity, tilt angle and tension signals are averaged and plotted in Figure 4.1 to Figure 4.3. For vibration and sound signals, output

voltage signals in 10-bit binary format are recorded in the storage card. The root mean square method, included in Equation 4.1, is applied for those signals to be converted into decimal values for analysis. In the equation, n is the number of signals in each trial at each increment of flow velocity, and supply voltage for piezo film is 5 V and for electret microphone is 3.3 V.

$$V_{output} = \frac{\sum_{i=1}^{n} \frac{|baseline\ reading - (sensor\ reading)_i|^2}{n}}{2^{10} - 1} * V_{supply} \qquad \text{Equation 4.1}$$

Plots of vibration and sound voltage signals after applying Equation 4.1 are shown in Figure 4.4 to Figure 4.7. For legends in Figure 4.1 to Figure 4.7, 'A' means before the load cell is assembled to the prototype buoy, and 'B' means after the load cell is assembled. The number next to the alphabet means different measurement setup. The next number means each trial, and 'W#' means wet condition of tarp on the microphone. If there is no 'W', it means the measurement setup is in dry condition for the tarp.

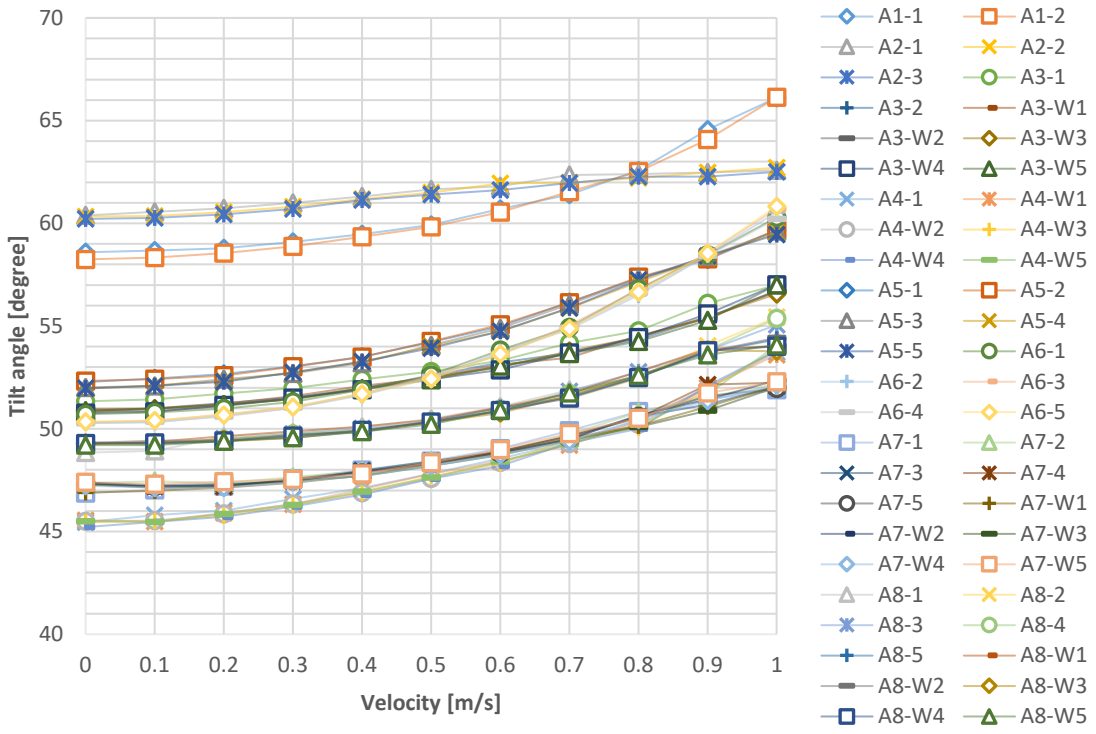

Figure 4.1: Forty-eight trials of tilt angle measurements vs. flow velocity before load cell is installed

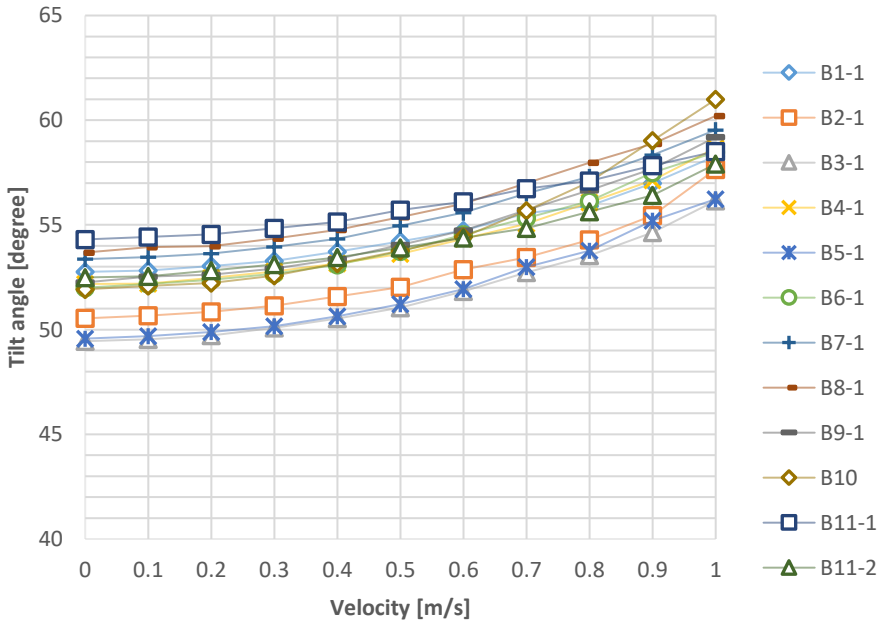

Figure 4.2: Selected trials of tilt angle measurements vs. flow velocity after load cell is installed

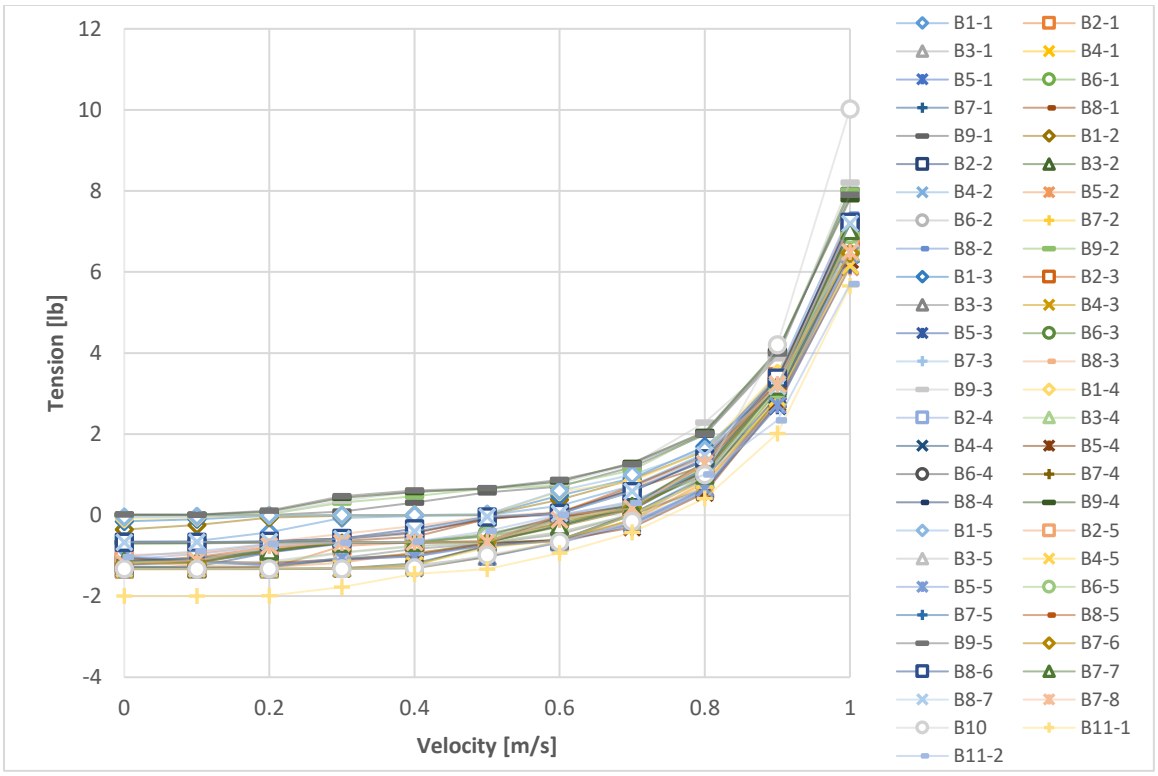

Figure 4.3: Fifty-three trials of mooring line tension measurements vs. flow velocity after load cell is installed

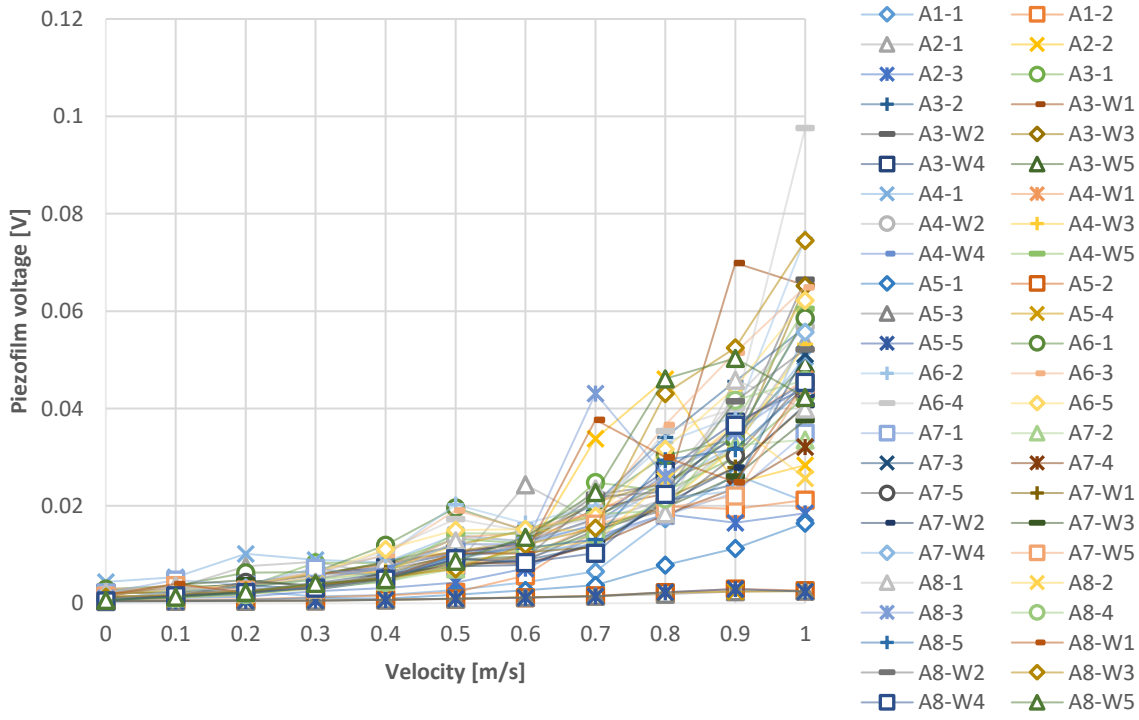

Figure 4.4: Forty-eight trials of piezo-film voltage measurements vs. flow velocity before load cell is installed

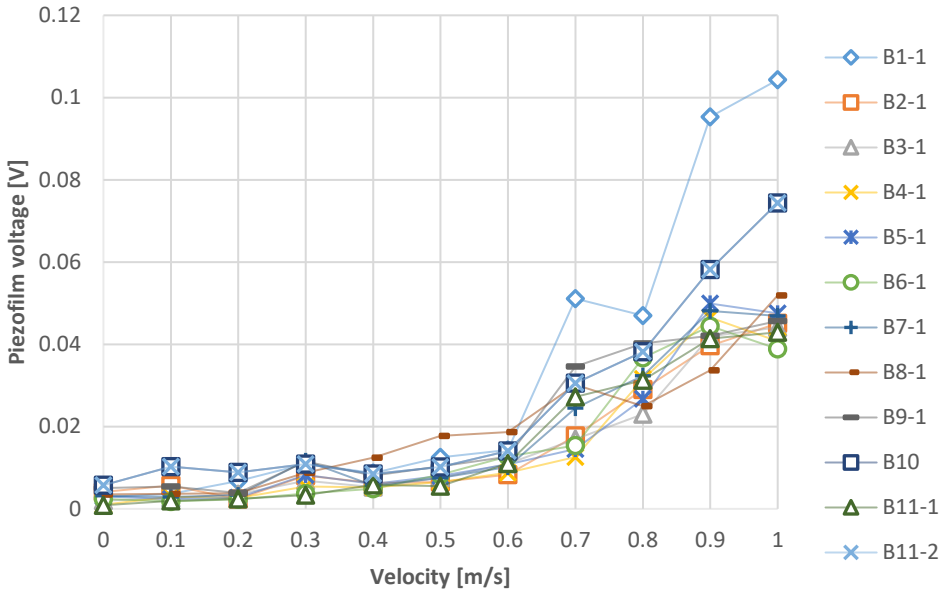

Figure 4.5: Selected trials of piezo-film voltage measurements vs. flow velocity after load cell is installed

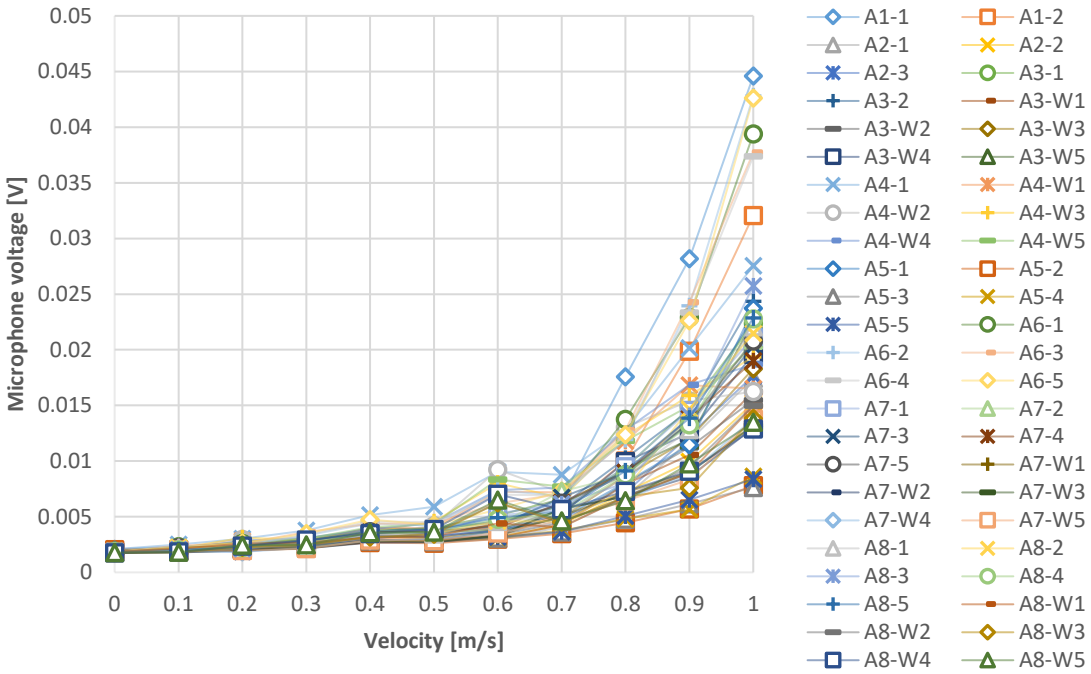

Figure 4.6: Forty-eight trials of microphone voltage measurements vs. flow velocity before load cell is installed

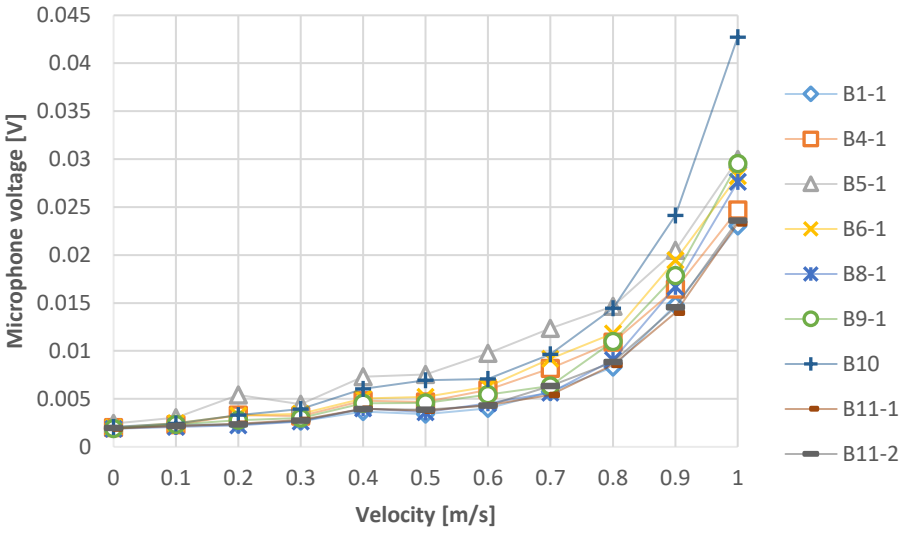

Figure 4.7: Selected trials of microphone voltage measurements vs. flow velocity after load cell is installed

The measurement data plots contain less deviations among the trials after the load cell is installed. This is because, before the load cell is used, the entire portion of 11-m wire rope, as it is shown in Figure 3.19, is laid at the floor of water tunnel for each setup. On top of the wound wire rope, the steel bars are laid for anchoring the prototype buoy. The wire rope is tied with a white rope which did not perfectly secure the wound portion of the wire rope. This made the wire rope portion between the steel bar anchor and the prototype buoy not perfectly fixed. This would have changed the initial state of the prototype buoy at zero velocity for each setup before the load cell is assembled.

4.1.1. Tilt angle

As predicted based on Equation 1.14, both Figure 4.1 and Figure 4.2 show the tilt angle of the prototype buoy increases nonlinearly when the flow velocity of water tunnel increases. The underwater geometrical structure of the prototype buoy before the load cell is installed is different from after the load cell is installed. However, definite differences in slope and the magnitude of tilt angle increase are not found when comparing between Figure 4.1 and

Figure 4.2. For further analysis, Figure 4.1 which contains more data is selected to be used to obtain the calibration curve.

In terms of the initial angular position of the prototype buoy, the prototype buoy in the water tunnel could start with any initial angle at zero flow velocity. However, when the surface of water is laid below the edge of the tip of the buoy, as shown in Figure 4.8, the flow pushes the buoy without increasing tilt angle as the flow increases, as shown in Figure 4.9. This behavior occurs because the buoy portion has its own moment with respect to the centre of buoy on water surface due to the heavy stainless-steel canister. Because of the moment, the buoy portion slanted more. Also, the tilt angle of the axial pipe of buoy and the tilt angle of the wire rope are not the same each other. For the trial when the tilt angle at zero flow was about 60°, tilt angle increased only by about 2° at 1 m/s of flow velocity, as well as the shape of the measurement plots in Figure 4.1 is not concave up like other curves of which the initial tilt angles were below 60°.

The initial tilt angle at zero flow was not easily controlled but ranges from 45° to 60° because the steel bars are heavy to move and difficult to lie at the bottom of the water tunnel to anchor the wire rope. That is why the initial tilt angle at zero flow for the first five trials, Trial A1-1 to A2-3, is bigger than 58°. Since all the other trials' initial angle is below 55°, the five trials are regarded as outliers and not included in further analysis.

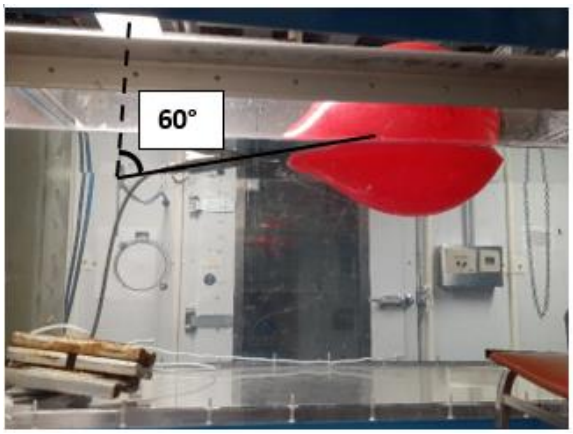

Figure 4.8: Flow velocity at 0 m/s when initial tilt angle is 60°

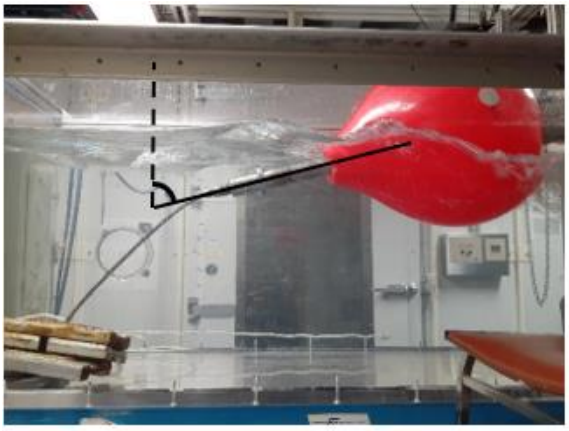

Figure 4.9: Flow velocity at 1 m/s when initial tilt angle is 60°

4.1.2. Mooring line tension

Figure 4.3 shows that the relationship between tension force on the wire rope and velocity is nonlinear. The results show that at velocities less than 0.3 m/s, the cable tension measured by the load cell is less sensitive to changes in velocity. The tension load at zero velocity ranges from -9 N (-2 lb) to 0 N (0 lb). Like the tilt angle measurements, the cause of this negative range is due to the measurement setup, especially when the steel bars are used as bottom anchors in the water tunnel. The measured negative cable tension at zero velocity is caused by the moment exerted by the prototype buoy's stainless-steel canister. Since the moment with respect to the buoy portion applies bending on the load cell, negative tension values are measured at low velocities.

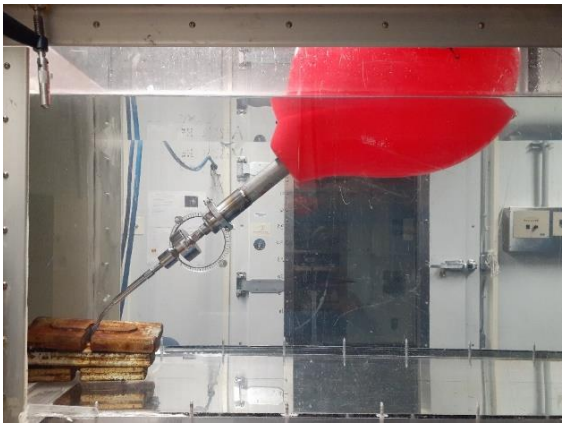

Figure 4.10: Flow velocity at 0 m/s when load cell is assembled

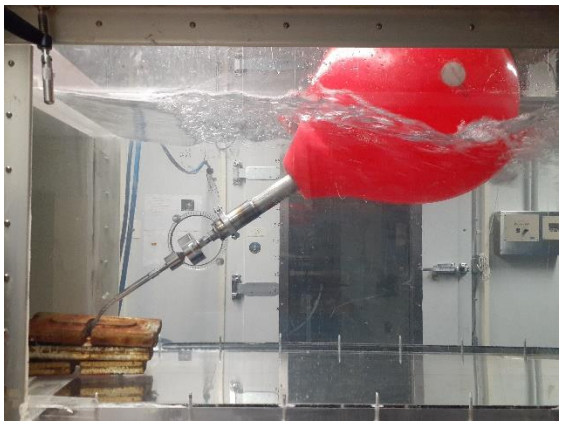

Figure 4.11: Flow velocity at 1 m/s when load cell is assembled

4.1.3. Vibration amplitude

Figure 4.4 and Figure 4.5 show that the vibration amplitude, which is reflective of the Strouhal frequency on the prototype buoy, nonlinearly increases as the flow velocity increases. Both figures show more deviations in data at higher velocities, but Figure 4.5 shows more fluctuations than Figure 4.4. The possible reason of more fluctuations is in less uniform characteristic diameter in the underwater geometrical structure of the prototype buoy due to the irregular shape of the load cell. For further analysis, the measurement data presented in Figure 4.4 is selected to obtain the calibration curve for vibration magnitude.

One of the major sources of error in vibration measurement is the orientation of the piezo film in the prototype buoy. As discussed in Chapter 3, the piezo film is attached at one angular position of inner surface of the axial pipe. Since the angular orientation of the prototype buoy is not controllable, for every time when the prototype buoy is set up to run the water tunnel, the sensitivity of piezo film may not be the same. Because the piezo film moves as a cantilever beam, the most sensitive direction for the piezo film to generate capacitance in the gap of the film is when the piezo film vibrates perpendicular to the film plane. To know the angular orientation of the axial pipe of the prototype buoy for every measurement, roll angle of the

prototype buoy is measured from the accelerometer, recorded, and applied to the vibration voltage signals by multiplying the cosine roll angle. As flow increases, the tilt angle changes. This also affects the sensitivity of piezo film because the orientation of the piezo film also changes.

4.1.4. Sound

Figure 4.6 and Figure 4.7 show that the relationship between the sound around the prototype buoy and the flow velocity is nonlinear. Since Figure 4.7 does not show any notable trend as compared to Figure 4.6, for further analysis, the measurement data in Figure 4.6 is selected to obtain the calibration curve for the sound.

There are several factors that affect the magnitude of sound around the prototype buoy in the water tunnel other than the flow velocity: 1) the distance between the microphone and the flow splash, 2) moisture condition on the tarp, and 3) the water pump sound.

As the tilt angle increases, the height of the location of the microphone decreases. Even though the tilt angle change is as low as about 5° to 8°, the microphone located in the canister lid gets closer to the splash zone. Since the electret condenser microphone is sensitive to the distance from the sound source, it is an important factor to investigate.

The tarp's moisture is also an important factor in sound response of the prototype buoy. When the tarp is wet because of water contact to the tarp, sound transmission through the tarp is attenuated. As shown in Figure 4.12, the output voltage signal of the microphone decreased by about 40% when the tarp is wet.

The water tunnel pump run by variable frequency drive (VFD), is the source of background noise that the microphone can pick up in the water tunnel. Since the pump noise increases as the flow velocity increases, the relationship between the pump noise and flow velocity is important to analyze.

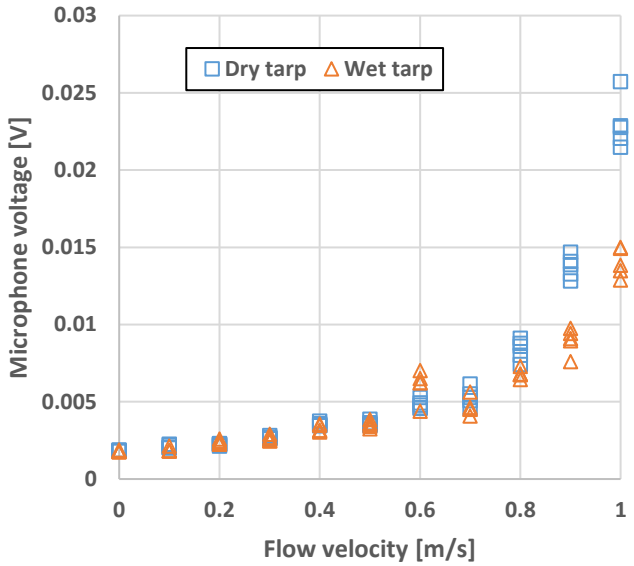

Figure 4.12: Ten trials of sound measurements to compare between dry tarp and wet tarp condition

4.1.5. Other possible sources of error

Other possible sources of error in measurement of tilt, mooring line tension, vibration, and sound are present and not easily controllable because of three constraints: 1) limited space in measurements, 2) limited quality and location in sensors, and 3) human error and unrecognized factors before measurements.

The space of the water tunnel is limited for the prototype buoy to freely vibrate without impacting the water tunnel wall. The horizonal gap between the prototype buoy and the water tunnel wall is less than 10 cm on both sides. Since the buoy portion of the prototype

buoy starts colliding with either side of the water tunnel wall at 0.6 m/s and higher, vibration acting on the prototype buoy is affected by the collision. When the piezo film sensor detects the collision impact, this causes irregular spikes in signals.

Depth of water tunnel is supposed to be always 60 cm. However, when water is not refilled in the water tunnel after a month, the depth of the water tunnel reduces about a few centimetres. As water depth decreases, water pump of the water tunnel has the same rotating frequency but less water to energize. Therefore, the water can flow faster than right after the water is filled up to 60 cm. This effect was not counted as an important source of error in result. However, this is noticeable when the steel bars start moving forward at 1 m/s. When depth of the water tunnel is 60 cm, the steel bars never move at 1 m/s. In other words, the flow velocity when the steel bars move is higher than 1 m/s.

Among the four variables, vibration measurement with a piezo film sensor has more errors compared to the other variables because vibration instrumentation includes more manually installed wiring than other sensors. Especially the charge amplifier for vibration measurement is manually assembled on a small breadboard. As the length of the circuit increases, noise from electric current also increases. Since more current flows when the piezo film sensor is more excited by the oscillation of the prototype buoy, there will be more noise generated in the instrumentation circuit. Besides, unused wires inside the canister and axial pipe may interrupt vibration measurement.

4.1.6. Noise of variable frequency drive (VFD) of water tunnel

The pump to run the water tunnel has noise when the impeller in the pump rotates. Because the pump sound, or VFD noise, increases as flow increases in terms of magnitude and frequency, this affects the relationship of the sound surrounding the prototype buoy with

the flow velocity. Figure 4.13 shows the average of two trials of the VFD of the pump of the water tunnel against the flow velocity. Since the sound frequency of the VFD noise is different from the sound frequency of flowing water in the water tunnel, it is assumed that the sound voltage generated by VFD noise can be subtracted directly from the microphone output voltage. By eliminating the VFD noise from the sound measurement data, the sound voltage generated only by the water in the water tunnel is obtained as shown in Figure 4.14. The trendline of the measurement data of sound excluding the variable frequency drive is also obtained. Also, the average ratio of VFD noise voltage to the microphone output voltage from the sound measurements is shown in Figure 4.15.

Since the VFD noise at 0 to 0.5 m/s is above 80% of the microphone voltage, and the voltage magnitudes at 0 to 0.5 m/s do not show increasing trend, the sound of flowing water at 0 to 0.5 m/s is not detectable with the microphone.

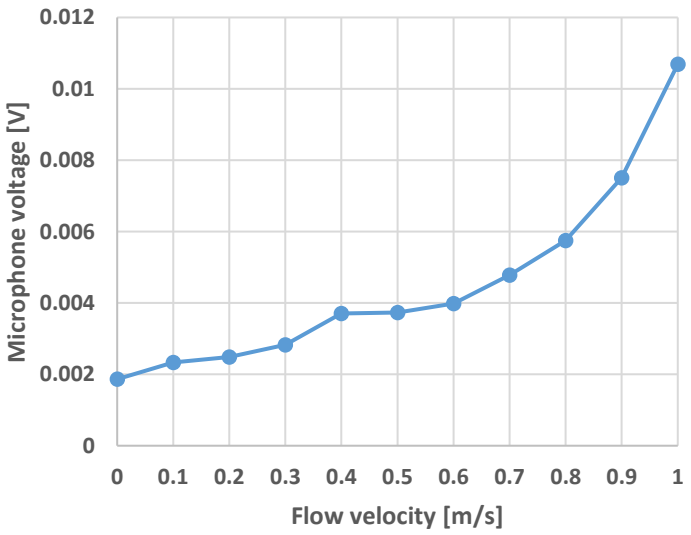

Figure 4.13: Average of two trials of VFD sound voltage vs. flow velocity

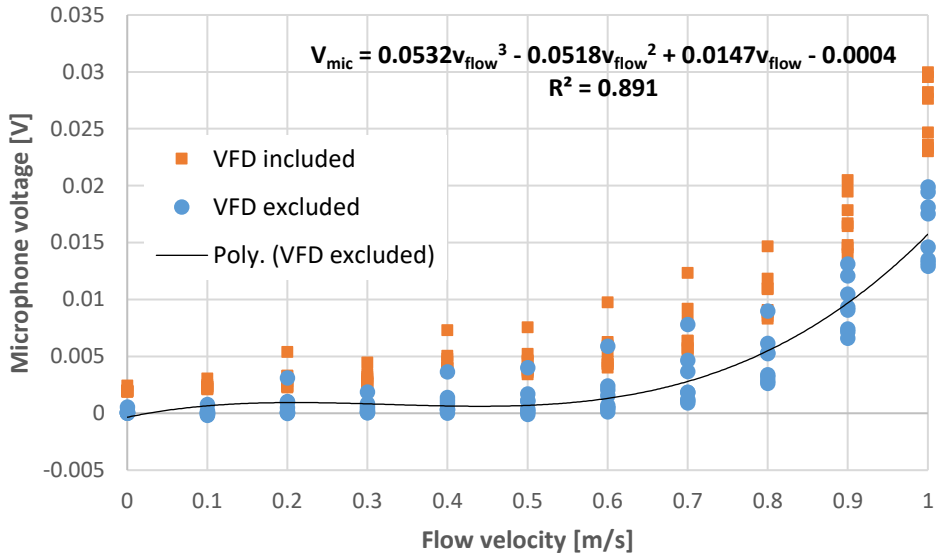

Figure 4.14: Eight sound measurements with and without VFD noise in dry tarp condition

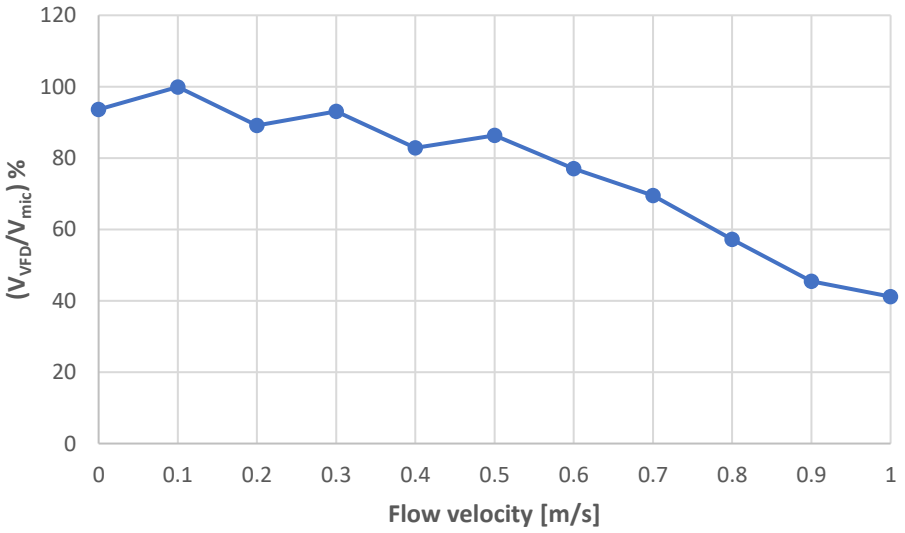

Figure 4.15: Average % ratio of VFD voltage to microphone voltage from eight sound measurements

4.2. Calibration curves by curve-fitting

For the plot of each variable's measurement data—tilt, mooring line tension, vibration amplitude, and sound—curve-fitting is applied for linear regression of polynomial terms. In Excel, a polynomial trendline feature is available. Technically, input of calibration curves is supposed to be the measurement data obtained from the prototype buoy to estimate the flow velocity, which is the output. In other words, the flow velocity is to be in y-axis while each variable's signals are to be in x-axis. However, the variables with respect to the flow velocity have positive and nonlinear, as shown in Figure 4.1 to Figure 4.7. The inverse function of the measurement data curves is in power of fractions which is too complex to be represented in Excel. Therefore, instead of using a finalized form of calibration curve function, the trendline of the plot of the four variables generated by Excel is used for estimating the flow velocity, v_{flow}, by solving for the root when the measurement data of each variable is given.

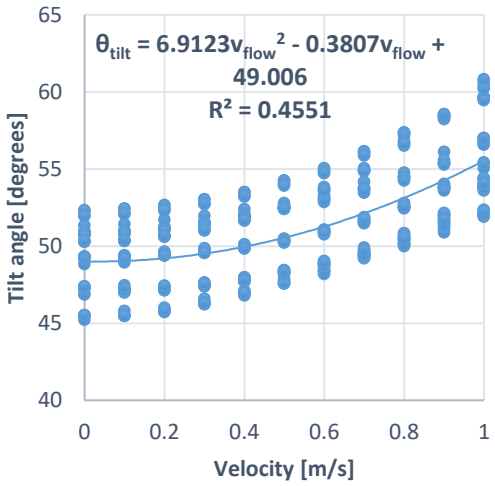

Figure 4.16: Trendline function of 43 tilt angle measurement data vs. flow velocity

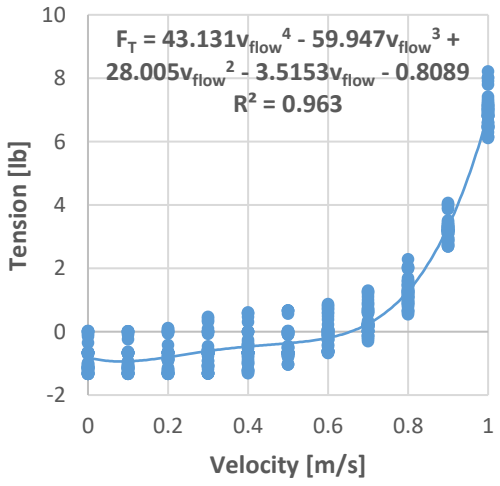

Figure 4.17: Trendline function of 50 tension measurement data vs. flow velocity

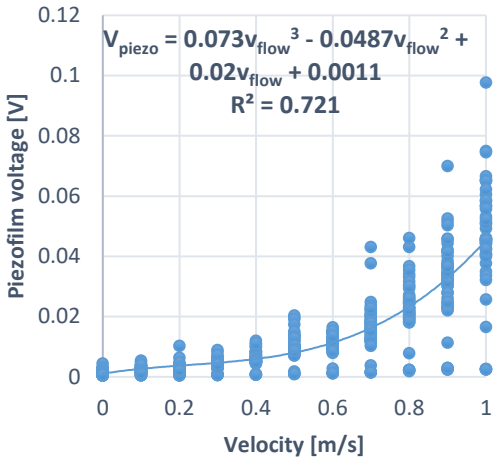

Figure 4.18: Trendline function of 43 vibration amplitude measurement data vs. flow velocity

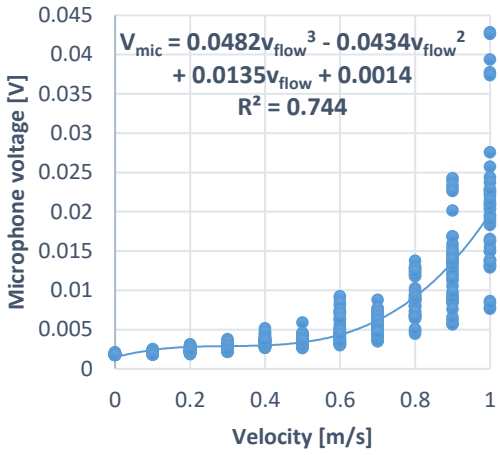

Figure 4.19: Trendline function of 43 sound measurement data vs. flow velocity

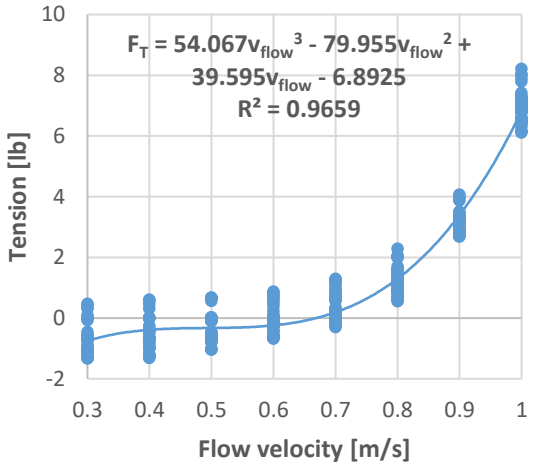

Figure 4.20: Trendline function of 50 mooring line tension measurement data vs. flow velocity excluding low flow velocities from 0 to 0.2 m/s

Figure 4.16 to Figure 4.19 show trendline functions obtained from curve-fitting plot of each variable against flow velocity. For tilt angle, a quadratic trendline function is obtained. Since the deviation in the tilt angle at zero velocity among the measurements was as large as the increase in tilt angle from zero to 1 m/s, the R^2 value was low and did not exceed 0.5. For mooring line tension, a quartic trendline function is obtained. Since the tension signals

apparently increase at flow velocity of 0.3 m/s, a cubic trendline function excluding flow velocities from 0-0.2 m/s is also obtained, as shown in Figure 4.20. The trendline of the mooring line tension has a higher R^2 value than vibration amplitude and sound measurements. The order of polynomial trendline function for each data set is determined when the R^2 value of each trendline does not increase more than 1% in higher order trendlines.

4.2.1. Residual plots to assess trendlines

To validate the trendlines, a residual plot for each variable's plot is used, as shown in Figure 4.21 to Figure 4.25. The residual plots show whether the curve-fitting on each plot is appropriate or inappropriate to analyze relationship with flow velocity by looking at the randomness of the shape of the residuals.

Two kinds of pattern in residual plots are found. First, a wave pattern is detected in Figure 4.25. The pattern can be formed by either lacking higher order terms in the trendline function or missing other independent variables. As discussed in Chapter 1, mooring line tension acting on the prototype buoy increases as the tilt angle increases. Because the tilt angle is an independent variable of mooring line tension on the prototype buoy, the trendline function of the tension data includes higher order terms than without tilt angle change. Second, increasing trend in the absolute magnitude of residuals in vibration amplitude and sound data is detected as shown in Figure 4.23 and Figure 4.24. This trend is called heteroscedasticity [63] which shows that the trendline functions are unreliable to use at the higher flow velocities. To remove this trend, natural logarithm microphone function is taken for the raw data of vibration and sound, as shown in Figure 4.26 and Figure 4.28. The

corresponding residual plot for vibration and sound, Figure 4.27 and Figure 4.29, still show increasing in absolute magnitudes as the flow increased.

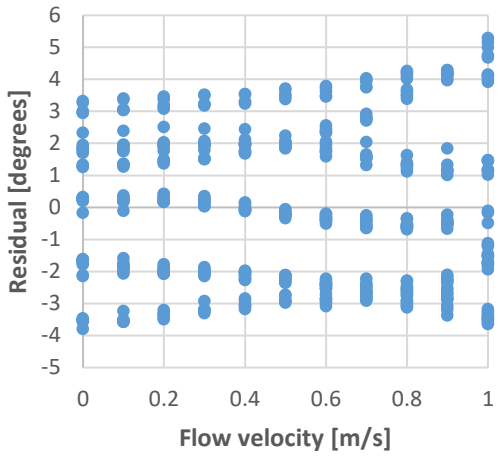

Figure 4.21: Residual plot of trendline of tilt angle of the prototype buoy against flow velocity

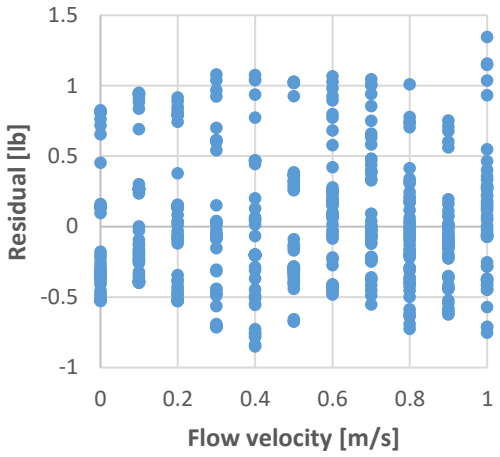

Figure 4.22: Residual plot of trendline of tension of the prototype buoy against flow velocity

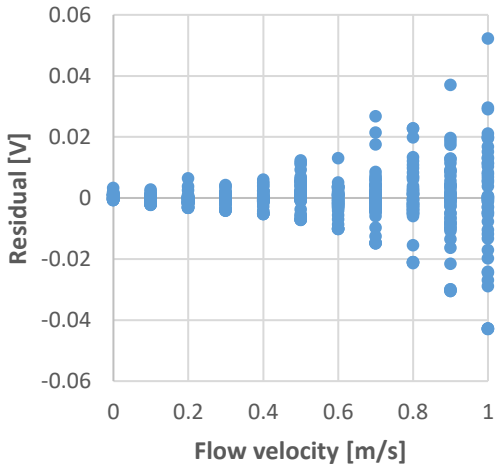

Figure 4.23: Residual plot of trendline of vibration amplitude of the prototype buoy against flow velocity

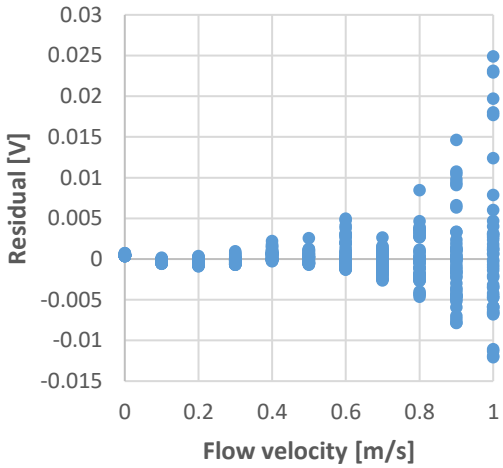

Figure 4.24: Residual plot of trendline of sound about the prototype buoy against flow velocity

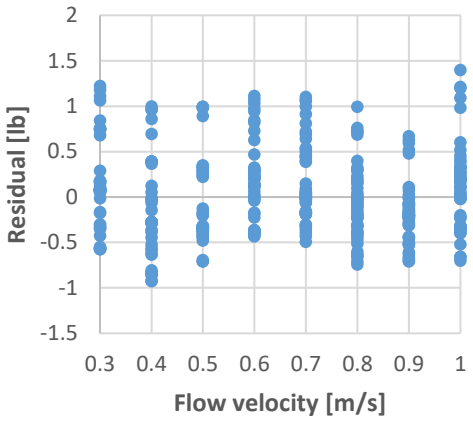

Figure 4.25: Residual plot of trendline of mooring line tension of the prototype buoy against flow velocity excluding 0 to 0.2 m/s

The main causes of heteroscedasticity are outliers in the measurement data, and missing independent variables that affect the measurements. Because of low quality in the piezoelectric sensor and the electret condenser microphone, outliers are expected in the measurements. In terms of variables, tilt angle affects vibration and sound. For vibration, vibration is affected by the angle of the immersed cylinder body of the prototype buoy and can be corrected by cosine angle for the angle range between 40° and 65°. For sound, as tilt angle increases, the height of the microphone decreases. Applying the height change to the sound signals, complexity of the nonlinear relationship between sound and the flow velocity can be reduced. However, the angle change of tilt angle of the prototype buoy is about 10 degrees, the effect of tilt angle to vibration and sound is assumed to be negligible. Therefore, the correction of vibration and sound signals with tilt angle data is not considered in this project.

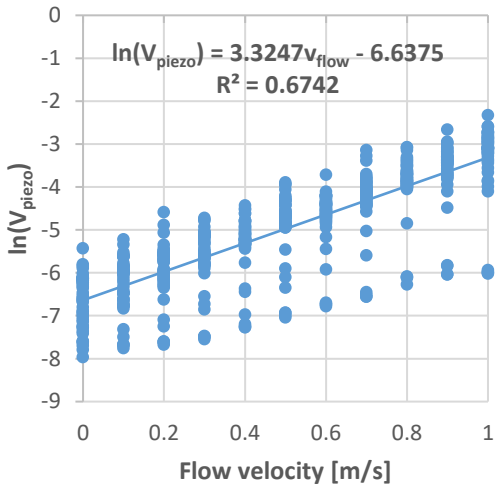

Figure 4.26: $\ln(V_{piezo})$ vs. flow velocity with trendline

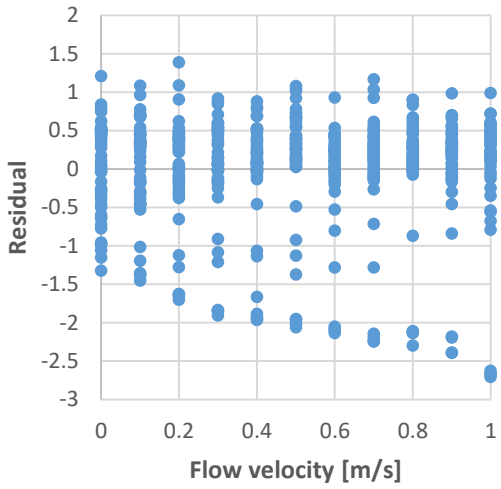

Figure 4.27: Residual plot of Figure 4.26

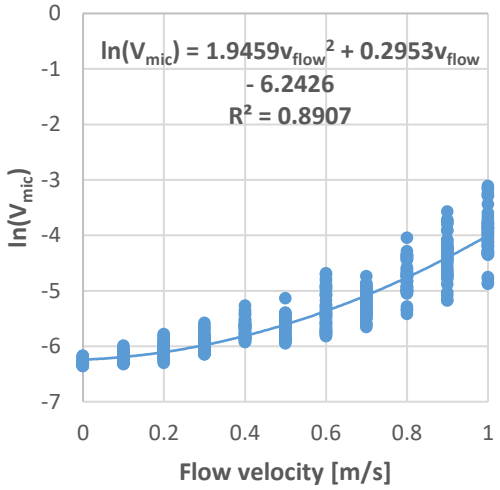

Figure 4.28: $\ln(V_{mic})$ vs. flow velocity with trendline

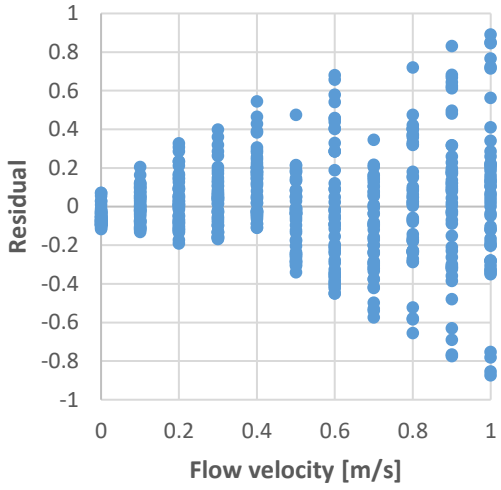

Figure 4.29: Residual plot of Figure 4.28

4.2.2. Elimination of effects originated from other variables related to flow velocity

4.2.2.1. Moisture of tarp

In the raw measurement data of the microphone, both dry tarp and wet tarp conditions are included. However, the effect of water on the tarp to sound transmission is remarkable as

illustrated in Figure 4.12. Thus, the trendline curve for both dry and wet tarp condition is obtained as shown in Figure 4.30 and Figure 4.32, respectively. Since the corresponding residual plots, Figure 4.31 and Figure 4.33, do not show any definite pattern, the calibration curves are more effective to estimate flow velocity.

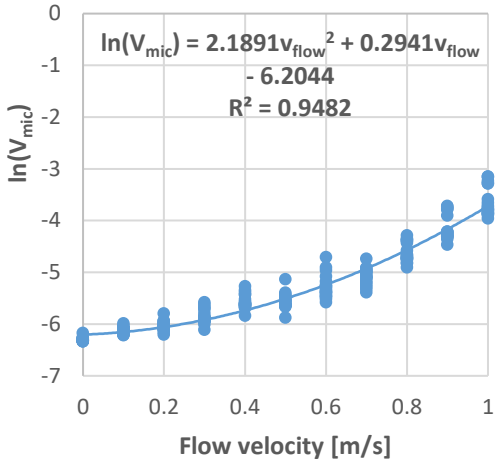

Figure 4.30: $\ln(V_{mic})$ vs. flow velocity with trendline in dry tarp condition of 19 measurements

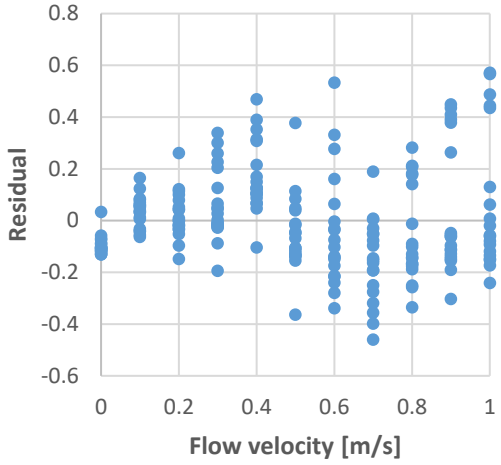

Figure 4.31: Residual plot of Figure 4.30

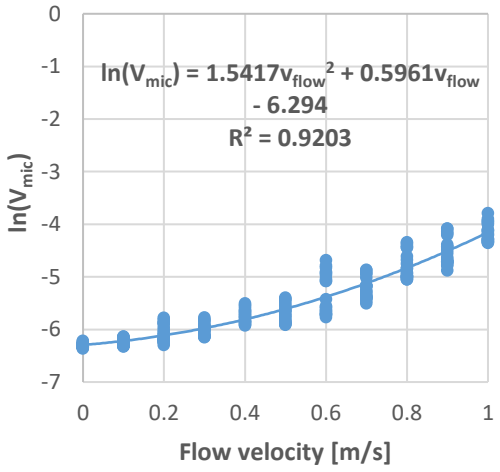

Figure 4.32: $\ln(V_{mic})$ vs. flow velocity with trendline in wet tarp condition of 20 measurements

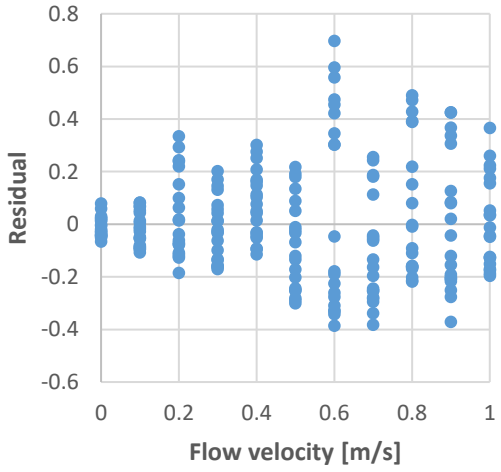

Figure 4.33: Residual plot of Figure 4.32

4.3. Estimation of flow velocity using trendline function from each variable

Using the trendline functions, flow velocity is estimated from the measurement data of each variable. The limitation of this estimation is that this is valid only for water tunnel environment where the geometrical structure of the prototype buoy under water is different from outside sites such as rivers due to water depth, wave, and eddy flow. ProteusDS simulations discussed in Chapter 3 explain more details about the difference.

4.3.1. Tilt angle of the prototype buoy

The flow velocity of the water tunnel is estimated from the average of the measurement data of tilt angle of the prototype buoy. Before using the trendline of tilt angle against flow velocity, the raw tilt data is corrected by subtracting the difference between the raw tilt data and the y-intercept of the trendline in Figure 4.16 which is the tilt angle when the estimated flow velocity is zero, $\theta_{\text{tilt\_estimated}_0} = 49.006°$, where $\theta_{\text{tilt\_raw}_0}$ is the raw data of tilt angle when flow velocity is zero. The corrected tilt angle, $\theta_{\text{tilt\_corrected}}$, is used to find the flow velocity which is the root of the trendline function as shown in Equation 4.2. That is, $\theta_{\text{tilt\_corrected}}$ is used as an input to Equation 4.3, and $v_{\text{estimated}}$, which is the root of the equation, becomes the output. Equation 4.4 is the percentage error between the actual and estimated flow velocity.

$$\theta_{\text{tilt\_corrected}} = \theta_{\text{tilt\_raw}} - (\theta_{\text{tilt\_raw}_0} - \theta_{\text{tilt\_estimated}_0}) \quad \text{Equation 4.2}$$

$$\theta_{\text{tilt\_corrected}} = 6.9123(v_{\text{estimated}})^2 - 0.3807(v_{\text{estimated}}) + 49.006 \quad \text{Equation 4.3}$$

$$\text{Error } \% = \frac{v_{\text{estimated}} - v_{\text{actual}}}{v_{\text{actual}}} \times 100\% \quad \text{Equation 4.4}$$

Using Equation 4.2 and Equation 4.3, flow velocities from 0.5 to 1 m/s are estimated when the average of tilt angle measurement data is given as shown in Figure 4.34. Table 4 shows the average tilt angle data with corrected values. The average percent error is 0.49%.

Table 4: Tilt angle measurements from 0.5 to 1 m/s flow velocity with corrected values

v_{actual} [m/s]	$\theta_{tilt\_corrected}$ [°]	$v_{estimated_{Eq.4.3}}$ [m/s]	Error %
0.5	50.55	0.5007	0.14
0.6	51.23	0.5948	0.86
0.7	52.08	0.6949	0.72
0.8	53.10	0.7976	0.29
0.9	54.35	0.9070	0.78
1	55.52	0.9983	0.17

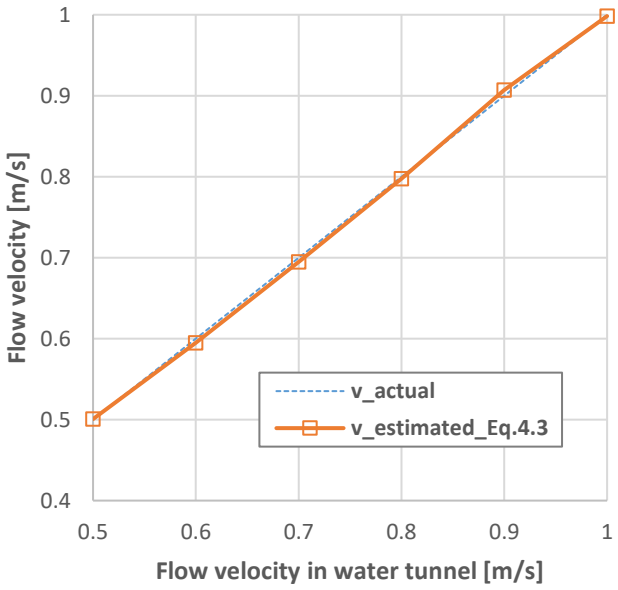

Figure 4.34: Plot of estimated flow velocity using tilt angle measurements

4.3.2. Mooring tension on the prototype buoy

Using Equation 4.5 which is the trendline function of 50 mooring line tension measurements in Figure 4.20, the flow velocities from 0.5 to 1 m/s are estimated from average of mooring

line tension measurements, F_T, as shown in Figure 4.35. That is, F_T is used as an input to Equation 4.5, and $v_{estimated}$, which is the root of the equation, becomes the output.

$$F_T = 54.067(v_{estimated})^3 - 79.955(v_{estimated})^2 + 39.595(v_{estimated}) - 6.8925 \quad \text{Equation 4.5}$$

Table 5: Mooring line tension measurements and estimated velocity from 0.5 to 1 m/s

v_{actual} [m/s]	F_T [lb]	$v_{estimated_{Eq.4.5}}$ [m/s]	Error %
0.5	-0.43	0.38	24.45
0.6	-0.12	0.64	7.18
0.7	0.33	0.72	2.48
0.8	1.20	0.79	0.80
0.9	3.19	0.89	0.86
1	6.93	1.00	0.28

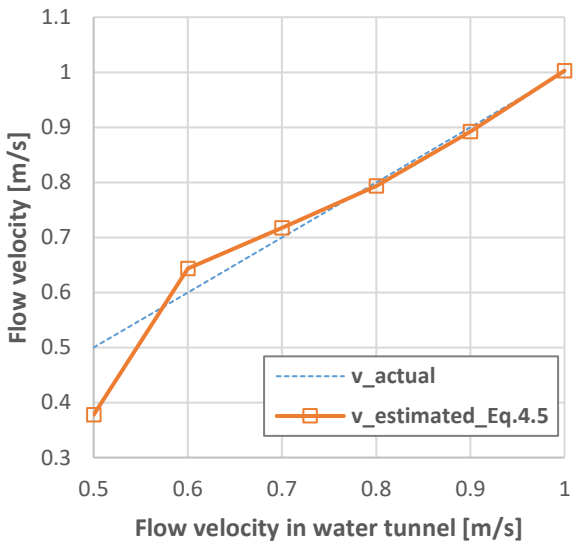

Figure 4.35: Plot of estimated flow velocity using mooring line tension measurements

At flow velocity of 0.5 m/s, the largest error at between the actual and estimated velocity occurs. The error magnitudes reduce as the flow velocity increases. The average percent error is 6.01%.

4.3.3. Vibration amplitude of the prototype buoy

Using Equation 4.6, the flow velocities are estimated from average of vibration measurements as shown in Figure 4.36.

$$Amplitude = 0.073(\mathrm{v_{estimated}})^3 - 0.0487(\mathrm{v_{estimated}})^2 + 0.02(\mathrm{v_{estimated}}) + 0.0011 \quad \text{Equation 4.6}$$

Equation 4.7 is used to remove heteroscedasticity of residuals of the vibration measurement data.

$$\ln(Amplitude) = 3.3247(\mathrm{v_{estimated}}) - 6.6375 \quad \text{Equation 4.7}$$

Table 6 shows vibration amplitude and estimated velocity from Equation 4.6 and Equation 4.7. Figure 4.36 shows the plot of the estimated velocity represented in

Table 6.

Table 6: Vibration measurements and estimated velocity from 0.5 to 1 m/s

$\mathrm{v_{actual}}$ [m/s]	Amplitude [V]	ln (amplitude [V])	$\mathrm{v_{estimated_{Eq.4.6}}}$ [m/s]	$\mathrm{v_{estimated_{Eq.4.7}}}$ [m/s]
0.5	0.010	-4.61	0.59	0.61
0.6	0.011	-4.54	0.61	0.63
0.7	0.016	-4.12	0.72	0.76
0.8	0.023	-3.77	0.81	0.86
0.9	0.032	-3.44	0.90	0.96
1	0.046	-3.08	1.01	1.07

Without taking natural log on the vibration measurements, the error between estimated and actual flow velocity fluctuates as the velocity changes. After taking natural log on the measurements, the overall error between estimated and actual velocity increases, but the

error fluctuation is more levelized. The average percent error when Equation 4.6 is used is 4.21%, and 9.43% when Equation 4.7 is used.

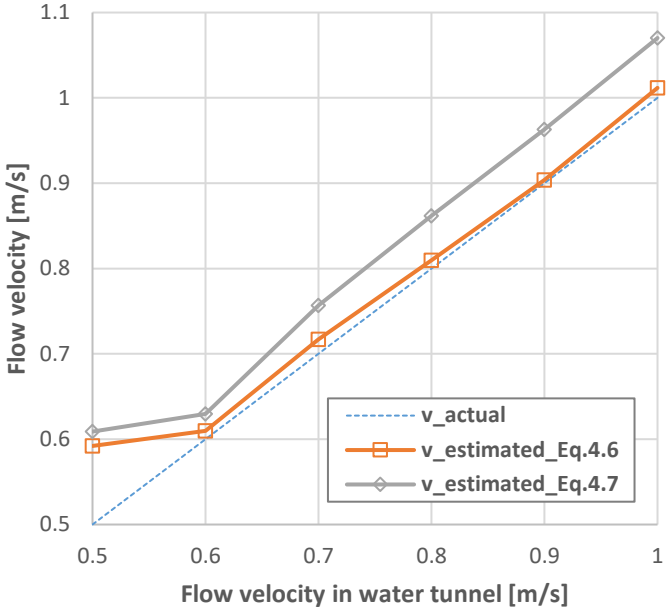

Figure 4.36: Plot of estimated flow velocity using vibration measurements

4.3.4. Sound level around the prototype buoy

Using Equation 4.8, the flow velocities are estimated from average of sound measurements as shown in Figure 4.37.

$$Sound\ level = 0.0482(\mathrm{v_{estimated}})^3 - 0.0434(\mathrm{v_{estimated}})^2 + 0.0135(\mathrm{v_{estimated}}) + 0.0014 \qquad \text{Equation 4.8}$$

Equation 4.9 is the trendline after taking natural log on the sound voltage measurements which include both dry and wet tarp condition.

$$\ln(sound\ level) = 1.9459(\mathrm{v_{estimated}})^2 + 0.2953(\mathrm{v_{estimated}}) - 6.2426 \qquad \text{Equation 4.9}$$

Equation 4.10 excludes wet tarp condition in the sound measurements.

$$\ln(sound\ level) = 2.1891(v_{estimated})^2 + 0.2941(v_{estimated}) - 6.2044 \qquad \text{Equation 4.10}$$

Table 7: Sound level measurements and estimated velocity from 0.5 to 1 m/s

v_{actual} [m/s]	Sound level [V]	$\ln(V_{mic(d+w)})$	$\ln(V_{mic(d)})$	$v_{estimated_{Eq.4.8}}$ [m/s]	$v_{estimated_{Eq.4.9}}$ [m/s]	$v_{estimated_{Eq.4.10}}$ [m/s]
0.5	0.0036	-5.63	-5.56	0.54	0.49	0.48
0.6	0.0050	-5.29	-5.28	0.65	0.63	0.59
0.7	0.0057	-5.17	-5.09	0.68	0.67	0.65
0.8	0.0089	-4.72	-4.62	0.79	0.81	0.79
0.9	0.0132	-4.33	-4.13	0.89	0.92	0.91
1	0.0202	-3.90	-3.65	1.01	1.02	1.02

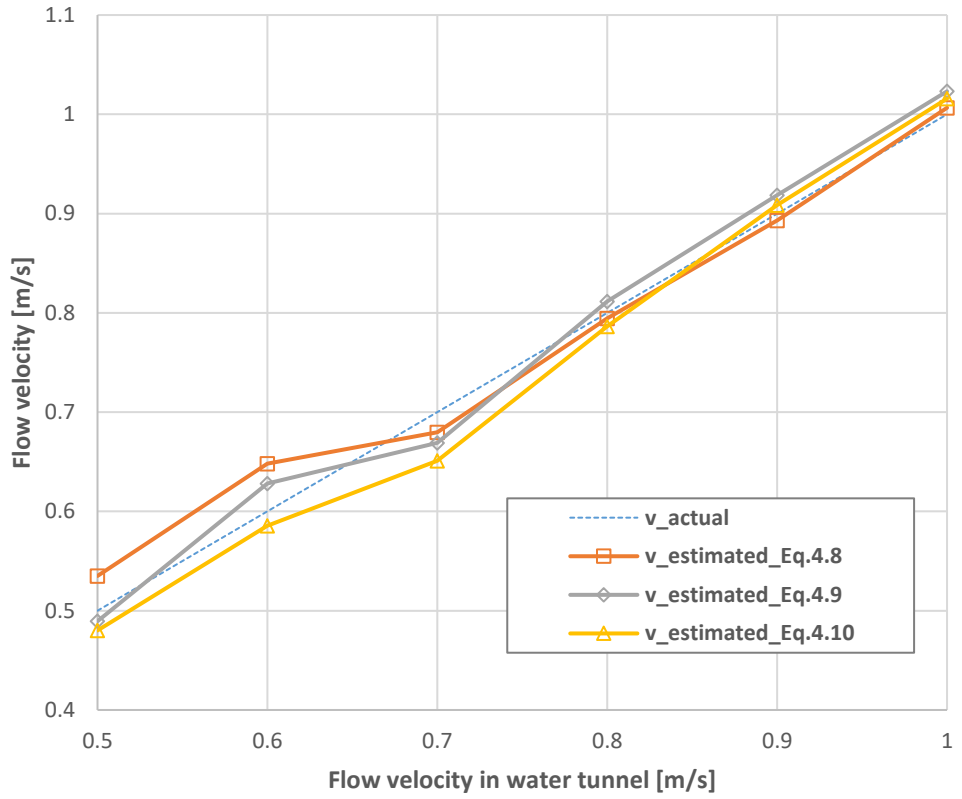

Figure 4.37: Plot of estimated flow velocity using sound measurements

Among the estimated velocity from Equation 4.8 to Equation 4.10, estimated velocity from Equation 4.8 shows less error between estimated and actual velocity at 0.6 m/s and higher, but more fluctuating shape at 0.5 m/s and lower flow velocity. The estimated velocity from

Equation 4.10, which excludes measurements in wet tarp condition, shows less error magnitudes than estimated velocity from Equation 4.9, which includes wet tarp condition. The average error when Equation 4.8 is used is 3.35%, 2.84% when Equation 4.9 is used, and 2.94% when Equation 4.10 is used.

4.4. Different characteristics between water tunnel and river

4.4.1. Flow condition

Several flow conditions cause different characteristics between the water tunnel and river setting. In terms of streamwise direction, the distance between the portion of the prototype buoy on the free surface and the downstream end of water in the water tunnel is less than 50 cm. Downstream flow behind the prototype buoy at the free surface generates sound because of the water tunnel outlet where the free surface ends. Since the surface water hits the water tunnel outlet ceiling at higher velocities, sound from flowing water is louder on the water tunnel than on river. On river, consistent sound noise of any objects approaching to the prototype buoy either by flow or emitting their own sound may exist.

Flow features in river are more various than in water tunnel. While water tunnel generates uniform flow, which has relatively uniform velocity profile in vertical direction, downstream river flow velocity differs along the vertical direction. In terms of flow floor condition, water tunnel has uniform flat contour without any sediments at the bottom floor of the water tunnel. In contrast, river has mostly non-uniform contour at the riverbed and has sediments. Therefore, flow velocity measurement in river has more uncertainties that influence the measurement accuracy.

4.4.2. Underwater portion of prototype buoy

In water tunnel environment, the major portion of the prototype buoy under water surface is the buoy and the axial pipe connecting between the buoy and wire rope. Also, the cross-sectional area of the prototype buoy underwater in water tunnel is relatively irregular because of the buoy portion under water. Because of the large size of the frontal area due to large cross-sectional area, the vortex shedding frequency becomes less than 10 Hz, which requires a specialized vibration sensor to detect the frequency. Vortex shedding frequency is higher and easily detected when the frontal area of submerged object throughout the object is smaller and uniform because the frequency is inversely proportional to the characteristic diameter which is determined by the frontal area of the object. In water tunnel, slender and constant characteristic diameter is impossible for the prototype buoy. Therefore, vortex shedding frequency around the prototype buoy is unavailable to be measured. The vortex shedding amplitude is also affected by frontal area of the prototype buoy under water. Therefore, the amplitude data contains errors that are difficult to remove in water tunnel laboratory setting.

In contrast, in river several times deeper than the water tunnel, the wire rope is the major portion of the prototype buoy under water. Therefore, the frontal area against the flow to the prototype buoy under water in the water tunnel is smaller and less various than in the water tunnel.

4.4.3. ProteusDS simulations to find different characteristics between water tunnel and river

Using ProteusDS simulations, mooring tension force in between water tunnel and river with respect to flow velocity is represented in Figure 4.38 and Figure 4.39. The drag force caused by the water flow is proportional to the frontal area of the submerged portion of the

prototype buoy. Since deeper water setting makes the frontal area of the submerged portion of the prototype buoy larger, at 1 m/s, as shown in Figure 4.40, tension acting on the wire rope in river setting is also more than the tension in water tunnel setting.

Tilt angle of the prototype buoy in water tunnel and river setting is also simulated in ProteusDS. In Figure 4.41, however, tilt angle change from 0 to 1 m/s of flow velocity is less than one degree while the tilt angle measurements in Figure 4.1 and Figure 4.2 show that the tilt angle change is at least a few degrees. The different results may be due to assignment of the buoyant force acting along the surface area that water contacts with the buoy. Assigning buoyant force of the entire submerged portion of the prototype buoy is available, but not the centre location of the buoyant force. Tilt angle of the buoy depends on the force balance and the moment balance of the prototype as discussed in Chapter 1. Since only the centre of gravity is available to be assigned, the effect of buoyancy on angular direction can only be applied in the centre of gravity. Since accurate estimation of the centre of gravity including the buoyant force of the prototype buoy is complicated, further analysis addressing on this estimation will be needed.

In Figure 4.42, the trendline of the tilt angle against flow velocity does not show any concave up curvature. Since measurement of tilt angle of the prototype in higher flow velocity than 1 m/s was not included in this research, further analysis will be needed to validate the relationship between tilt angle of the prototype buoy and flow velocity.

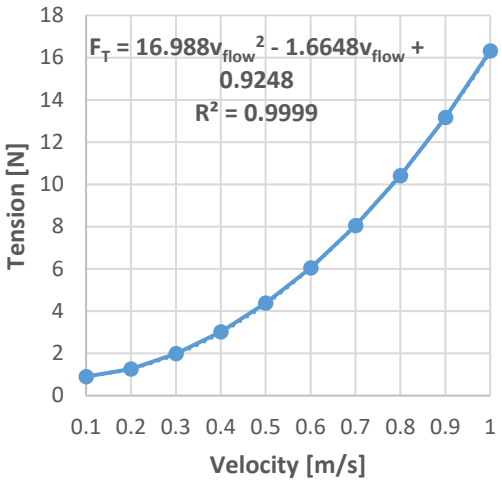

Figure 4.38: ProteusDS result of mooring tension force of wire rope vs. flow velocity from 0.1 to 1 m/s in water tunnel setting

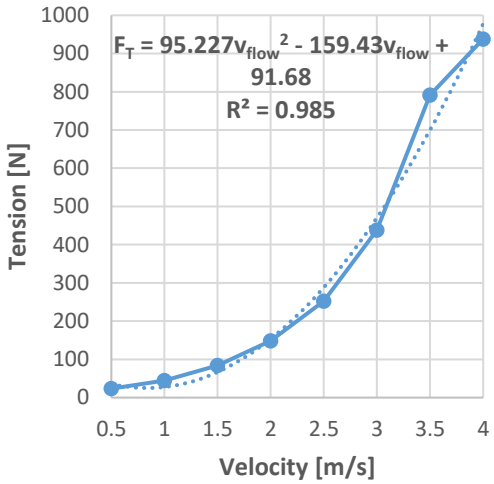

Figure 4.39: ProteusDS result of mooring tension force of wire rope vs. flow velocity from 0.5 to 4 m/s in river setting

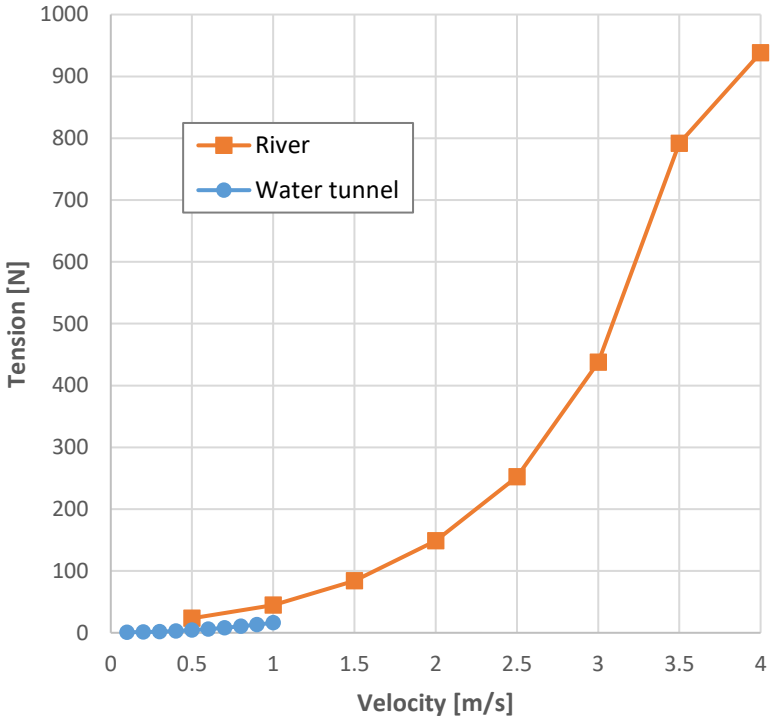

Figure 4.40: Combined plot of Figure 4.38 and Figure 4.39

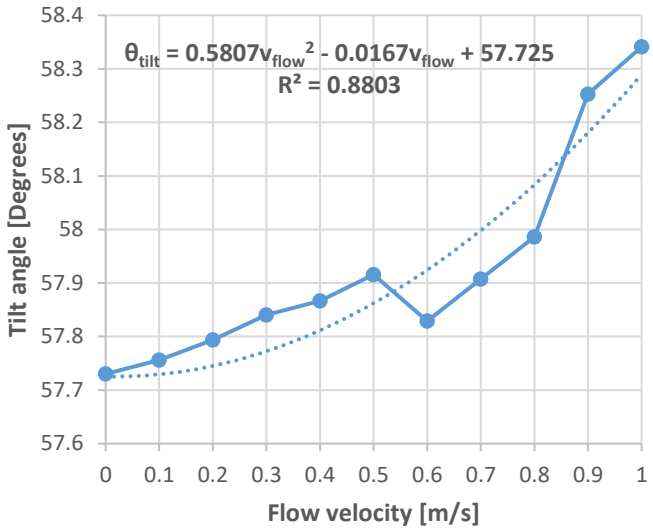

Figure 4.41: ProteusDS result of tilt angle of prototype buoy vs. flow velocity from 0.1 to 1 m/s in water tunnel setting

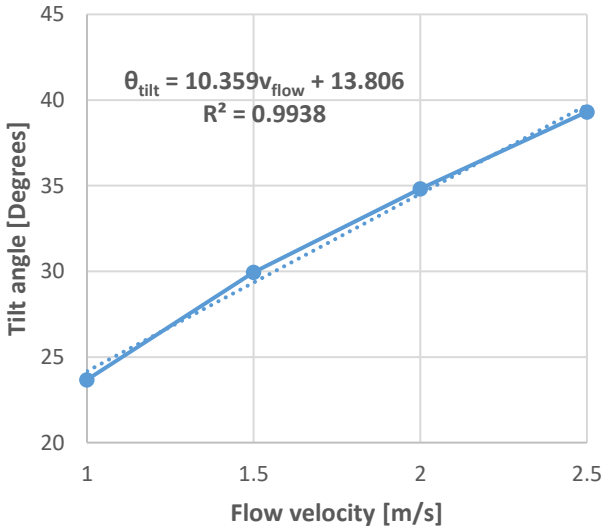

Figure 4.42: ProteusDS result of tilt angle of prototype buoy vs. flow velocity from 1 to 2.5 m/s in river setting

4.5. Evaluation of the four measurement methods

Based on the results discussed in Chapter 4.1-4.4, evaluation of the four rugged velocity meter methods in different features is summarized in Table 8.

Related sub-variables of each method need to be controlled to obtain reasonable estimation of flow velocity. For both tilt angle and mooring line tension method, first, the ratio between the depth of water and the length of wire rope under water and, second, the equilibrium curvature of wire rope under water due to drag force are required to be investigated. Also, the fitting between the buoy and wire rope also causes relative motion that affects the tilt angle and the mooring line tension. For the vibration amplitude method, the characteristic diameter of the submerged portion of the prototype buoy determines the vortex shedding frequency. As the water depth is deeper, the characteristic diameter becomes closer to the diameter of the wire rope. For the piezo film sensor, roll orientation angle of the prototype buoy affects the output of the vibration amplitude. For the sound method, first, tarp condition affects the output of sound voltage output. Second, the distance between the microphone and water surface is a factor to be considered. This changes when the tilt angle of the prototype buoy changes. Also, other noises different from the water may need to be filtered if the noises exist consistently over time during measurements. Especially for the sound method, the sound in the water tunnel is mostly generated due to the water tunnel wall facing the downstream. In the river setting there is no wall for flowing water to face. This will decrease capturable sound volume. The actual magnitude of sound measured in river at the same flow velocity as in water tunnel may not be larger than in the water tunnel.

In terms of accuracy, the measurement method using tilt angle data is the most accurate method to estimate flow velocity among the four methods.

Table 8 Evaluation of the four rugged long-term velocity meter methods. (ln): taking natural logarithm on voltage signals

Variable / Feature	Tilt	Tension	Vibration amplitude	Sound
Relationship to flow velocity	Nonlinear	Nonlinear	Nonlinear	Nonlinear
Related sub-variables	1) Ratio of water depth to wire rope length. 2) Frontal area of submerged portion of the prototype buoy. 3) Relative motion at fitting between buoy and wire rope.		1) Characteristic diameter of submerged portion of the prototype buoy. 2) Orientation angle of piezo sensor.	1) Tarp wetness. 2) Attenuation of sound. signals through tarp 3) Distance between microphone and water surface. 4) Noise other than from water.
Maximum error of estimated velocity	0.007 m/s	0.12 m/s	0.09 m/s, 0.11 m/s (ln)	0.05 m/s, 0.03 m/s (ln), 0.05 m/s (ln, dry tarp only)
Average percent error in accuracy	0.49%	6.01%	4.21%, 9.43% (ln)	3.35%, 2.84% (ln), 2.94% (ln, dry tarp only)
Difference in response between measurement in water tunnel and river	1) Tilt angle of prototype buoy at zero flow velocity. 2) Lower tilt angle of prototype buoy in river.	1) At the same flow velocity, higher mooring tension acts in river.	1) Higher vortex shedding frequency in river. 2) Higher vibration amplitude in river.	1) No structural barriers in the middle of river. 2) Noise resources from objects approaching to prototype buoy or emitting sound in river.

5. Conclusion and recommendations

5.1. Conclusion

The rugged long-term velocity measurement methods using four variables: tilt, mooring line tension, vibration amplitude, and sound are designed to evaluate the capability to measure flow velocity. A calibration curve in terms of the flow velocity is obtained by trendline function in Excel using the repeated measurements of each variable. All the four variables have nonlinear relationship with flow velocity. Residual plots are used to assess if the relationship of each method is valid for flow velocity estimation. According to the residual plots, tilt and mooring line tension method are appropriate to be used, but vibration amplitude and sound method need further processes to use the relationship. Using the calibration curve for each variable, flow velocities are estimated when a set of measurement for each variable is given. Among the four rugged velocity measurement methods, tilt data estimated the most accurate flow velocity. The average percent error in accuracy to estimate flow velocities of 0.5 to 1 m/s is 0.49 % from tilt angle data. Using mooring line tension data, the accuracy is 6.01 %, From vibration magnitude data, flow velocity can be estimated about 9.43 % error in accuracy. Lastly, from sound data, the accuracy is 2.94 %.

The vortex shedding frequency measurement data is not obtained in the water tunnel because the maximum available frequency with the characteristic diameter of the submerged portion of the prototype buoy in the water tunnel is approximately 2 Hz which is too low to measure with the low-end piezo film sensor. In a river, where the water depth is as deep as several metres, the characteristic diameter becomes closer to the wire rope diameter because almost all the portion of the prototype buoy under water is the wire rope. In this case, available vortex shedding frequency increases, and it means it is easier to be measured.

Each velocity measurement method has multiple sub-variables that affect the relationship with flow velocity used for each method. The sub-variables are caused by reasons classified into three categories: 1) the posture of the prototype buoy underwater, 2) the feature of sensors, and 3) specific condition for certain method. For tilt and mooring line tension method, because the prototype buoy can be posed differently according to the depth of water, the ratio between the water depth and the length of the wire rope affects the relationship of each variable with the flow velocity. For vibration method, the piezo film sensor is sensitive to the orientation of the point where the sensor is installed. For sound method, the conditions of tarp installed on the lid of the canister of the prototype buoy are the sub-variables. Wetness of tarp and tarp itself attenuate sound transmission through the tarp. Also, the distance between the microphone and water surface is also a sub-variable. All the sub-variables from the four methods are required to be controlled to have reliable calibration curves.

The calibration curves are only obtained from measurement data taken in the water tunnel. However, it is impractical without collecting measurement data of tilt, mooring line tension, vibration, and sound in river because of different depth of water and different surroundings have different relationship between each variable and the flow velocity. Therefore, measurements in river with various flow velocities are required to find more relevant relationship which makes relevant calibration curves to estimate flow velocity.

Rugged velocity measurement methods for hydrokinetic energy resource assessment will help decrease time and cost for determination of hydrokinetic turbine sites. While conventional instruments such as ADV and ADCP must have fixtures and platforms to sustain these devices from rapid streams for at least several months,

rugged velocity meters do not need such structure to safely guard the devices. To install the rugged velocity meters, only a boat to reach the point of deployment of the velocity meters is required. This will shorten duration of the setup, and the cost of hydrokinetic energy resource assessment of the site of interest will decrease. Since this will make hydrokinetic energy resource assessment easier, more hydrokinetic turbines can be installed and operated in a shorter time. Also, remote communities which have been consuming electric power generated by fossil fuels can start implementing hydrokinetic turbine that do not generated any greenhouse gases.

5.2. Recommendations

Measurement data of the variables: tilt, mooring line tension, vibration amplitude and frequency, and sound in rivers with various flow velocities is important to collect. Since not only the water tunnel generates velocity from 0 to 1 m/s, but also its maximum water depth is 60 cm, which makes the wire rope of the prototype buoy cannot be fully used as in river. This causes the behaviour of tilt, mooring tension, and vibration to be different between water tunnel and river. The real practical calibration curves that contain the similar physical aspects can only be obtained from repeated measurements taken in river.

A higher quality piezoelectric sensor without adding a mass to increase sensitivity on low frequency is recommended to be used instead of low-end piezo film sensor that needs such a mass attached. One of the sources of error in vibration amplitude result is the motion of the added mass attached at the end of the cantilever beam shape of the piezo film sensor. Since the piezo film sensor is attached at the inner surface of the connecting pipe portion between the buoy and the wire rope at a tilted orientation, the added mass can move individually when water flows outside the pipe portion in the water tunnel.

To make the measurements of the variables in the water tunnel closer to measurements collected in river in terms of physical behaviours of the prototype buoy due to flow, it is suggested to assemble a model which is a scaled-down device but has similar physical properties such as the characteristic diameter of the prototype buoy under water and the centre of mass of the prototype buoy.

Location of microphone is suggested to be inside the buoy of the prototype buoy because at the current location, the sound is attenuated by the tarp which is waterproof for the microphone. To capture sound only from water surrounding the prototype buoy, a better-quality microphone with waterproof is required. Instead of measuring the ambient sound of the flow, measurement of impact sound of water flow is more capturable in terms of magnitude. The water flow collides with the buoy where the sound is generated at the buoy surface. Therefore, it is effective to install a microphone inside the buoy at the inner surface of the water-fronting area of the buoy.

Further analysis on ProteusDS simulation of tilt and mooring line tension is recommended to find the more accurate relationship with flow velocity. The tilt angle of the prototype buoy is the result of the equilibrium shape of the wire rope portion of the prototype buoy under water. The complicated equilibrium shape is accurately simulated in the software. However, in the simulation software ProteusDS, the centre of buoyant force of the buoy is not individually defined. Since only the centre of mass of the assembled parts of the prototype buoy can be defined, the buoyant force coordinates need to be added on the coordinates of the centre of mass. By solving this calculation, the tilt angle of the prototype buoy can be simulated more accurately.

6. Bibliography

[1] NOAA Global monitoring laboratory, "Trends in Atmospheric Carbon Dioxide," NOAA Global monitoring laboratory, 5 May 2021. [Online]. Available: https://gml.noaa.gov/ccgg/trends/. [Accessed 12 May 2021].

[2] NASA's Goddard Space Flight Center, "Sea Level - SATELLITE DATA: 1993-PRESENT," the Earth Science Communications Team at NASA's Jet Propulsion Laboratory, 6 May 2021. [Online]. Available: https://climate.nasa.gov/vital-signs/sea-level/. [Accessed 12 May 2021].

[3] REN 21, "RENEWABLES 2020 GLOBAL STATUS REPORT," REN 21, Paris, 2020.

[4] NASA Goddard Institute for Space Studies, "GLOBAL LAND-OCEAN TEMPERATURE INDEX," the Earth Science Communications Team at NASA's Jet Propulsion Laboratory, 6 May 2021. [Online]. Available: https://climate.nasa.gov/vital-signs/global-temperature/. [Accessed 12 May 2021].

[5] A. Betz, "Introduction to the Theory of Flow Machines," Oxford: Pergamon Press, 1966.

[6] A. S. Bahaj and L. E. Myers, "Fundamentals applicable to the utilisation of marine current turbines for energy production," *Renewable Energy,* vol. 28, no. 14, pp. 2205-2211, 2003.

[7] Natural Resources Canada, "Canadian Weather Energy and Engineering Datasets," Natural Resources Canada, 2020.

[8] W. Jenkinson, "Canada's hydrokinetic power potential," 2013.

[9] V. T. Chow, "2-4. Velocity Distribution in a Channel Section," in *Open-Channel Hydraulics*, Tokyo, McGraw-Hill, 1959, pp. 24-26.

[10] R. Vaid, "Designing, optimizing, and testing of a river hydrokinetic prototype turbine system for remote northern communities," Department of Mechanical Engineering, the University of Manitoba, Winnipeg, Canada, 2020.

[11] S. d'Auteuil, "Investigation of velocity and turbulence measurement techniques for riverine hydrokinetic turbine sites," University of Manitoba, Winnipeg, 2017.

[12] T. Sarpkaya, Wave Forces on Offshore Structures, Cambridge; New York: Cambridge University Press, 2010.

[13] F. M. White, Fluid Mechanics, Toronto: McGraw-Hill Book Company, 1979.

[14] Nortek Group, "Technical specification - Vector-300 m," [Online]. Available: https://www.nortekgroup.com/products/vector-300-m/pdf.

[15] H. Chanson, M. Trevethan and S.-i. Aoki, "Acoustic Doppler velocimetry (ADV) in small estuary: Field experience and signal post-processing," *Flow Measurement and Instrumentation,* vol. 19, no. 5, pp. 307-313, 2008.

[16] H. Chanson and N. J. Docherty, "Turbulent velocity measurements in open channel bores," *European Journal of Mechanics B/Fluids,* no. 32, pp. 52-58, 2012.

[17] M. S. Sulaiman, S. K. Sinnakaudan and M. R. Shukor, "Near Bed Turbulence Measurement with Acoustic Doppler Velocimeter (ADV)," *KSCE Journal of Civil Engineering,* vol. 17, no. 6, pp. 1515-1528, 2013.

[18] B. Gunawan, V. S. Neary and J. Colby, "Tidal energy site resource assessment in the East River tidal strait, near Roosevelt Island, New York, New York," *Renewable Energy,* vol. 71, pp. 509-517, 2014.

[19] R. L. Gordon, "Acoustic measurement of river discharge," *Journal of Hydraulic Engineering,* vol. 115, no. 7, pp. 925-936, 1989.

[20] B. S. X. S. M. K. D. S. K. C. J. R. P. W. N. S. R. T. X. a. F. I. Gunawan, "An integrated and novel approach to estimating the conveyance capacity of the River

Blackwater," in *Proceedings of the Eight International Conference on Hydro-Science and Engineering*, Nagoya, Japan, 2008.

[21] E. R. C. a. O. K. Nystrom, "Evaluation of Mean Velocity and Turbulence Measurements with ADCPs," *Hydraulic Engineering,* vol. 133, pp. 1310-1318, 2007.

[22] Nortek Group, "CURRENT PROFILER Signature55," 2022. [Online]. Available: https://www.nortekgroup.com/products/signature55. [Accessed 15 July 2022].

[23] V. Neary, B. Gunawan, M. Richmond, V. Durgesh, B. Polayge, J. Thompson, M. Muste and A. Fontaine, "Field measurements at river and tidal current sites for hydrokinetic energy development: best practices manual," US Department of Energy, 2011.

[24] ENVCO, "Global Water Flow Probe," Global Water, 2022. [Online]. Available: https://envcoglobal.com/catalog/water/liquid-flow/current-meters-and-discharge-monitoring/flow-counters-and-computers/global. [Accessed 2 December 2022].

[25] C. E. Brennen, "An Internet Book on Fluid Dynamics: Introduction to Flow Rate and Velocity Measurement," 10 June 2006. [Online]. Available: http://brennen.caltech.edu/fluidbook/measurement/instrumentation/flowrate/introduction.pdf. [Accessed 1 12 2022].

[26] A. S. Almeida and V. C. B. d. Souza, "An alternative method for measuring velocities in open-channel flows: perfomance evaluation of a Pitot tube compared to an acoustic meter," *Brazilian Journal of Water Resources,* vol. 22, no. 26, 2017.

[27] Lowell Instruments, "Tilt Current Meters," Lowell Instruments, 2022. [Online]. Available: https://lowellinstruments.com/. [Accessed 2022].

[28] R. Adrian, "Particle-imaging techniques for experimental fluid mechanics," *Annual Review of Fluid Mechanics 23,* pp. 261-304, 1991.

[29] A. Boutier, Laser Velocimetry, London, UK: John Wiley & Sons, Inc., 2012.

[30] I. Fujita, M. Muste and A. Kruger, "Large-scale particle image velocimetry for flow analysis in hydraulic engineering applications," *Journal of Hydraulic Research,* vol. 36, no. 3, pp. 397-414, 1998.

[31] I. Fujita, "Development of a non-intrusive and efficient flow monitoring technique: The space-time image velocimetry (STIV)," *International Journal of River Basin Management,* vol. 5, no. 2, pp. 105-114, 2007.

[32] M. Muste, I. Fujita and A. Hauet, "Large-scale particle image velocimetry for measurements in riverine environments," *WATER RESOURCES RESEARCH,* vol. 44, no. W00D19, pp. 1-14, 2008.

[33] M. Muste, R. Ettema and I. Fujita, "Flow diagnostic in hydraulic modeling using image velocimetry," *Journal of Hydrological Engineering,* vol. 130, no. 3, pp. 175-185, 2004.

[34] I. Fujita, Y. Notoya, K. Tani and S. Tateguchi, "Efficient and accurate estimation of water surface velocity in STIV," *Environmental Fluid Mechanics,* vol. 19, pp. 1363-1378, 2019.

[35] F. Tauro, R. Piscopia and S. Grimaldi, "Streamflow Observations From Cameras: Large-Scale Particle Image Velocimetry or Particle Tracking Velocimetry?," *Water Resources Research,* vol. 53, pp. 10374-10394, 2017.

[36] C. J. Legleiter and P. J. Kinzel, "Surface Flow Velocities From Space: Particle Image Velocimetry of Satellite Video of a Large, Sediment-Laden River," *Frontiers in Water,* vol. 3, 2021.

[37] B. Lüthi, T. Philippe and S. Peña-Haro, "Mobile device app for small open-channel flow measurement," in *7th Intl. Congress on Env. Modelling and Software in International Environmental Modelling and Software Society (iEMSs)*, San Diego, CA, 2014.

[38] T. Nakamura, S. Kaneko, F. Inada, M. Kato, K. Ishihara, T. Nishihara, N. W. Mureithi and M. A. Langthjem, "Vibration Induced by Cross-Flow: Classifications and Lessons From Practical Experiences, 2nd Edition," in *Flow-Induced Vibrations*, London, Academic Press, 2014, pp. 29-45.

[39] O. M. Griffin and S. E. Ramberg, "Some recent studies of vortex shedding with application to marine tubulars and risers," *Journal of Energy Resources Technology,* vol. 104, no. 1, pp. 2-13, 1982.

[40] R. King, "Vortex excited structural oscillations of a circular cylinder in steady currents," in *Offshore Technology Conference*, 1974.

[41] P. W. Bearman, "Vortex Shedding from Oscillating Bluff Bodies," *Annual Reviews Fluid Mechanics,* pp. 195-222, 1984.

[42] L. R. Wootton, M. H. S. R. N. Warner and D. H. Cooper, "Oscillations of piles in marine structures. A resume of the full-scale experiments at Immingham.," CIRIA Techology, 1972.

[43] C. C. Feng, "The measurement of vortex-induced effects in flow past a stationary and oscillating circular and D-section cylinders," University of British Columbia, Vancouver, 1968.

[44] A. Khalak and C. H. K. Williamson, "Dynamics of a hydro elastic cylinder with very low mass and damping," *Journal of Fluids and Structures,* no. 10, pp. 455-472, 1996.

[45] A. Khalak and C. H. K. Williamson, "Fluid forces and dynamics of a hydro elastic structure with very low mass and damping," *Journal of Fluids and Structures,* no. 11, pp. 973-982, 1997.

[46] A. Khalak and C. H. K. Williamson, "Investigation of relative effects of mass and damping in vortex-induced vibration of a circular cylinder," *Journal of Wind Engineering and Industrial Aerodynamics,* pp. 69-71, 341-350, 1997.

[47] J. HE, S. Y, B. MJ and M. C, "Correlating sound and flow rate at a tap," *Procedia Engineering,* vol. 119, pp. 864-873, 2015.

[48] K. R. Cheatle, Fundamentals of Test Measurement Instrumentation, Research Triangle Park, North Carolina: Instrumentation, Systems, and Automation Society, 2006.

[49] K. Tuck, "Tilt Sensing Using Linear Accelerometers," 18 April 2007. [Online]. Available: https://archive.eetasia.com/www.eetasia.com/ARTICLES/2007APR/PDF/EEOL_2007APR18_STECH_AN_01.pdf. [Accessed 8 June 2021].

[50] PocketLab, "How does an Accelerometer Work - Physics of Probeware," 16 April 2018. [Online]. Available: https://archive.thepocketlab.com/educators/lesson/how-does-accelerometer-work-physics-probeware. [Accessed 4 February 2020].

[51] R. S. Khandpur, "Accelerometer," *Compendium of Biomedical Instrumentation,* vol. 1, no. 1, pp. 1-8, 2020.

[52] K. Hoffmann, "1.2 The measurement system," in *An Introduction to Measurements using Strain Gages*, Darmstadt, Hottinger Baldwin Messtechnik GmbH, 1989, pp. 15-16.

[53] Measurement Specialties Inc, "Piezo Film Sensors Technical Manual," March 2008. [Online]. Available: https://www.metrolog.net/files/piezofilm_manual_en_metrolog.pdf. [Accessed 23 January 2020].

[54] Arduino, "What is Arduino?," 5 February 2018. [Online]. Available: https://www.arduino.cc/en/Guide/Introduction. [Accessed 9 June 2022].

[55] Adafruit Industries, "Adafruit 10-DOF IMU Breakout - L3GD20H + LSM303 + BMP180," 2020. [Online]. Available: https://www.adafruit.com/product/1604. [Accessed 19 October 2020].

[56] STMicroelectronics, "LSM303DLHC," 2011. [Online]. Available: https://cdn-shop.adafruit.com/datasheets/LSM303DLHC.PDF. [Accessed 19 October 2020].

[57] TE Connectivity Ltd., "LDT1-028K PIEZO SENSOR," 2017. [Online]. Available: https://www.tti.com/content/dam/ttiinc/manufacturers/te-sensor-solutions/Piezo/PDF/LDT1_028K.pdf. [Accessed 15 September 2020].

[58] Measurement Specialties, *MiniSense 100 Vibration Sensor,* Hampton, VA: Measurement Specialties, 2009.

[59] Adafruit Industries, "Electret Microphone Amplifier - MAX4466 with Adjustable Gain," 2020. [Online]. Available: https://www.adafruit.com/product/1063. [Accessed 7 January 2021].

[60] CUI Inc, "PART NUMBER: CMA-4544PF-W," 2008. [Online]. Available: https://cdn-shop.adafruit.com/datasheets/CMA-4544PF-W.pdf. [Accessed 5 January 2021].

[61] Maxim Integrated Products, "Low-Cost, Micropower, SC70/SOT23-8, Microphone Preamplifiers with Complete Shutdown," 2001. [Online]. Available:

https://cdn-shop.adafruit.com/datasheets/MAX4465-MAX4469.pdf. [Accessed 5 January 2021].

[62] Dynamic Systems Analysis Ltd., "ProteusDS Manual," 4 June 2018. [Online]. Available: https://proteusds.com/software-downloads/ProteusDS%20Manual.pdf. [Accessed 30th September 2019].

[63] J. Frost, "Heteroscedasticity in Regression Analysis," October 2017. [Online]. Available: https://statisticsbyjim.com/regression/heteroscedasticity-regression/. [Accessed 12 June 2022].

[64] M. Ridgill, S. P. Neill, M. J. Lewis, P. E. Robins and S. D. Patil, "Global riverine theoretical hydrokinetic resource assessment," *Science Direct - Renewable Energy,* no. 174, pp. 654-665, 2021.

[65] C. Roozeboom, "How does an Accelerometer Work - Physics of Probeware," 16 April 2018. [Online]. Available: https://archive.thepocketlab.com/educators/lesson/how-does-accelerometer-work-physics-probeware. [Accessed 5 June 2021].

[66] DAN-FENDER, "How to correctly use a mooring buoy," DAN-FENDER, 2021. [Online]. Available: https://danfender.com/p/faq/how-to-correctly-use-a-mooring-bouy. [Accessed 10 November 2021].

[67] J. H. J. VanZwieten, N. E. Matthew, K. D. von Ellenrieder, J. W. Lovenbury and L. Kilcher, "Experimental Evaluation of Motion Compensated ADV Measurements for In-Stream Hydrokinetic Applications," in *2015 IEEE/OES Eleveth Current, Waves and Turbulence Measurement (CWTM)*, St. Petersburg, FL, USA, 2015.

[68] H. Chanson, "ACOUSTIC DOPPLER VELOCIMETRY (ADV) IN THE FIELD AND IN LABORATORY: PRACTICAL EXPERIENCES," Division of Civil Engineering at the University of Queensland, Brisbane, QLD, Austrailia, 2008.

[69] A. Botelho, P. Ferreira, F. Lima, L. M. C. Pinto and S. Sousa, "Assessment of the environmental impacts associated with hydropower," *Renewable and Sustainable Energy Reviews,* vol. 70, pp. 896-904, 2017.

[70] M. I. Yuce and A. Muratoglu, "Hydrokinetic energy conversion systems: A technology status review," *Renewable and Sustainable Energy Reviews,* vol. 43, pp. 72-82, 2015.

[71] S. S. Rao, Mechanical Vibrations, Toronto: Prentice Hall, 2011.

[72] B. Dzhudzhev, V. Ivancheva, S. Kachulkova and E. Gospodinova, "Vibration Measurement with Piezoelectric Transducer," Technical University of Sofia, Sofia, Bulgaria.

[73] K. Vikestad, J. K. Vandiver and C. M. Larsen, "Added mass and oscillation frequency for a circular cylinder subjected to vortex-induced vibrations and external disturbance," *Journal of Fluid and Structures,* no. 14, pp. 1071-1088, 2000.

[74] B. Gunawan, M. Sterling and D. W. K. MCIWEM, "Using an acoustic Doppler current profiler in a small river," *Water and Environment Journal,* vol. 24, no. 2, pp. 147-158, 2010.

[75] A. Eltner, H. Sardemann and J. Grundmann, "Flow velocity and discharge measurement in rivers using terrestrial and UAV imagery," *Hydrology and Earth System Sciences,* vol. 289, 2019.

[76] K. Bhuyan, "Uncertainty analysis of acoustic flow measuring instruments for characterization of high energetic river flow," University of Manitoba, Winnipeg, 2019.

Appendix A. Arduino code

```
// This code reads raw gps data, parses it and writes desired data to an SD card.
// It is modified code from Adafruit's GPS libraries
// to work with the Arduino Mega and to write only desired and parsed information.

// Link the ultimate GPS shield   ------> http://www.adafruit.com/products/1272
// Link to a GPS data resource    ------> http://www.gpsinformation.org/dale/nmea.htm#RMC

// Including the appropriate header files
#include <Adafruit_GPS.h>    // Adafruit's GPS Library
#include <SoftwareSerial.h>  // Software Serial library
#include <Adafruit_GFX.h>    // Core graphics library
#include <Adafruit_ST7735.h> // Hardware-specific library for the screen
#include <SPI.h>
#include <SD.h>              // Arduino SD card library.  Editted by
#include <avr/sleep.h>
#include <Wire.h>
#include <Adafruit_Sensor.h>
#include <Adafruit_LSM303_Accel.h>
#include <HX711.h>

/*****************************************************************************************************************/
/************************************** CONSTANTS AND PIN LABELS ************************************************/

// Initializing the software serial pins and functionality for direct printout to
SoftwareSerial mySerial(11, 10);
Adafruit_GPS GPS(&mySerial);

// Set GPSECHO to 'false' to turn off echoing the GPS data to the Serial console
// Set to 'true' if you want to debug and listen to the raw GPS sentences.
// Set LOG_FIXONLY to 'false' to log data even without a fix
#define GPSECHO     false
#define LOG_FIXONLY false
#define chipSelect     53
#define ledPin         13

#define calibration_factor 320 //This value is obtained using the SparkFun_HX711_Calibration sketch
#define LOADCELL_DOUT_PIN  25
#define LOADCELL_SCK_PIN  27
#define GND 29

uint32_t dSampT = 100;  // Digital sample frequency
uint32_t anSampT = 1000;    // Analog sample frequency (microseconds)
uint64_t anTimer;          // The timer used to count down to the next analog sample
uint64_t dTimer;           // The timer used to count down to the next digital sample

uint32_t analogueSampleTimer;         // Initializing the timer variable for
```

```
uint32_t analogueSampleTimer;         // Initializing the timer variable for
                                      // an analogue sampling period
uint32_t analogueSampleTime = 3000;  // Setting the analogue sampling period
uint8_t  dCount = 0;                  // Digital sample counter
uint8_t  digitalSamplesPerCycle = 10; // Setting the number of digital samples
                                      // before an analog sampling period

int GT_OFFSET = 5;        // Global time offset in hours

long int waitTimer;       // Pre-initializing the variable that will be used to
                          // determine the current time spent waiting for a GPS fix

boolean waiting = false;  // A truth variable used to set if the Arduino has
                          // started waiting for a proper GPS signal

// This is a constant stored inside the environmental sensor library
// it is used to figure out the temperature and altitude from the pressure
// This can be replaced with a better known number that will more accurately
// determine the temperature and altitude
float seaLevelPressure = SENSORS_PRESSURE_SEALEVELHPA;
//float piezo = 0;
//float piezoOne = 0;
float piezoTwo = 0;
float piezoThree = 0;
float mic =0;

float ReadingA_Strain1 = 365.0;
float LoadA_Strain1 = 0.0; //  (Kg,lbs..)
float ReadingB_Strain1 = 371.0;
float LoadB_Strain1 = 4.0; //  (Kg,lbs..)

// Software declaration of the various IMU sensors and libraries
Adafruit_LSM303_Accel_Unified accel = Adafruit_LSM303_Accel_Unified(54321);

/* The numbers inside the function calls above are taken
 * straight from an example sketch of using each function.
 * Do not change these or do research before doing so.
 */

File logfile; // Initializing the log file for later logging

//HX711 scale;
/**************************************************************************************************/
/************************************* FUNCTION DEFINITIONS ***************************************/


/************************************** HEX PARSING ROUTINE ***************************************/

// read a Hex value and return the decimal equivalent

uint8_t parseHex(char c) {
  if (c < '0')
    return 0;
  if (c <= '9')
    return c - '0';
  if (c < 'A')
    return 0;
  if (c <= 'F')
    return (c - 'A')+10;
}

/**************************************************************************************************/
/************************************* IMU SENSOR & strain gauge amplifier INITIALIZATION *************************************/

// IMU sensor & HX711(strain gauge amplifier) initialization routine

void initSensors()
{
 if (!accel.begin()) {
    /* There was a problem detecting the ADXL345 ... check your connections */
    Serial.println("Ooops, no LSM303 detected ... Check your wiring!");
    while (1)
      ;
 }
}
```

```
// Allows the turning off of the 1/ms interupt routine described later.
// This must be kept as true as the manual polling alone causes the parsing to fail frequently.
boolean usingInterrupt = true;

// Function prototype keeps the Arduino happy
void useInterrupt(boolean); // Taken straight from the GPS parsing example code in the adafruit GPS library


/*****************************************************************************************************/
/********************************************** MAIN SETUP ***********************************************/

// The majority of the setup occurs in this function

void setup() {

  // IMU sensor & HX711 initialization
  initSensors();

  // connecting to the serial line at 115200 so we can
  // read the GPS and echo it without dropping parts
  // GPS of a message
  Serial.begin(115200);
  Serial.print(seaLevelPressure);

  //pinMode(A0,INPUT);// Vibration
  //pinMode(A1,INPUT);// Vibration1
  pinMode(A9,INPUT);// Sound
  pinMode(A3,INPUT);// Vibration2
  pinMode(A4,INPUT);// Vibration3
  /* Uncomment for debugging */
  // see if the card is present and can be initialized:
  if (!SD.begin(chipSelect, 53)) { //53 was originally 51
    //if (!SD.begin(chipSelect)) {      // if you're using an UNO, you can use this line instead
    Serial.println("Card init. failed!");
  }
  fileNamer();

  useInterrupt(true);

  dTimer = millis();
  anTimer = millis();
}

/*****************************************************************************************************/
/************************************** GPS INTERUPT POLLING *****************************************/

// This is interupt handler that will be called once/millisecond by the interupt routine

SIGNAL(TIMER0_COMPA_vect) {

  char c = GPS.read(); // Reads the current GPS data if a new reading was received
  // The next few lines are a speedier way to do debug printing to the serial monitor
  #ifdef UDR0
    if (GPSECHO)
      if (c) UDR0 = c;
      // writing direct to UDR0 is much much faster than Serial.print
      // but only one character can be written at a time.
  #endif
}

/*****************************************************************************************************/
/************************************** INTERUPT ROUTINE *********************************************/

// This sets an interupt to be called off of TIMER0 once a millisecond


void useInterrupt(boolean v) {
  if (v) {
    // Timer0 is already used for millis() - we'll just interrupt somewhere
    // in the middle and call the "Compare A" function above
    OCR0A = 0xAF;
    TIMSK0 |= _BV(OCIE0A);
    usingInterrupt = true;
  }
  else {
    // do not call the interrupt function COMPA anymore
    TIMSK0 &= ~_BV(OCIE0A);
    usingInterrupt = false;
  }
}
```

```
/*****************************************************************************************************/
/********************************************** FILE NAMER ***********************************************/

// File naming routine. Generates a file named "000.TXT" or incements
// the number by 1 if the file name already exists within the SD card.

void fileNamer() {
  char filename[8];
  strcpy(filename, "000.TXT");
  for (uint16_t i = 0; i < 1000; i++) {

    filename[0] = '0' + i/100;
    filename[1] = '0' + (i%100)/10;
    filename[2] = '0' + i%10;

    // create if does not exist, do not open existing.
    if (!SD.exists(filename)){break;}
  }

  logfile = SD.open(filename,FILE_WRITE);

}

/*****************************************************************************************************/
/********************************************** ZERO PADDER ***********************************************/

// This function handles the zero padding "num" up to a length of len = 4

char zeroPad(int num, int len) {
  char pbuffer     [16]; // This is creating an empty character
                         // array for formatted printing.
                         // It is big enough to fit the necessary

                        // characters plus a few extra for stability

  if (len == 2) {
    // This fills pbuffer with the appropriate formatted string
    sprintf(pbuffer,"%02d",num);
  }
  if (len == 3) {
    // This fills pbuffer with the appropriate formatted string
    sprintf(pbuffer,"%03d",num);
  }
  if (len == 4) {
    // This fills pbuffer with the appropriate formatted string
    sprintf(pbuffer,"%04d",num);
  }
  else {return "failed";}
  return pbuffer;
}

/*****************************************************************************************************/
/************************************** DIGITAL LOGGING ROUTINE **************************************/

// Handles the logging of digital type data.
// Add additional in kind data here.

void digitalLog() {
    accel.setRange(LSM303_RANGE_4G);
    accel.setMode(LSM303_MODE_HIGH_RESOLUTION);

    sensors_event_t event;
    accel.getEvent(&event);

    /* Get a new sensor event */
    Serial.print("millis: "); Serial.println(millis());
    logfile.print("millis: "); logfile.println(millis());

    /* Logging relevent information to the file here */

    // Logging the pitch, roll, and heading pulled from the IMU
    Serial.print("X: ");
    Serial.print(event.acceleration.x);
    Serial.print("  ");
    Serial.print("Y: ");
    Serial.print(event.acceleration.y);
    Serial.print("  ");
    Serial.print("Z: ");
    Serial.print(event.acceleration.z);
    Serial.print("  ");
```

```
    Serial.println("m/s^2");
    Serial.print("tilt angle: ");
    //Serial.println(180/3.14*acos((event.acceleration.z)/(sqrt(sq(event.acceleration.x)+sq(event.acceleration.y)+sq(event.acceleration.z)))));
    Serial.print(90-180/3.14*atan((event.acceleration.x)/(sqrt(sq(event.acceleration.y)+sq(event.acceleration.z)))));
    Serial.print(" roll: ");
    if(event.acceleration.z<0)
    {Serial.println(180+180/3.14*atan((event.acceleration.y)/(event.acceleration.z)));
    }
    else if(event.acceleration.y<0)
    {Serial.println(360+180/3.14*atan((event.acceleration.y)/(event.acceleration.z)));
    }
    else
    {Serial.println(180/3.14*atan((event.acceleration.y)/(event.acceleration.z)));
    }
    logfile.print("X: ");
    logfile.print(event.acceleration.x);
    logfile.print("  ");
    logfile.print("Y: ");
    logfile.print(event.acceleration.y);
    logfile.print("  ");
    logfile.print("Z: ");
    logfile.print(event.acceleration.z);
    logfile.print("  ");
    logfile.println("m/s^2");
    logfile.print("tilt angle: ");
    //logfile.println(180/3.14*acos((event.acceleration.z)/(sqrt(sq(event.acceleration.x)+sq(event.acceleration.y)+sq(event.acceleration.z)))));
    logfile.print(90-180/3.14*atan((event.acceleration.x)/(sqrt(sq(event.acceleration.y)+sq(event.acceleration.z)))));
    logfile.print(" roll: ");
    if(event.acceleration.z<0)
    {logfile.println(180+180/3.14*atan((event.acceleration.y)/(event.acceleration.z)));
    }
    else if(event.acceleration.y<0)
    {logfile.println(360+180/3.14*atan((event.acceleration.y)/(event.acceleration.z)));
    }
    else
    {logfile.println(180/3.14*atan((event.acceleration.y)/(event.acceleration.z)));
    }

    Serial.print("millis: "); Serial.println(millis());
    logfile.print("millis: "); logfile.println(millis());
    logfile.flush();

}

/*****************************************************************************************************/
/************************************* ANALOGUE LOGGING ROUTINE ************************************/


// Handles the logging cycle for analogue sampling periods.
// Add additional analogue type data to be sampled here.

void analogueLog () {

  anTimer = millis();
  analogueSampleTimer = millis();
  //Serial.print("analog s timer: "); Serial.println(analogueSampleTimer);
  Serial.print("millis: "); Serial.println(millis());
  logfile.print("millis: "); logfile.println(millis());
  while ((millis()-analogueSampleTimer) <= analogueSampleTime) {
    if ((micros()-anTimer)>=anSampT) {
      piezoTwo = analogRead(A3);
      Serial.print(piezoTwo);Serial.print("/");
      logfile.print(piezoTwo);logfile.print("/");
      piezoThree = analogRead(A4);
      Serial.print(piezoThree);Serial.print("/");
      logfile.print(piezoThree);logfile.print("/");

      mic = analogRead(A9);
      Serial.print(mic);Serial.print("/");
      logfile.print(mic);logfile.print("/");

      float newReading_Strain1 = analogRead(0);  // analog in 0 for Strain 1
      float load_Strain1 = ((LoadB_Strain1 - LoadA_Strain1)/(ReadingB_Strain1 - ReadingA_Strain1)) * (newReading_Strain1 - ReadingA_Strain1) + LoadA_Strain1;
      Serial.println(load_Strain1);     // display strain 1 load
      logfile.println(load_Strain1);

      anTimer = micros(); // Reset the timer
    }
  }
  Serial.print("millis: "); Serial.println(millis());
  logfile.print("millis: "); logfile.println(millis());

  logfile.flush();
}

/*****************************************************************************************************/
/************************************************ MAIN *********************************************/

// This is the main loop that will be run continuosly

void loop(void) {
    if ((millis()-dTimer)>=dSampT){
      digitalLog();
      dCount++;
      dTimer = millis(); // Resetting the digital timer after the completion of a cycle
```

```
      //logfile.println(""); // Ends the line if not recording any analog at this time
      logfile.flush();
    }

    if (dCount>=digitalSamplesPerCycle) {
      analogueLog();
      dCount = 0;
      logfile.println("");  //
      logfile.flush();
    }
}
```